MASTER

The effects of contact material and contact geometry on high current interruption in vacuum

van den Akker, W.F.

Award date:
1996

EG/96/830

FACULTEIT DER ELEKTROTECHNIEK

Vakgroep Elektrische Energietechniek

The Effects of Contact Material and Contact Geometry on High Current Interruption in Vacuum

W.F. van den Akker

EG/96/830.A

Afstudeerwerk verricht o.l.v.:
Prof.ir. G.C. Damstra
Dr.ir. W.F.H. Merck
Eindhoven, oktober 1996.

TECHNISCHE UNIVERSITEIT EINDHOVEN

Acknowledgements

I would like to thank prof.ir. G.C. Damstra and Dr.ir. W.F.H. Merck for our fruitful discussions. Furthermore I would like to thank Arie van Staalduinen, Hans Vossen and Ton Wilmes for their help with the experiments. Finally I would like to thank Dr.ir. J.K.M. Jansen, Wil Kortsmit and Jos van Schijndel for their help with the numerical implementation of the current contraction model.

Summary

These days vacuum circuit breakers are more and more used in electricity grids with voltages up to 40 kV. Two of the most important parameters regarding the interruption performance of these vacuum circuit breakers are the contact material and the contact geometry. The aim of this master's project was to investigate the influence of these two parameters on the interruption performance in order to give a classification of the investigated contacts. Criteria for the classification are: the number of reignitions, the reignition voltages or reignition field strengths and the erosion of the contacts. Butt-type and coil-type contacts were used as contact geometries.

The interruption performance of these contacts is measured using a Weil-Dobke synthetic circuit and a high speed camera that has been developed at KEMA.

The CuCr butt-type contacts perform well for arc energies below approximately 1 kJ. For larger energies the effect of the axial magnetic field of the coil-type contacts becomes more significant and the interruption performance of the butt-type contact decreases in comparison with the coil-type contacts.

The contact materials of the coil-type electrodes were: Cu, CuCr, CuW and AgWC. Of the these materials AgWC is most suited for implementation in "low surge breakers" and CuCr is most suited for the use of short-circuit current interruptions. Cu has as main disadvantage the very high erosion of the anode and is therefore not very suited as a contact material for vacuum circuit breakers. CuW is a very promising material for the interruption of high currents but has to be investigated in more detail.

The current contraction and the heating of the anode contact turned out to be very important parameters for the interruption behavior. Therefore the development of a finite element method model for the calculation of the current contraction and the anode spot formation has been started. The current contraction model for the butt-type electrodes gives results that confirm the existence of current contraction.

Samenvatting

Vandaag de dag worden er steeds meer vacuümvermogensschakelaars toegepast in middenspanningsnetten. Twee van de belangrijkste parameters voor het onderbrekingsgedrag van deze vacuümschakelaars zijn het contact materiaal en de contact geometrie. Doel van dit afstudeerwerk was het effect van deze twee parameters op het onderbrekingsgedrag van een vacuümschakelaar te onderzoeken teneinde een classificatie van de onderzochte contacten te verkrijgen. Criteria voor de classificatie zijn: het aantal herontstekingen, de herontsteekspanningen of de herontsteek veldsterkten en de slijtage van de contacten.

Het onderbrekingsgedrag van deze contacten wordt onderzocht met behulp van een Weil-Dobke synthetisch circuit en een snelcamera die ontwikkeld is bij de KEMA.

De CuCr "butt-type" contacten vertonen een prima onderbrekingsgedrag voor boogenergieën lager dan ongeveer 1 kJ. Voor grotere boogenergieën krijgt het effect van het axiaal magnetisch veld, gegenereerd door de "coil-type" contacten, de overhand en verslechtert het onderbrekingsgedrag van de "butt-type" contacten snel in vergelijking met het onderbrekingsgedrag van de "coil-type" contacten.

De "coil-type" contacten waren uitgerust met de contact materialen: Cu, CuCr, CuW en AgWC. Van deze materialen is AgWC het meest geschikt voor het gebruik in zogenaamde "low surge breakers" en is CuCr het meest geschikt voor het onderbreken van kortsluitstromen. Cu heeft als grote nadeel dat er erg veel slijtage is aan het anode contact en is daarom niet erg geschikt als contact materiaal voor vacuümvermogensschakelaars. CuW is een veel belovend contact materiaal voor het onderbreken van kortsluitstromen maar er moet nog meer onderzoek naar gedaan worden.

Het blijkt dat de stroomcontractie en de verhitting van het anode contact een grote invloed hebben op het onderbrekingsgedrag van de contacten. Er is daarom begonnen met de ontwikkeling van een "finite element method" model dat de stroomcontractie en de verhitting van de anode berekend. Het stroomcontractie model voor "butt-type" contacten geeft resultaten die het bestaan van stroomcontractie bevestigen.

Contents

1. Introduction

Since the beginning of this century, electricity grids have been expanding in both geometric size and transported power. Circuit breakers always have played an important role in controlling these large expanding grids. The improvements to which the circuit breakers continuously have been subjected therefore are not strange. These improvements were possible thanks to extensive research.

Circuit breakers can be divided into different groups. As a main division circuit breakers can be characterized into groups based on their arcing medium. One then finds circuit breakers that use air, oil, SF_6 or vacuum as arcing medium.

These days vacuum circuit breakers belong to the most used circuit breakers in grids with voltages up to 40 kV. Reasons for this popularity are the compactness of the circuit breaker, the environmental very friendly arcing medium and the high availability of the circuit breaker. The main reason for this high availability is the relative simple switching mechanism [Sme94].

A lot of research has been done on the interruption performance of this economically very attractive vacuum circuit breaker. The contact material and the contact geometry turned out to be among the most important parameters for the interruption performance.

In order to investigate the differences in interruption behavior of different contact materials and contact geometries, a cooperation with Toshiba Corporation Fuchu Works Tokyo was started at the Eindhoven University of Technology. The investigation is executed with the materials Cu, CuW, CuCr and AgWC. For each material two contact geometries are used, one that generates an axial magnetic field and one that generates neither an axial nor a transverse magnetic field.

The contacts that did not generate an axial or transverse magnetic field were investigated by Binnendijk [Bin95]. The interruption performance of the contacts that have a special geometry in order to generate an axial magnetic field is described in chapter 4 of this report. The different contact materials will be compared and also the effect of the axial magnetic field will be discussed.

The contact material and the contact geometry also influence the formation of a so called anode spot. An anode spot is a large molten area on the contact surface. Because an anode spot can damage the vacuum circuit breaker severely and can lead to a serious interruption failure, the formation of this anode spot has to be prevented. Chapter 5 of this report presents a Finite Element Method (FEM) model that tries to predict the formation of an anode spot. This model however has not been finished yet due to a lack of time. Chapter 5 therefore concentrates on the current contraction part of the model. The contact material and the generation of an axial magnetic field are parameters of the model.

2. Interrupting current with a vacuum circuit breaker

This chapter will deal with some of the basic concepts of interrupting current with a vacuum circuit breaker.

An interruption of current with a circuit breaker can be dived into an arc phase before current zero and a recovery phase after current zero. Whether an interruption with a vacuum circuit breaker is successful or not depends on a number of parameters [Sme94]:

- peak value of the recovery voltage;
- slope of the recovery voltage just after current zero;
- slope of the current just before current zero;
- contact gap at current zero;
- peak value of the arc current;
- arcing time;
- contact material;
- geometry of the contacts.

The first six parameters are determined by the circuit and the switching mechanism and will be treated in chapter 3. A combination of the last four parameters however determines the appearance of the vacuum arc. The appearance of the vacuum arc is one of the main indirect parameters for a successful interruption and therefore will be treated extensively in paragraph 2.1.1 Paragraph 2.1.2 and 2.1.3 will discuss the effect of the contact material and the contact geometry on the arc appearance.

2.1 Arc phase

2.1.1 Arc appearance

Based on the observations made by a number of persons, Craig Miller distinguishes a number of arc appearances [Mil83] [Mil85]:

- Diffuse Arc Mode;
- Footpoint Mode;
- Anode Spot Mode;
- Intense Arc Mode;

The diffuse arc mode actually represents two low current modes of the arc. In the first mode the anode is inert and acts only as a collector of the plasma emitted by the cathode. In the second mode the anode emits a flux of sputtered particles. The flux emitted by the anode is about six percent of the flux emitted by the cathode [Mil83].

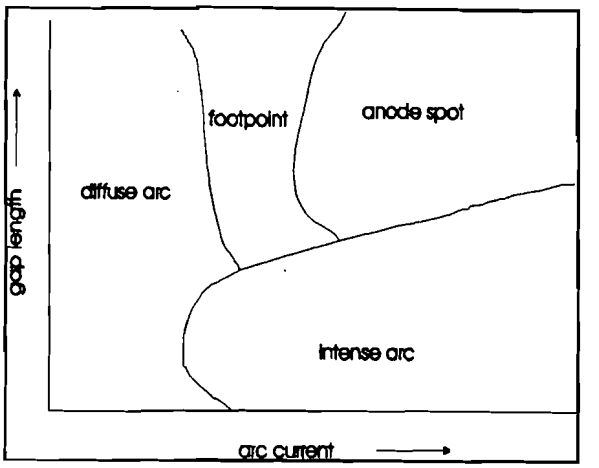

Figure 2-1: Sketch of the arc modes as a function of current and gap length [Mil85].

The plasma that conducts the current in the diffuse arc mode is formed mainly in so called cathode spots. These spots have a typical diameter of several µm, carry currents up to around 100 A and move across the surface with a speed in the order of several ten m/s [Daa78]. In these cathode spots electrons and neutral particles are formed by explosive evaporation of the contact material. Directly in front of the cathode surface most of the neutral particles are ionized by energetically interaction with the emitted electrons [McC74], [Mit87].

The formed plasma flows with a velocity in the order of 500 m/s from the cathode towards the anode. The thermal speed of the electrons in the plasma is in the order of 10^6 m/s and the speed of the ions in the plasma is in the order of 10^4 m/s [Sch83].

Using the directions stated in Figure 2-2, the current carried by the plasma is given by equation (2-1) [Bin95].

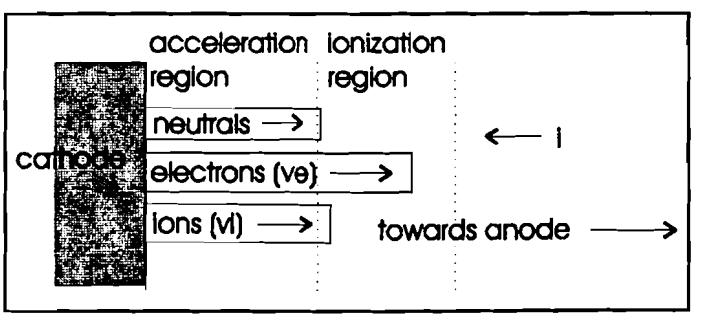

Figure 2-2: Definition of the directions used in formula (2-1).

$$i = Ae\left(n_e v_e - z n_i v_i\right) \qquad (2\text{-}1)$$

i	= current	[A]
A	= arc cross section	[m2]
e	= elementary charge	[C]
n_e	= electron density	[m^{-3}]
v_e	= electron velocity in axial direction	[m/s]
z	= average ion charge number	
n_i	= ion density	[m^{-3}]
v_i	= ion velocity in axial direction	[m/s]

The arc voltage in the diffuse arc mode is quiet and low and except for some possible sputtering no erosion occurs at the anode.

The footpoint mode is an intermediate arc mode. In this mode one or more luminous spots appear on the anode surface. These footpoints often are associated with anode spots. This is not correct because footpoints erode the anode surface only lightly while an anode spot causes gross melting. The temperature of the footpoints is measured to be near the melting point of the anode material. The formation of footpoints is usually accompanied by an increase in mean arc voltage and high frequency voltage oscillations.

During the anode spot mode a very bright anode spot is visible and the temperature of this spot is near the atmospheric boiling point of the anode material. Considerable erosion of the anode occurs during this arc mode. In this mode both the anode and the cathode act as a plasma source. The arc voltage is most of the time low and quiet but can have some high peaks.

The intense arc mode is a high current mode that can occur at small contact gaps. During this mode both the cathode and the anode are eroded severely because large melted areas are formed on both the contacts. Of course both the anode and the cathode are plasma source during this arc mode. The arc voltage is always low and quiet.

From the description above it shall be clear that the anode spot mode and the intense arc mode have to be prevented. A number of theories exist on the formation of the real anode spots. These theories can be divided into three main groups [Mil85]:

- Column Controlled Theories. These theories state that a contraction of current and/or plasma precedes the formation of an anode spot. The anode spot is formed because the contracted arc energy only heats a small part of the surface.

- Anode Controlled Theories. These theories state that a change of the plasma parameters is the onset to the formation of an anode spot. The change of the plasma parameters is caused by the evaporation of anode material. Also the ejection of droplets anode material into the arc is mentioned as a cause of change of the plasma parameters.

- Anode-Column Interaction Theories. These theories form a combination of the first two types of theories. Both the effects of the constriction of the arc and the evaporation of anode material are accounted for in these theories.

Although there is experimental evidence for all three types of theories, the anode-column interaction theories seem to provide the best results in comparison with the measurements [Mil85]. In chapter 5 a model of the formation of an anode spot will be presented.

During the arc phase the contacts influence the formation of an anode spot in two different ways. On the one hand through the characteristics of the contact materials and on the other hand through the generation of an axial or transverse magnetic field.

2.1.2 Influence of the contact material

The thermal characteristics of the anode material greatly influence the formation of an anode spot. A higher melting and boiling temperature of the anode material of course delays or prevents the formation of an anode spot. A high heat conduction coefficient however is also important for the prevention of an anode spot. A high heat conduction coefficient means a rapid distribution of the absorbed arc energy all over the contact material.

Table 2-1 displays some electrode materials and their thermal characteristics in comparison to the average threshold current density for anode spot formation. The average threshold current density is defined as the current at which an anode spot forms, divided by the contact surface area. The average threshold current densities are taken from [Mil83] and the thermal characteristics are taken from [CRC82] and [BIN86].

Table 2-1: A comparison of the thermal properties of the contact material and the average anode spot threshold current density.

Electrode material	T_m [K]	T_v [K]	λ [$Wm^{-1}K^{-1}$]	$\kappa \cdot c_s$ [$Jm^{-3}K^{-1}$]	J_{ac} [Am^{-2}]
Sn	505	2543	64	$1.75 \cdot 10^6$	$9.0 \cdot 10^6$
Al	933	2740	237	$2.97 \cdot 10^6$	$2.7 \cdot 10^7$
Ag	1234	2485	450	$2.94 \cdot 10^6$	$3.8 \cdot 10^7$
Cu	1356	2840	483	$4.48 \cdot 10^6$	$4.0 \cdot 10^7$
Mo	2883	5833	138	$2.65 \cdot 10^6$	$5.3 \cdot 10^7$
W	3683	5933	235	$2.61 \cdot 10^6$	$5.4 \cdot 10^7$

T_m	= melting temperature	[K]
T_v	= boiling temperature	[K]
λ	= heat conduction coefficient	[$Wm^{-1}K^{-1}$]
κ	= mass density	[kgm^{-3}]
c_s	= specific heat	[$Jkg^{-1}K^{-1}$]
J_{ac}	= average anode spot threshold current density	[Am^{-2}]

From Table 2-1 it can be concluded that materials with high boiling temperatures can be used best to prevent the formation of anode spots. This assumption is only correct for the anode material. Research has shown that cathode materials with low boiling temperatures give higher average threshold current densities than cathode materials with high boiling temperatures when the same anode material is used. The anode material however influences the formation of an anode spot more than does the cathode material [Mil85].

An increase of the average threshold current density for cathode materials with low boiling temperatures can be correlated to a less contracted arc. Contact materials with low boiling temperatures produce plasmas with a high particle density. These plasmas often have a lower Hall parameter $\omega_e\tau_{ei}$ (where ω_e is the electron cyclotron frequency and τ_{ei} the electron-ion collision time) than have plasmas with a low particle density [Aga84]. A lower Hall parameter implies less contraction of the arc due to the Hall effect [Izr85]. Less contraction of the arc implies that a larger contact surface area is used to transfer the arc energy resulting in anode spot formation at higher currents.

Vacuum circuit breakers however are used mainly in power frequency networks and therefore cannot have different cathode and anode materials without special measures to control the direction of the current. The contact material therefore has to be an optimum between the materials with high and low boiling temperatures.

2.1.3 Influence of the contact geometry

Contacts with special geometries can generate axial or transverse magnetic fields. These axial or transverse magnetic fields help to prevent or to delay the formation of an anode spot. Although the contacts used in vacuum circuit breakers can have a variety of geometries [Beh84], [Yan85], [Sch93-1], [Sch93-2], this paragraph will be limited to three basic contact types:

- Butt Contacts. These contacts do not generate an axial or transverse magnetic field. The interruption capacity depends on the diameter of the contact and the contact material.

- Spiral Contacts. These contacts generate a transverse magnetic field. The interruption capacity depends on the transverse magnetic field, the diameter of the contacts and the contact material.

- Coil Contacts. These contacts generate an axial magnetic field. The interruption capacity depends on the axial magnetic field, the diameter of the contacts and the contact material.

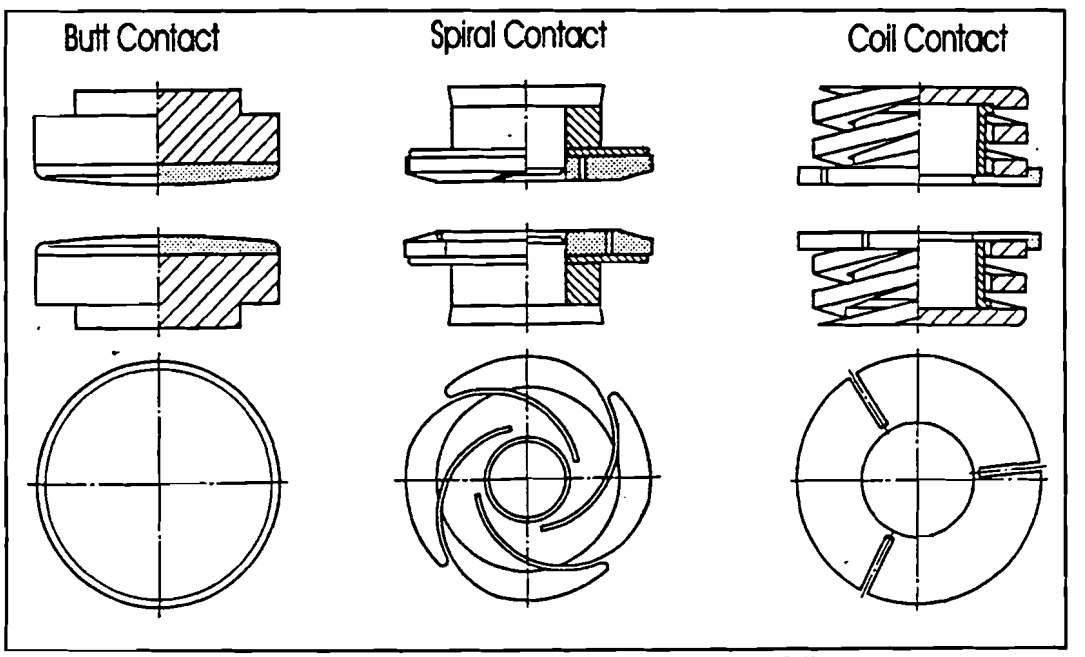

Figure 2-3: Drawings of the three types of contacts [Beh84].

Spiral contacts generate a transverse magnetic field. Because of this magnetic field a Lorenz force will force the arc to run azimuthally on the peripheral edge of the contact. The movement of this arc is nicely photographed by Behrens [Beh85] and in one of his articles Schulman presents a nice outline of the arc behavior when spiral electrodes are used [BSc93].

Because of the fast movement of the arc along the peripheral edge of the contacts (50 - 170 m/s [Beh85]) the absorbed arc energy is distributed more evenly over the contact surface. In this way strong local heating of the anode contact is prevented and the formation of an anode spot prevented or delayed.

In vacuum arcs electrons and ions have the tendency to follow the magnetic field lines. This characteristic is used in coil contacts. Coil contacts generate an axial magnetic field. This axial magnetic field has a dual effect:

- The axial magnetic field opposes the pinching effect of the azimuthal magnetic field that is generated by the arc current [Izr85], [Nem89], [Sha89], [Wie89].

- The axial magnetic field confines the highly ionized plasma to the gap region so the charge carriers cannot recombine on the shield of the vacuum tube [Yan87], [BSc94], [Wat96-1].

The two effects mentioned above cause the arc to stay in the diffuse mode at higher arc currents.

Considering Behrens [Beh83] it can be concluded that a coil contact has a better interruption capacity than has a spiral contact of the same diameter and the same material. Great care has to be taken with this conclusion because newly designed spiral contacts can have improved interruption capacities.

Because in the present work coil contacts were used some remarks about the axial magnetic field have to be made.

Using coil contacts the axial magnetic field is generated by the circuit current. This results in a sinusoidal axial magnetic field that has a slight phase shift with respect to the arc current [BSc94]. Calculations of necessary axial magnetic field strengths often give a dc-value. This dc-value has to be compared to the sinusoidal value of that moment.

The effect of the axial magnetic field is also correlated to the contact material [Aga84]. As already mentioned contact materials with a low erosion rate produce less plasma than do contact materials with a high erosion rate. A low particle density plasma often has a larger electron Hall parameter which implies a stronger contraction of the arc current due to the Hall effect [Izr85]. The effect of the axial magnetic field on these strongly contracted arcs will be more evident than in the case of moderately contracted arcs.

The influence of the diameter of the contacts on the interruption capacity has been mentioned a few times already. According to Behrens [Beh84] the interruption capacity of a certain type of contact increases linearly with increasing diameter. Behrens however does not measure an increase in interruption capacity for coil contacts with diameters larger than 60 mm. Yanabu [Yan87] and Watanabe [Wat96-1] though measured a linear increase in interruption capacity for coil contacts with diameters up to 200 mm. Careful comparison of the contact material, contact geometry and contact fabrication process is necessary to explain this difference. It can be stated however that the interruption capacity of a certain type of contact increases with increasing diameter.

2.2 Recovery phase

After current zero the so called recovery phase starts. Just before current zero a low impedance plasma exists between the contacts. The electrons now are decelerated to meet the required circuit current. The ions in the plasma are much heavier and do not change their speed so quickly. Just after current zero the former anode becomes the new cathode and the electrons will quickly change direction and disappear to the new anode, leaving a positive ion space charge near the new cathode. These ions will continue their journey to the new cathode. The plasma particles that do not reach one of the contacts disappear quickly in the background vacuum because of the large difference in pressure between the arc and the background vacuum. These effects result in the so called post arc current which decays within a microsecond.

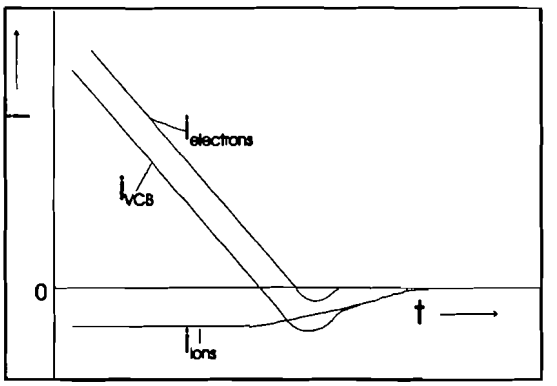

Figure 2-4: Sketch of a typical post arc current consisting of electron and ion current [Bin95].

The post arc current is closely related to the particle density after current zero and is an important factor in the interruption. The peak of the post arc current and the total charge of the post arc current will increase when more plasma is present after current zero. Contact materials with higher vapor pressures will therefore have larger post arc currents [Yan85][Yan86] and the chance on reignition becomes larger.

Besides the contact material the contact geometry also can influence the post arc current. This is the case when large currents have to be interrupted. Contact geometries that prevent or delay the formation of an anode spot will also have smaller post arc currents compared to normal butt contacts [Yan85][Yan86]. The main reason for this effect is of course the lower temperature of the anode. A lower anode temperature means less plasma at current zero and a smaller post arc current.

After the disappearance of the plasma a recovery voltage appears across the gap that can have an amplitude of twice the circuit voltage and a frequency of some ten kHz depending on the circuit configuration [Sme94].

Two main types of reignition can be distinguished:

- Dielectric reignition;
- Thermal reignition.

Dielectric reignition mostly occurs in situations where the arc current and arcing time have been small and sharp edges are present on the contact. Of course this type of reignition becomes more important at smaller contact gaps.

The arc current and arcing time have to be small for dielectric breakdown of the gap because in this situation the arc is in the diffuse mode and the cathode is the only plasma providing contact. On the cathode plasma is produced in so called cathode spots that have a diameter of several μm [Daa78]. These cathode spots will cool down very quickly so only a few microseconds around current zero are decisive for a successful interruption. After these few microseconds the roughness of the contacts and the electric field strength decide whether reignition occurs or not. The upper part of Figure 2-5 shows a typical dielectric reignition.

In the case of large arc currents and long arcing times the anode will also produce plasma. In this case an anode spot is often present. An anode spot is, as mentioned before, a large (several mm^2) melted area. These anode spots therefore need more time to cool down and one has to think in milliseconds of cooling time [Wat96-1], [Wat96-2]. Metal vapor will still be emitted after current zero because of these long cooling times.

The evaporation of metal after current zero will reduce the dielectric strength of the contact gap considerably. The metal vapor will be ionized by accelerated electrons and ions. These electrons and ions in turn are accelerated by the recovery voltage. The reignition voltage as a result will be considerably lower than in the case of absence of an anode spot. The middle part of Figure 2-5 shows a typical example of such a combined dielectric and thermal reignition. When the amount of emitted vapor is so large that no significant reignition voltage is measured one speaks of a thermal reignition. The bottom part of Figure 2-5 shows a typical example of a thermal reignition.

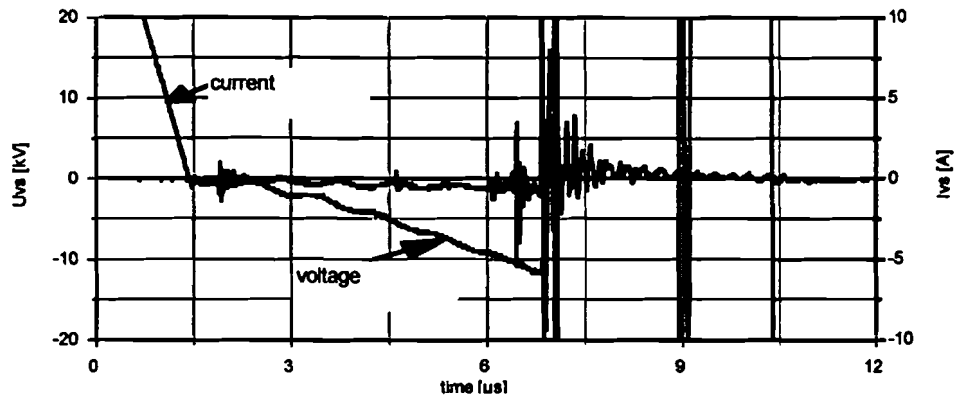

A typical dielectric reignition.

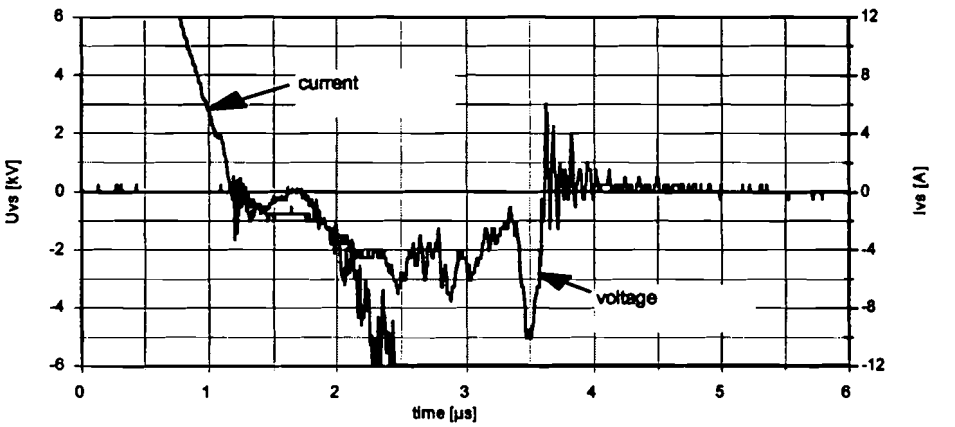

A typical combination of a dielectric and a thermal breakdown.

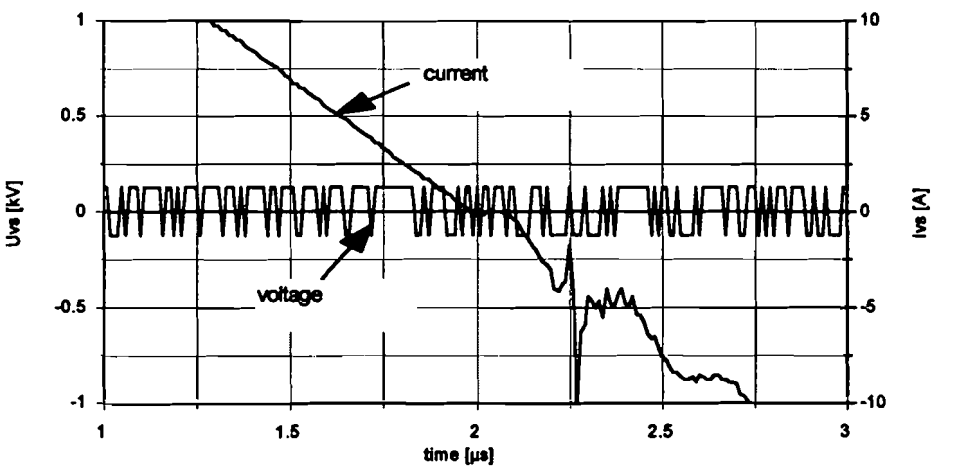

A typical thermal reignition.

Figure 2-5: Typical reignition types.

3. Measurements

This chapter discusses the measuring equipment, some typical measurements and a special post arc current phenomenon.

3.1 Measuring equipment

This paragraph will give a survey of the measurement equipment and the methods used in this investigation. Information on the used equipment can also be found in appendix A.

3.1.1 The synthetic circuit

A Weil-Dobke synthetic circuit is used to perform the interruption measurements. Except for some component values, the Weil-Dobke circuit used here is the same as the circuit used by Binnendijk [Bin95] and Macken [Mac94]. Figure 3-1 shows the used Weil-Dobke synthetic circuit. The circuit is suitable to perform interruption measurements with currents between 10 kA and 35 kA.

At the start of an interruption measurement, the minimum oil circuit breaker S1 is open and the vacuum circuit breakers S2 and VS are closed. Capacitor C_m is charged to a voltage between 1.5 kV and 15 kV, depending on the required amplitude of the "main current". Capacitor C_{inj} is always charged up to a voltage of 15 kV at the beginning of an interruption measurement.

The capacitor battery (C_m) and the transformer (T1) form the "main current" part of the circuit. The LC-loop formed by this capacitor and this transformer supplies a sinusoidal "main current" (i_m) with a frequency of 36.4 Hz and an amplitude up to 50 kA.

The "main current" is triggered by closing the circuit breaker S1. Vacuum circuit breaker S2 is used to isolate the "main current" part of the circuit from the "injection" part of the circuit and is opened just after the top of the main current. Vacuum circuit breaker VS has a sectional vacuum chamber in which the contacts used in this investigation are placed. The time at which vacuum circuit breaker VS is opened depends on the required contact gap at current zero. Appendix B shows a drawing of the sectional vacuum tube.

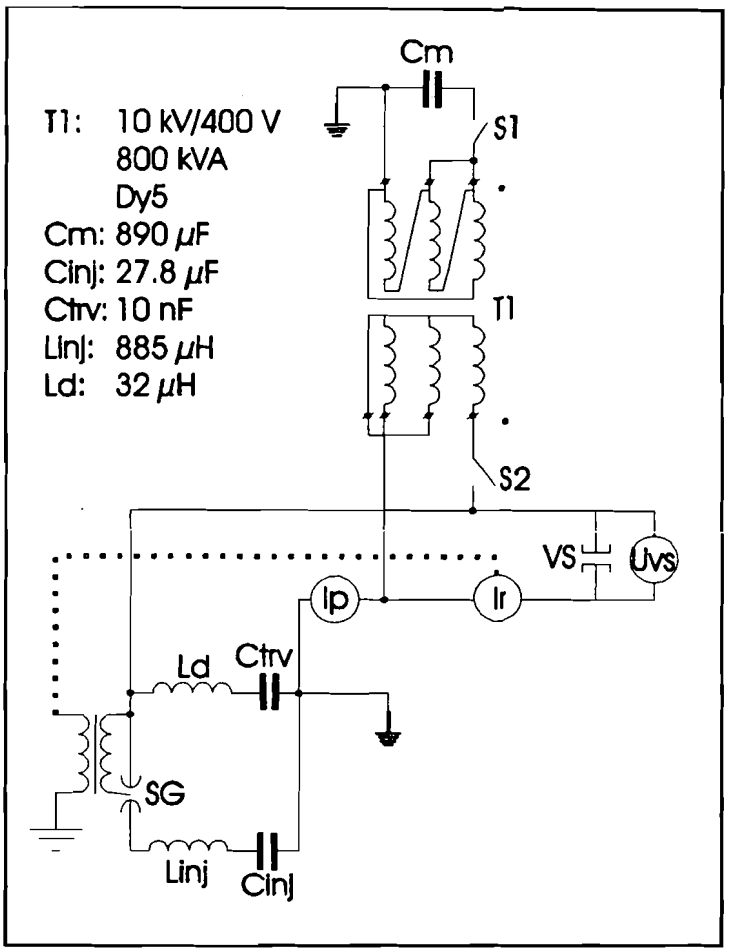

Figure 3-1: The synthetic circuit.

The "main current" is measured with a Rogowski coil (Ir) with matching integrator. The sensitivity of this combination is 25.3 kA/V.

The readings of the current Ir are also monitored by a triggering device for the spark gap (SG). Just before the first current zero of the "main current" this triggering device fires the spark gap and an "injection current" (I_{inj}) will start to flow.

The LC-loop formed by L_{inj} and C_{inj} supplies a sinusoidal "injection current" with a frequency of 1 kHz and an amplitude around 2.9 kA. This "injection current is measured with a Pierson current transformer (Ip) which has a sensitivity of 200 A/V. The current transformer output is clipped by two diode arrays consisting of 10 parallel diodes each and switched anti parallel. The diode arrays prevent saturation of the transformer core.

The injection current delays the current zero in circuit breaker VS but not in circuit breaker S2. The arc in vacuum circuit breaker S2 therefore will extinguish before the arc in vacuum circuit breaker VS extinguishes. The advanced current zero of the current through vacuum circuit breaker S2 therefore provides a safe isolation of the "main current" part of the synthetic circuit from the other parts of the circuit at the time of current zero in vacuum circuit breaker VS.

If the circuit breaker VS succeeds in interrupting the current at a current zero, the "injection current" commutates through the damping coil L_d into the capacitor C_{trv}. The LC-loop formed by L_{inj}, L_d, C_{inj} and C_{trv} gives a sinusoidal recovery voltage (U_{trv}) with a frequency of 51 kHz and an maximum amplitude around 20 kV. The maximum amplitude of the recovery voltage depends a little on the amount of residual plasma present after current zero.

3.1.2 Measuring the arc voltage

The arc voltage has a value around 40 V most of the time. This low voltage is measured with a 1000:1 probe so the oscilloscope receives a signal with an amplitude around 40 mV. The probe measurement is necessary because of the high recovery voltage between the contacts immediately after interruption of the current.

Although great care has been taken to avoid electromagnetic interference (EMC) problems, the arc voltage could not be measured without some induced interference. A careful layout of the measuring circuit had already minimized this induced interference.

Because of the use of shielded coaxial high voltage cables the induced interference on the arc voltage has a rather constant pattern. This constant pattern enables a mathematical correction of the induced interference.

Figure 3-3 shows the induced interference of the "main current" and the "injection current" with the contacts of the circuit breaker VS closed. When the contacts of circuit breaker VS are closed, the measured arc voltage should be zero.

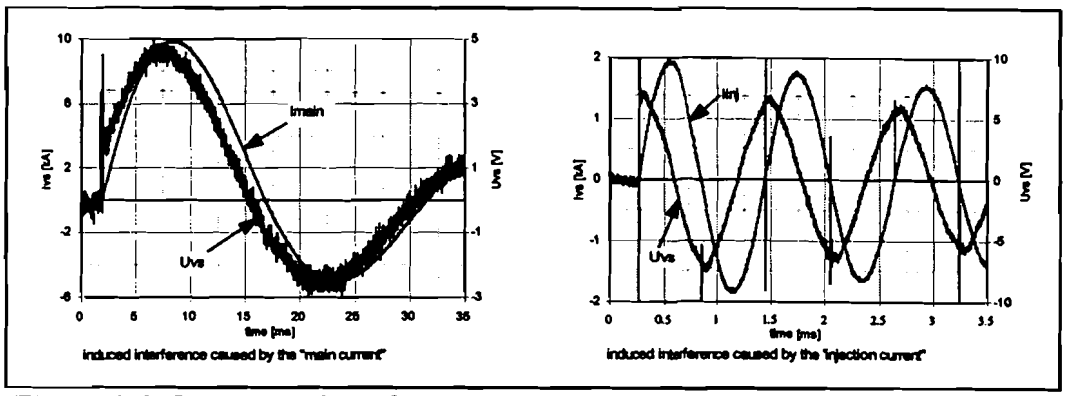

Figure 3-3: Measured interference induced by the circuit current.

The measured arc voltages of Figure 3-3 can be modeled by assuming a resistor and a coil in series with the ideal contacts, as is drawn in Figure 3-2. This assumption leads to a mathematical correction of the measured arc voltage as is given by formula (3-1):

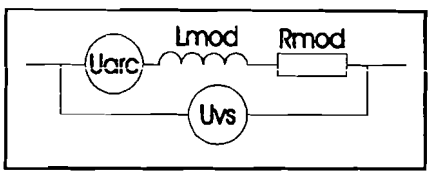

Figure 3-2: Model of the measured arc voltage.

$$U_{arc}(t) = U_{vs}(t) - 2\pi f I L_{mod} \cos(2\pi f t) - R_{mod} i(t) \qquad \textbf{(3-1)}$$

U_{arc}	= arc voltage	[V]
t	= time	[s]
Uvs	= measured arc voltage	[V]
f	= frequency of the sinusoidal current	[Hz]
I	= maximum amplitude of the current	[A]
L_{mod}	= model reactance	[H]
R_{mod}	= model resistance	[Ω]

Formula (3-1) is used for both i_{main} and i_{inj}. The parameters of the "main current" should therefore be used to correct the measured arc voltage during the "main current" phase and the parameters of the "injection current" should be used to correct the arc voltage during the injection phase.

Using the induced voltages with closed contacts (Figure 3-3), the values of L_{mod} and R_{mod} can be determined. The value found for L_{mod} is $7 \cdot 10^{-7}$ H and the value found for R_{mod} is $4 \cdot 10^{-4}$ Ω. The value for R_{mod} is sensitive for the condition of the contacts but is assumed to be constant during this investigation. The value of L_{mod} is also assumed to be constant during this investigation.

The measured arc voltage was corrected by using a spread sheet program to correct each sample according to formula (3-1). Figure 3-4 gives the result of such a correction.

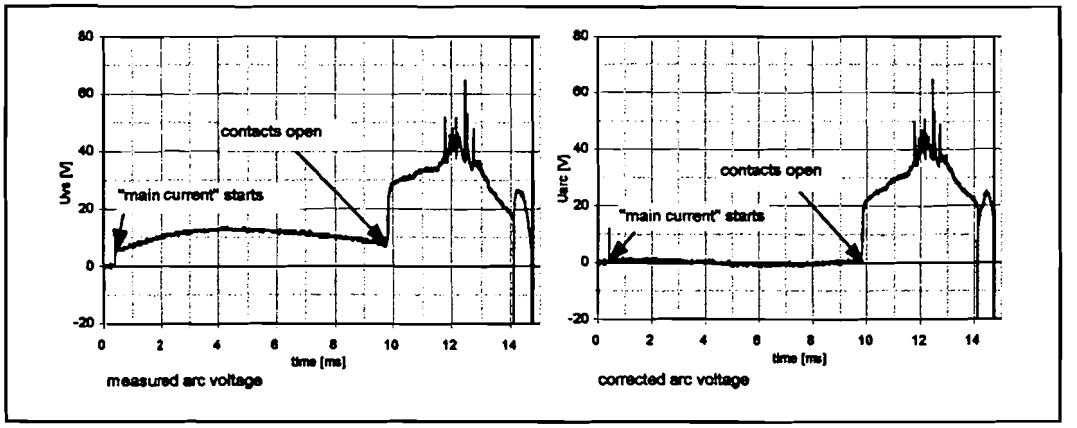

Figure 3-4: Example of a corrected arc voltage.

3.1.3 High speed camera

The light emitted by the arc was recorded by a high speed camera designed at KEMA.

The high speed camera has a 16 X 10 matrix of glass fibres. Each fibre is connected to an optical receiver. The signals of the optical receivers are converted by 4-bits A/D converters that show a logarithmic conversion characteristic. With these characteristics the camera gives an image of 16 X 10 pixels of the arc and every pixel has sixteen light intensity levels, with a ratio of $\sqrt{2}$ between adjacent levels.

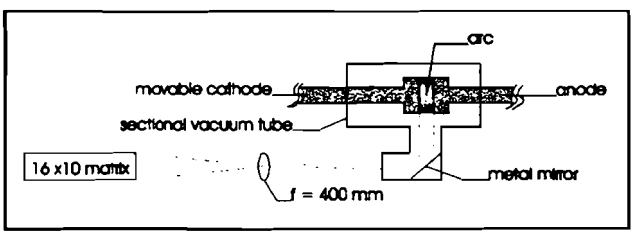

Figure 3-5: Setup of the high speed camera used to record the light emitted by the arc.

The maximum sample rate of the camera is 10^6 images/second and the camera has a memory for 1638 images. The sensitivity of the optical receivers can be adjusted by changing a reference voltage.

In Figure 3-5 the setup of the camera is drawn. An example of the images produced by the camera is given in Figure 3-8d and Figure 3-10b in paragraph 3.2.

Small arc currents require a very sensitive camera recording. Two or three columns of the 16 X 10 matrix suffered from noise at this high sensitivity setting of the camera. Higher arc currents required a less sensitive setting of the camera and did not give noise problems.

Very high arc currents however required a very low sensitivity of the camera during the "main current" phase. The required sensitivity was too low to record any reignitions. Very high arc currents therefore had to be recorded twice with different settings of the sensitivity of the camera.

3.1.4 Other equipment

An ion getter pump is used to keep the pressure in the sectional vacuum tube below 10^{-6} mbar. The pressure inside the sectional vacuum tube was measured indirectly by relating the current of the ion getter pump to the pressure inside the tube.

A fast laser displacement measuring system was used to record the opening of the contacts. The accuracy of the laser system is 0.2 mm. The laser system however suffered from some interference during current zero crossings of the circuit current.

The contact opening mechanism is almost the same as used by Binnendijk [Bin95]. Only a slight modification has been made in order to increase the contact closing force from 320 N to 390 N. This increase in closing force was necessary to withstand the electrodynamic popping forces up to currents of 35 kA.

An increase of the closing force also implies an increase in opening speed of the contacts. The opening speed of the modified mechanism is around 1.75 m/s. An example of the opening of the contacts, measured by the laser system, is given in Figure 3-6.

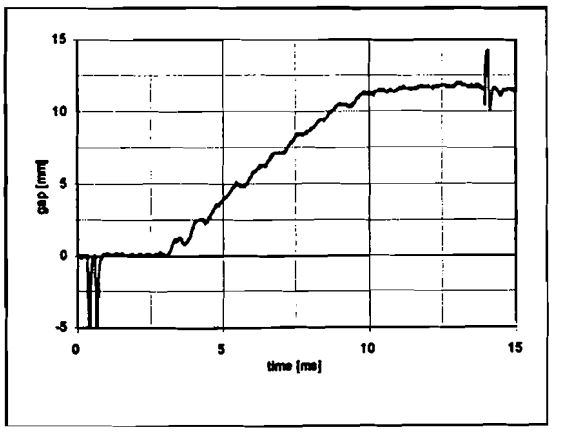

Figure 3-6: Opening of the contacts measured by the laser system.

One of the parameters of an interruption measurement is the contact gap at current zero. The construction of the switching mechanism however does not allow an individual adjustment of arcing time and contact gap at current zero. This means a certain contact gap at current zero is correlated to a certain arcing time. An increasing contact gap at current zero also implies an increasing arcing time. Scientifically spoken it is not nice to change two parameters at the same time but it does give a good representation of reality where contact gap at current zero and arcing time also are coupled parameters.

In order to measure the electrode erosion rate, the weight of the contacts before and after the interruption measurements was determined. A Sartorius AC 210 balance with an accuracy of 0.1 mg was used to determine the weight of the contacts.

3.2 Typical measurements

Figure 3-7, Figure 3-8 and Figure 3-9 give an example of the results obtained by an interruption measurement. The results shown are obtained from an interruption measurement done with Toshiba's CuCr contacts that generate an axial magnetic field.

The letters A to G, placed at the top of the Figure 3-7a, b, c, and Figure 3-8e, f, each denote a time interval. This time interval is the same as the time interval of the corresponding row in the recording of the camera (Figure 3-8d).

Figure 3-7a shows the current through the vacuum circuit breaker VS. This figure clearly shows three reignitions, one immediately and two more after a short delay.

Figure 3-7b shows the opening of the contacts. The laser displacement measuring system suffers from interference during current zero crossings as mentioned before. Nevertheless the contact gap can be determined without problems.

Figure 3-7b also shows the contact gap becomes smaller after reaching its maximum around 12 ms. This is caused by the mechanical tolerance in the switching mechanism. Reaching the maximum opening of the switching mechanism, the contacts bounce and make a little oscillation before they come to rest with a contact gap around 6 mm. The minimum contact gap during the oscillation is around 4 mm.

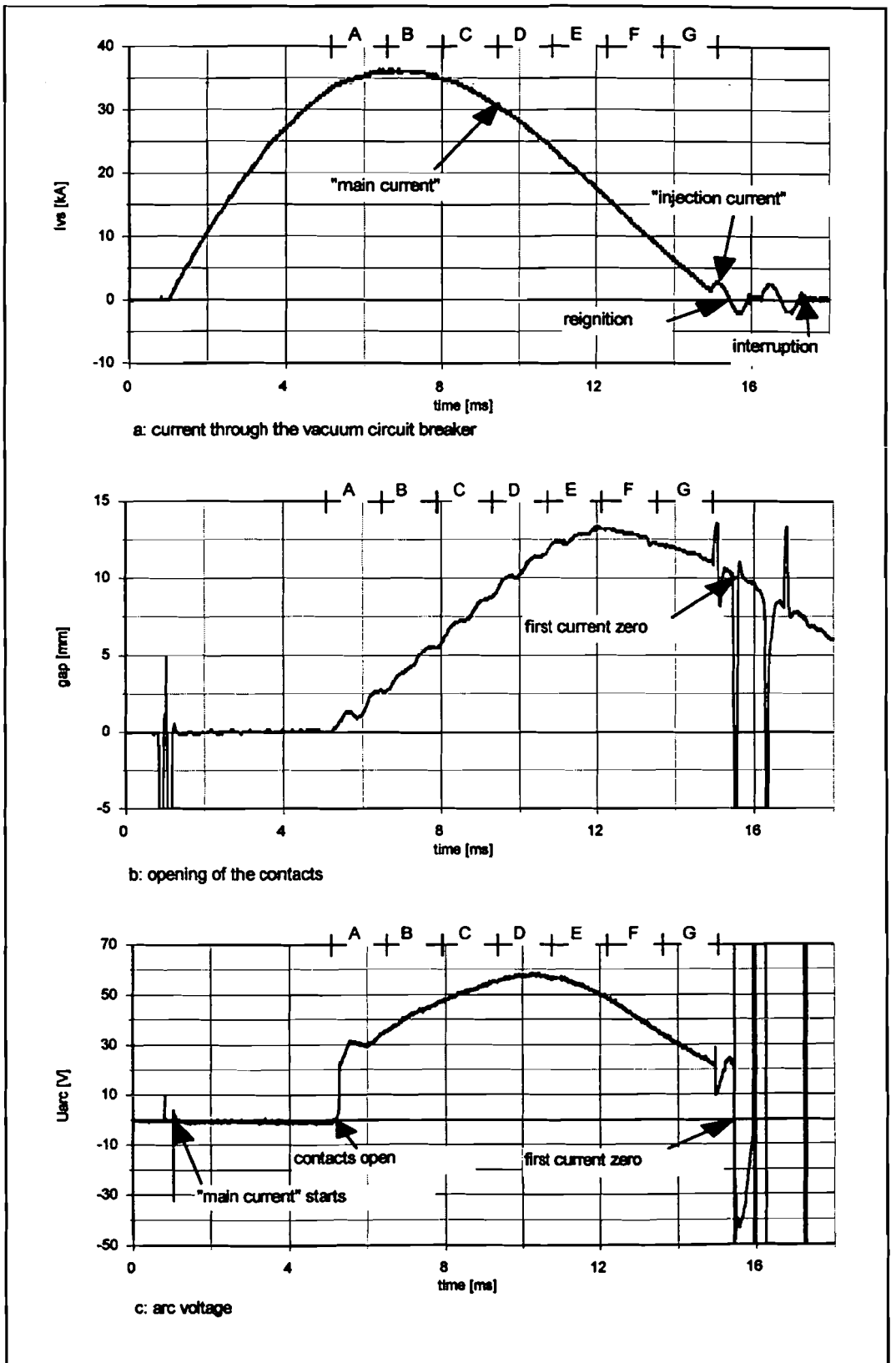

Figure 3-7: An example of the measured current, contact opening and arc voltage.

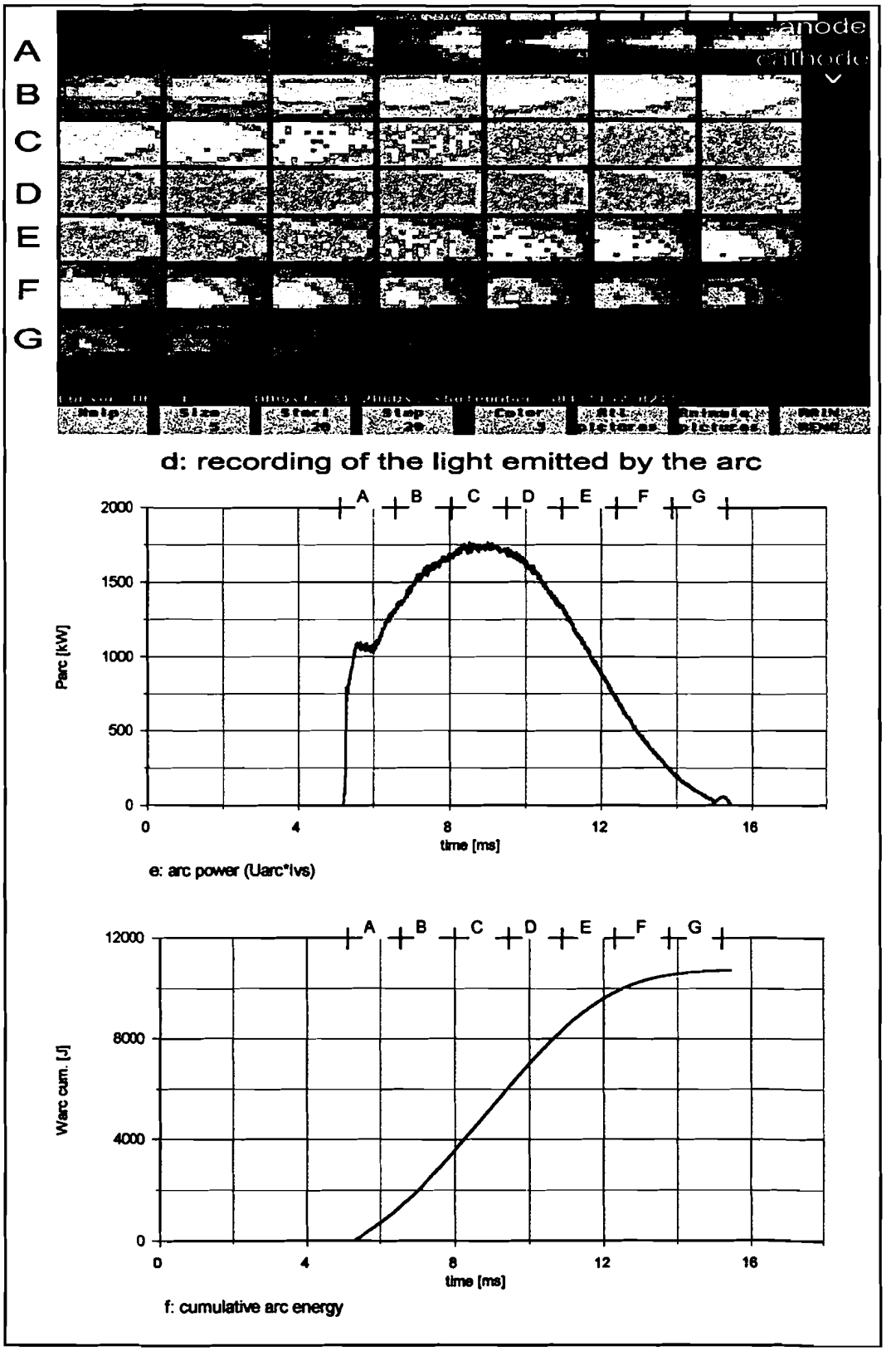

Figure 3-8: An example of the recording of the light emitted by the arc, the arc power and the cumulative arc energy.

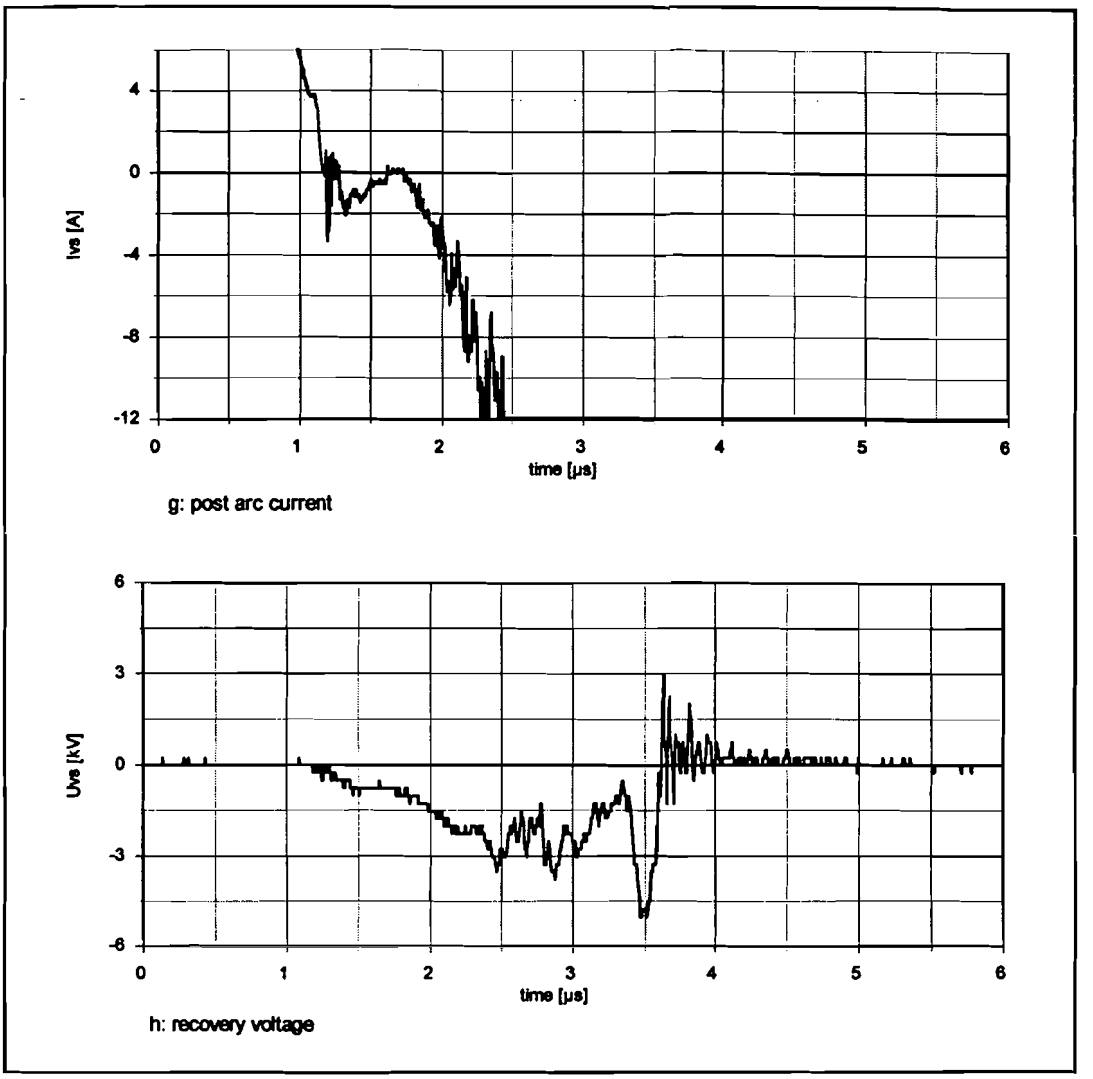

Figure 3-9: An example of the measured post arc current and the recovery voltage.

Figure 3-7c shows a corrected measurement of the arc voltage. The arc voltage is corrected up to the first current zero. The correction is made according the ideas of paragraph 3.1.2.

The example shown, is a measurement done with Toshiba's CuCr contacts that provide an axial magnetic field (AMF). All the measurements with the AMF contacts show arc voltages that resemble the arc voltage of Figure 3-7c. No spikes occur on the arc voltage but the arc voltage seems to be made up from the addition of a constant ionization voltage and a variable voltage caused by the resistance of the plasma.

Figure 3-8d shows the recording of the light emitted by the arc. To be able to record some useful information during the main current phase of a 37 kA arc current, the camera has to be set at a low sensitivity. Reignitions however can not be observed because of this low sensitivity. At the end of this paragraph Figure 3-10 will give the recording of some reignitions during an other interruption measurement.

The position of the contacts is not always clearly visible on the recording of the camera. As can been seen in Figure 3-8d, high currents will cause the arc to expand around the contacts and therefore the contacts can no longer be seen. At the end of row A in Figure 3-8d however the arc has not yet expanded around the contacts and two horizontally placed electrodes can be drawn into the picture. The top electrode is the anode that will keep this position during the measurement. The bottom electrode is the cathode that will move downwards with increasing contact gap.

The light emitted by the arc seems to be strongly correlated to the arc power. At the beginning of row C the emitted light is strongest and the arc surrounds the contacts totally. Neither at the maximum amplitude of the current nor at the maximum amplitude of the arc voltage so much light is emitted as there is in the case of the maximum amplitude of the arc power.

After a decrease in light intensity there again is a very bright arc visible at the beginning of row F. At the beginning of row F however the arc current, arc voltage and arc power are rather low and an even lower light intensity than in the case of row D is expected. The most likely explanation for this phenomenon is the formation of a contracted arc. The cone shaped light of row F also points to an arc that is contracted near the anode.

The very hot anode surface (more than 10 kJ of arc energy has been dissipated) obviously provides the circumstances for the arc to become contracted at these low currents. The reduced circuit current also reduces the generated axial magnetic field Although the reduced axial magnetic field also plays a role in the formation of a contracted arc, the hot anode surface here is necessary to give these images of a contracted arc. These results differ from those of Watanabe [Wat96-1] where contraction is only assumed around current maximum.

Figure 3-8e shows the arc power. Figure 3-8e has been constructed by multiplying each sample of the corrected arc voltage with the corresponding sample of the arc current. The arc power has been calculated from the opening of the contacts to the first current zero.

Figure 3-8f shows the cumulative arc energy. Figure 3-8f has been constructed by taking the integral of Figure 3-8e.

As already noticed by Binnendijk [Bin95], the maximum cumulative arc energy is an important parameter to characterize the performance of the contacts. It however requires a lot of computer time and hard disk space to calculate the maximum cumulative arc energy when using all the measurement data. To overcome this problem a mathematical approximation of the maximum cumulative arc energy, that requires less measurement data, has been used. This approximation is checked by comparing the results to a limited number of measurements that are worked out like the one in Figure 3-7 and Figure 3-8.

When calculating the maximum cumulative arc energy with the mathematical approximation, the main problem is the unknown arc voltage. The arc voltage, as already mentioned, seems to be made up from the addition of a constant ionization voltage and a variable voltage caused by the resistance of the plasma. In the calculation used here, the resistance of the plasma is assumed to vary linearly with the contact gap. Furthermore a constant contact opening velocity v_c is assumed. This contact velocity v_c is equal to the contact gap at the first current zero divided by the arcing time. With these assumptions the arc voltage can be written as:

$$U_{arc}(t) = U_0 + \rho_p v_c\left(t - \left(t_{cz} - t_{arc}\right)\right) i(t) \qquad \textbf{(3-2)}$$

U_0	= constant ionization voltage	[V]
ρ_p	= plasma resistance per meter gap length	[Ω/m]
v_c	= constant contact opening velocity	[m/s]
t_{cz}	= time of first current zero	[s]
t_{arc}	= arcing time	[s]

The maximum cumulative arc energy now can be calculated using formula (3-3):

$$W_{arc} = \int_{t_{cz}-t_{arc}}^{t_{cz}} \left[U_0 + \rho_p v_c\left(t - \left(t_{cz} - t_{arc}\right)\right) i(t)\right] i(t)\, dt \qquad \textbf{(3-3)}$$

W_{arc}	= maximum cumulative arc energy	[J]

The current i(t) is made up from the addition of the "main current" and the "injection current". The current during the injection phase is rather small so a constant arc voltage U_0 is assumed during the injection phase. With this assumption formula (3-3) can be written as:

$$W_{arc} = \int_{t_{cz_{main}} - t_{arc}}^{t_{cz_{main}}} \left\{ \left[U_0 + \rho_p v_c \left(t - \left(t_{cz} - t_{arc} \right) \right) I_{main} \sin(2\pi f_{main} t) \right] \right.$$
$$\left. \bullet I_{main} \sin(2\pi f_{main} t) \right\} dt + \int_0^{\frac{t_{inj}}{2}} U_0 I_{inj} \sin(2\pi f_{inj} t)\, dt \qquad (3\text{-}4)$$

$t_{cz\,main}$	= time of current zero of main current	[s]
I_{main}	= maximum amplitude of main current	[A]
f_{main}	= frequency of main current	[Hz]
t_{inj}	= 1/frequency of injection current	[s]
I_{inj}	= maximum amplitude injection current	[A]
f_{inj}	= frequency of injection current	[Hz]

Solving formula (3-4), the following expression is found to calculate the maximum cumulative arc energy:

$$W_{arc} = \frac{U_0 I_{main}}{\omega_{main}} \left(1 + \cos\left(\pi - \omega_{main} t_{arc} \right) \right) + \frac{2 U_0 I_{inj}}{\omega_{inj}}$$
$$+ \frac{\rho_p v_c I_{main}^2}{16} \left\{ \left(2t_{arc} - t_{cz_{main}} \right)^2 + t_{cz_{main}} \left(4t_{arc} - t_{cz_{main}} \right) \right. \qquad (3\text{-}5)$$
$$\left. + \frac{2}{\omega_{main}^2} \left(\cos\left(2\omega_{main} t_{arc} - 2\pi \right) - 1 \right) \right\}$$

ω_{main}	$= 2\pi f_{main}$	[rad/s]
ω_{inj}	$= 2\pi f_{inj}$	[rad/s]

The parameters U_0 and ρ_p in expression (3-5) depend on the contact material and on the contact geometry. The values used for these parameters are listed in Table 3-1.

Table 3-1: Values used to calculate the maximum cumulative arc energy of the contacts.

Parameter	contact type				
	CuCr butt	Cu coil	CuCr coil	CuW coil	AgWC coil
U_0 [V]	13.0	14.0	13.0	17.0	10.0
ρ_p [Ω/m]	0.36	0.31	0.22	0.27	0.21

The values listed in Table 3-1 are experimentally found values. In chapter 4.3 however a possible physical explanation for these experimentally found values will be given.

Finally figure g and figure h of Figure 3-9 show a detailed measurement of current and voltage around the first current zero. Figure g and figure h show a nice example of a combined dielectric and thermal reignition.

After the post arc current, the current immediately increases to values outside the range of this sensitive measurement. This however does not immediately give a reignition but neither allows a normal rise of the recovery voltage. Because of the low recovery voltage (2-3 kV) that is present, the ions and electrons in the post arc plasma are accelerated and there are enough ionizing collisions to start a reignition. The whole process only took about two microseconds.

Figure 3-7a to Figure 3-9h showed an example of the results obtained by a typical interruption measurement. During this measurement the attention was focused on the high current phase and no reignitions were visible on the recording of the camera. Figure 3-10 shows an example of a recording that focuses on the reignitions.

Figure 3-10a only shows the last 8 milliseconds of an interruption of a 13.3 kA current. The contacts open at time 3.7 ms and the contact gap at the first current zero is 11.5 mm. The contact material is AgWC. The first reignition is a pure dielectric reignition that started 25.1 μs after the first current zero.

Figure 3-10b shows the recording of the reignitions by the camera. Again two horizontal electrodes are visible. The one at the top is the original anode and the one at the bottom is the original cathode. The letters A to G at the top of Figure 3-10a, mark the time interval of the corresponding row pictures recorded by the camera.

The anode and cathode exchange takes place at every current zero crossing. Figure 3-10b nicely shows how every reignition starts from the new cathode and than expands towards the new anode.

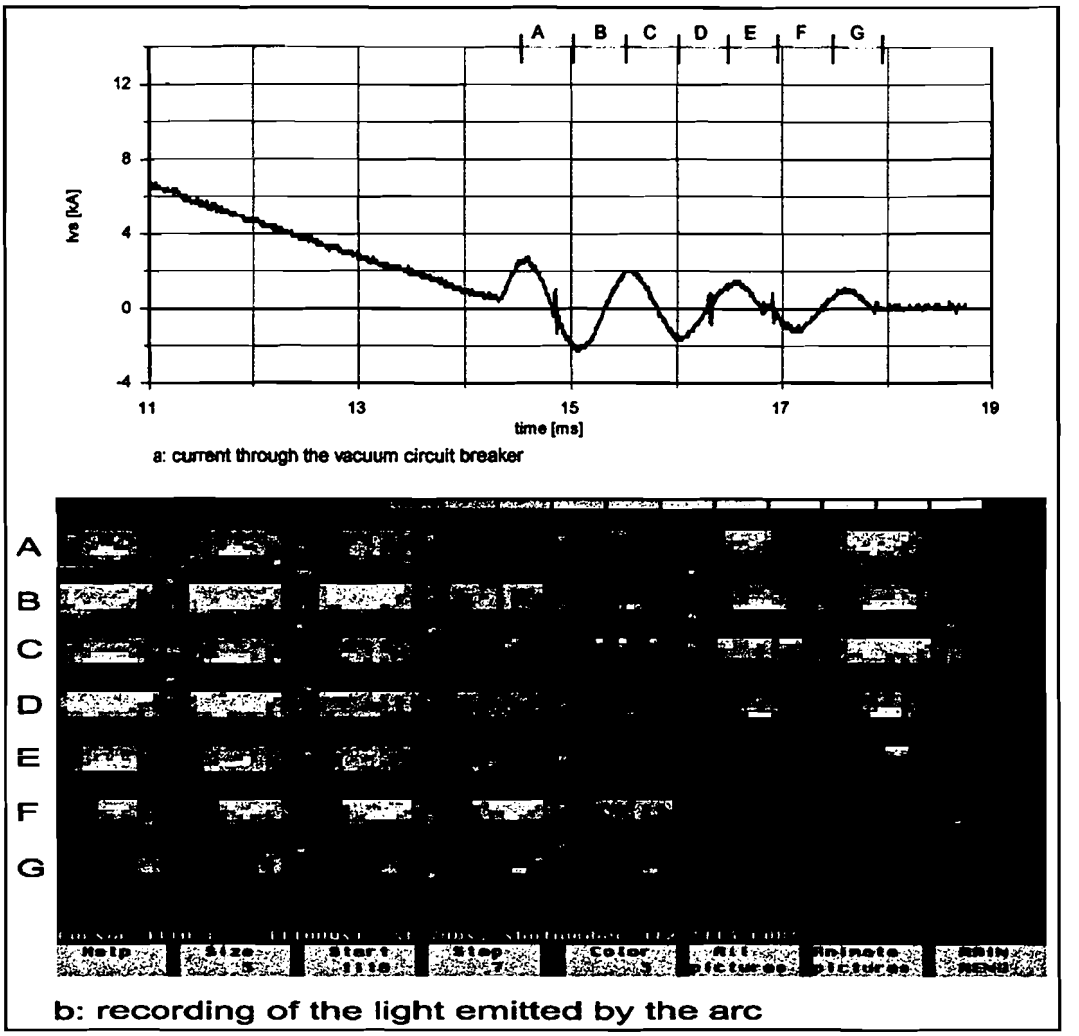

Figure 3-10: An example of reignitions recorded by the camera.

3.3 Current peak after post arc current?

During interruption measurements on the onset of reignition an interesting current peak after the post arc current occurred. This current peak could have an amplitude up to 25 A and could cause oscillations in the recovery voltage.

The current peaks approximately coincide with the first maximum of the derivative of the recovery voltage. A change in frequency of the recovery voltage also caused a change in the time between current zero and the current peak. A higher frequency of the recovery voltage gives a shorter time between current zero and the current peak, as is shown in Figure 3-11.

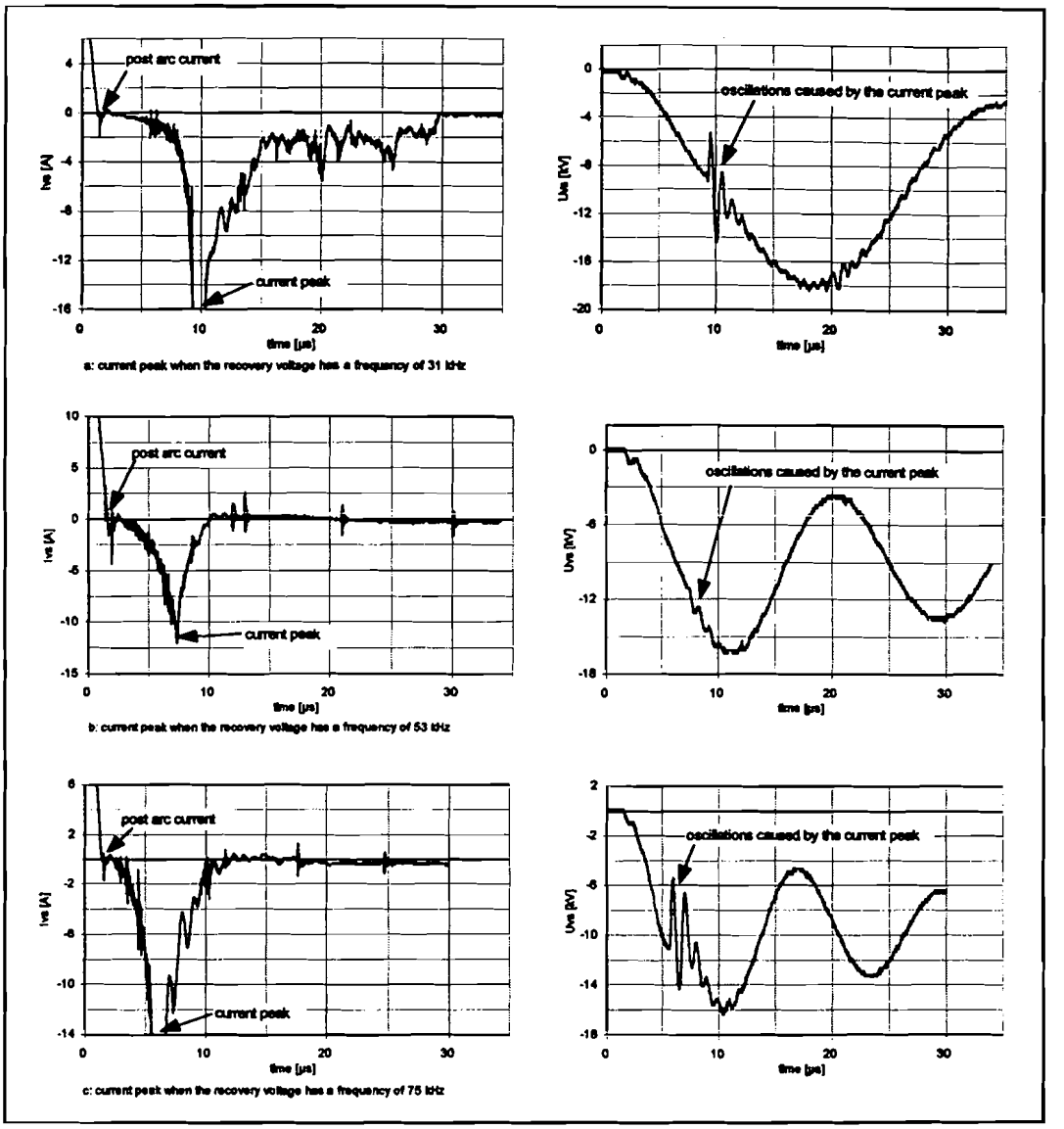

Figure 3-11: Examples of the current peak when the recovery voltage has different frequencies.

The fact the current peak coincides with the maximum derivative of the recovery voltage gives rise to the idea that the current peak is caused by the charging of a capacitor. A capacitor however also would be discharged, so more current peaks should be present. A capacitor therefore can not be the only reason to cause the current peak.

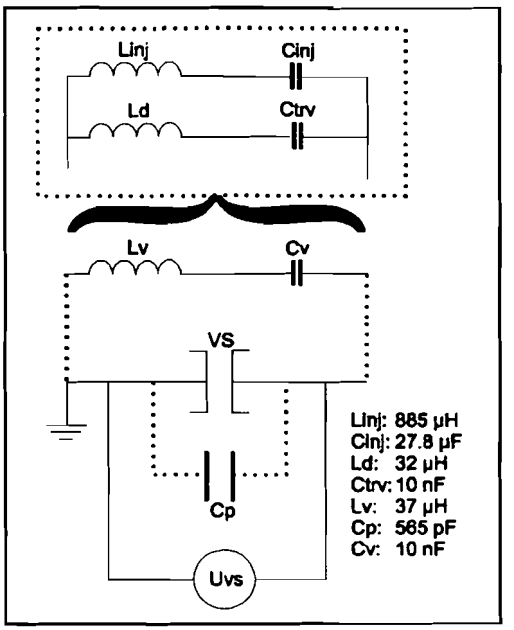

Figure 3-12: Location of the parasitic LC-loop.

During large current peaks, the recovery voltage shows oscillations with a frequency around 1 MHz. These high frequency oscillations of the recovery voltage are caused by a parasitic "LC-loop" in the "injection" part of the circuit. Figure 3-12 shows the location of this parasitic "LC-loop". L_v and C_v are the replacement coil and replacement capacitor for the whole injection circuit. C_p is the parasitic capacitor of the sectional vacuum tube. The coil L_v and the capacitors C_v and C_p were measured with an RLC bridge that was connected to the circuit by the connection clips of U_{vs}.

Capacitor C_p forms a series resonance loop with coil L_v. This resonance loop has a resonance frequency of 1,1 MHz and may be the explanation for the oscillations in the recovery voltage.

It is beyond the reach of this work to investigate in detail the interaction between current peak, parasitic capacitors, used contacts and interrupted current. This paragraph therefore will end with a general remark on a possible interaction between the contact material and the current peak, however, it is strongly recommended to do further investigations into the characteristics of this current peak.

The current peak occurred frequently when using CuCr or CuW as a contact material. Using the contact materials AgWC and Cu not many current peaks occurred. Relating the occurrence of the current peak to the thermal characteristics of the contact materials mentioned in Table 4-3 of paragraph 4.3.2, it seems that contact materials with high boiling temperatures give more current peaks than do materials with low boiling temperatures.

Contact materials with high boiling temperatures can cause higher contact surface temperatures at current zero crossings than in the case of materials with a low boiling temperature. A higher temperature of the contact surface lowers the electric field necessary to draw electrons from the contact material into the residue plasma. An increasing electric field therefore draws more and more electrons into the inter-electrode region and an increasing current is measured. If no reignition occurs the contact surface will cool down with increasing time after current zero and less and less electrons will be drawn into the inter-electrode region. The measured current will decrease again and stay zero.

4. Interruption performance

This chapter describes the interruption performance of the used contacts. Paragraph 4.1 and paragraph 4.2 will make some remarks about the interruption behavior and the condition of the used contacts. In paragraph 4.3 the interruption performance of the used contacts will be compared.

4.1 CuCr contacts without axial magnetic field

The working of the synthetic circuit was checked by using one of the contact types used by Binnendijk [Bin95]. The copper-chromium (CuCr) butt type contacts were used to check the performance of the synthetic circuit.

Figure 4-1 shows a drawing and a photograph of the used butt type contact.

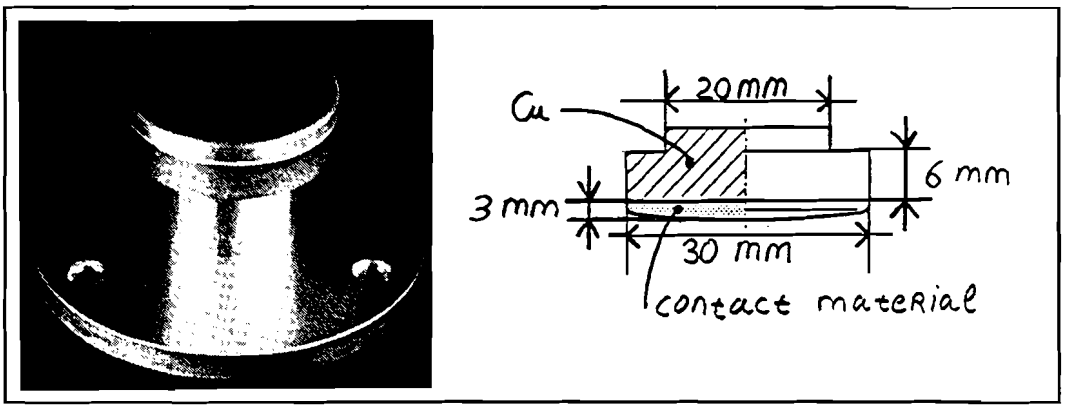

Figure 4-1: Photograph and drawing of the butt type contact used in this work.

Although the same interruption behavior was expected, the interruption performance of the CuCr butt type contacts had significantly improved compared to the results of Binnendijk [Bin95]. A clear definition of the circumstances that caused this difference could not be made. All observations however indicate numerous reignitions along the shield of the sectional vacuum tube during Binnendijk's measurements.

The erosion rate of the cathode was 159.6 μg/C and is similar to the erosion rate of 160.2 μg/C measured by Binnendijk [Bin95]. The erosion rate of the anode was 52.6 μg/C and differs significantly from the 3.6 μg/C Binnendijk [Bin95] measured.

According to paragraph 2.1.1, Binnendijk only measured arcs in the diffuse and footpoint mode and never measured arcs in the anode spot mode. The footpoint mode only causes light erosion of the anode surface while the anode spot mode causes gross melting of the anode surface. During this investigation anode spots occurred and they therefore might explain the higher erosion rate of the anode contact.

The difference in arc appearance can also be seen by comparing the arc voltages. For arcs with energies lower than about 1 kJ, the arc voltage is quiet most of the time. For energies higher than 1 kJ, the arc voltage is high and suffers from severe high frequency oscillations. These high frequency oscillations point to the formation of footpoints and even anode spots may be initiated (paragraph 2.1.1). Figure 4-2 gives an example of a quiet but already high arc voltage at a maximum arc current of 9.6 kA and an example of an high arc voltage with high frequency oscillations at a maximum circuit current of 12.9 kA.

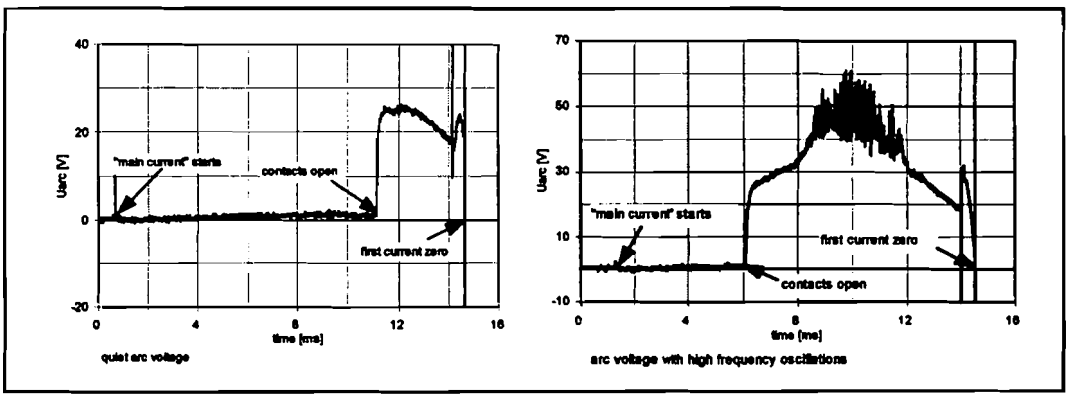

Figure 4-2: An example of arc voltages measured with the butt type CuCr contacts.

Figure 4-3 shows the CuCr butt type contacts after interruption measurements with a total charge of 3316 C and a maximum arc current of 19 kA.

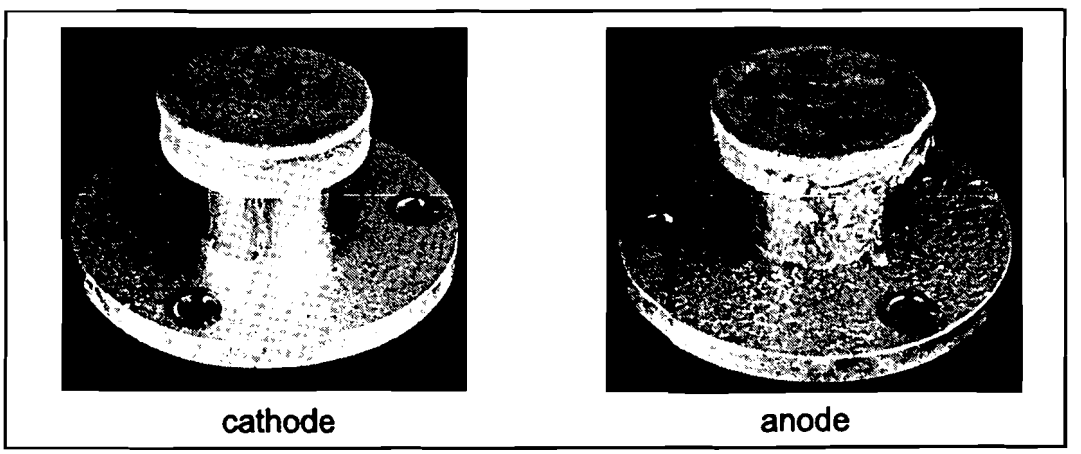

Figure 4-3: The CuCr butt type contacts after the interruption measurements.

As can be seen in Figure 4-3 the cathode is covered with little craters but does not have large melted areas. The anode surface has three large melted areas. The melted areas on the anode are not deep but there has been enough melted material to form a little rim around the contact.

The color of both the contacts is a silver alike, a color suggesting a large chromium concentration is present at the top of the surface. Comparing the boiling temperatures of copper and chromium (Table 4-3, paragraph 4.3.2) gives a much lower boiling temperature for copper than for chromium. Vaporization of copper in the top layer of the surface is possible, resulting in a smaller amount of copper in the copper-chromium mixture.

Both the cathode and the anode have a copper colored spot in the middle of the surface. The diameter of this spot is about 4 mm. The spots may be formed during an intense arc mode.

4.2 Contacts with axial magnetic field

The investigated contacts generating an axial magnetic field (AMF) were all coil type contacts. Figure 4-4 shows a photograph and a drawing of the used coil type contacts.

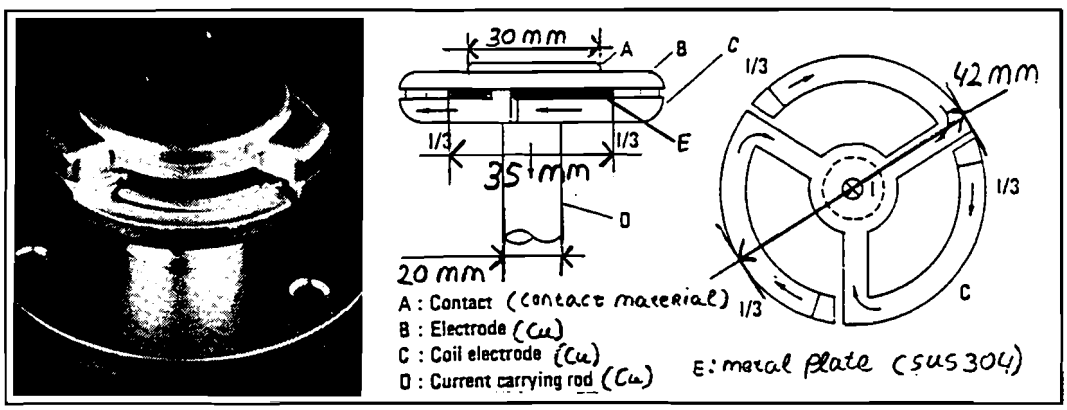

Figure 4-4: Photograph and drawing of the used contacts that generate an axial magnetic field.

A remark about the metal plate denoted as "E" has to be made. This metal plate is used for axial support of the coil electrode. The plate, however, is not connected to the rest of the contact and can move a little bit. After the interruption measurements however this plate was stuck to the contact in most cases. A part of the coil electrode also could become short circuited by molten contact material. A kind of cover around the coil electrode is advised to overcome these problems.

4.2.1 Cu AMF contacts

Copper is a rather strange material. Although the material has a very high erosion rate, the contacts still interrupt the current after one or two current zero crossings and withstand the high recovery voltages. The erosion rate of the copper contacts is 185.0 μg/C for the cathode and 1276 μg/C for the anode.

Figure 4-5 shows the contacts after they had interrupted currents with a total charge of 3324 C and a maximum arc current of 26.69 kA.

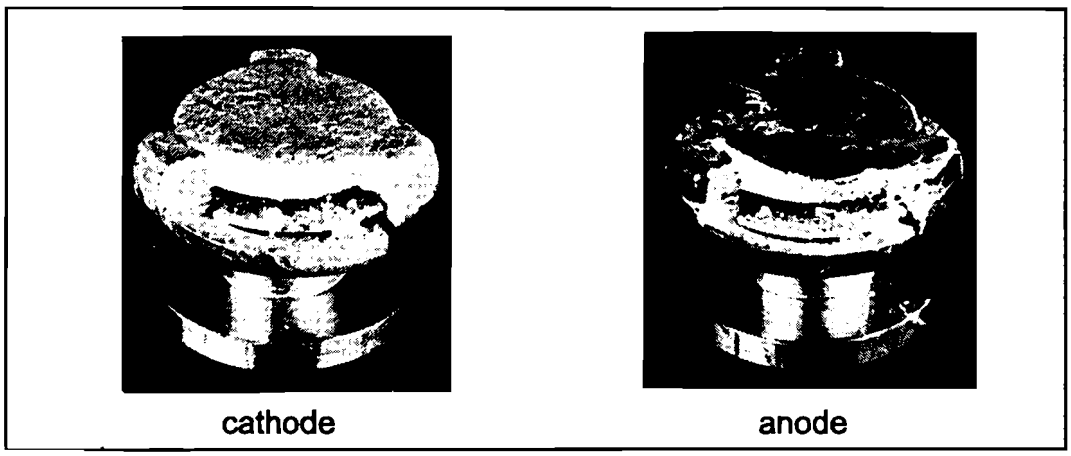

Figure 4-5: The Cu AMF contacts after the interruption measurements.

As can be seen in Figure 4-5, the anode is severely damaged. The severe melting of the anode caused a hole with a diameter around 1 mm in the middle of the contact. Furthermore the shield of the sectional vacuum tube, in the direction of the gravitation force, was covered with large dollops of melted copper.

The severe erosion of the cathode and the anode also caused the metal plate, denoted as "E" in Figure 4-4, to be stuck to the contact by molten copper.

4.2.2 CuCr AMF contacts

Although these contacts are badly damaged after the interruption measurements, the erosion rate of the contacts is rather low. The erosion rate of the cathode is 102.5 μg/C and the erosion rate of the anode is 52.6 μg/C. Figure 4-6 shows the contacts after interruption measurements with a total charge of 6192 C and a maximum arc current of 39.14 kA.

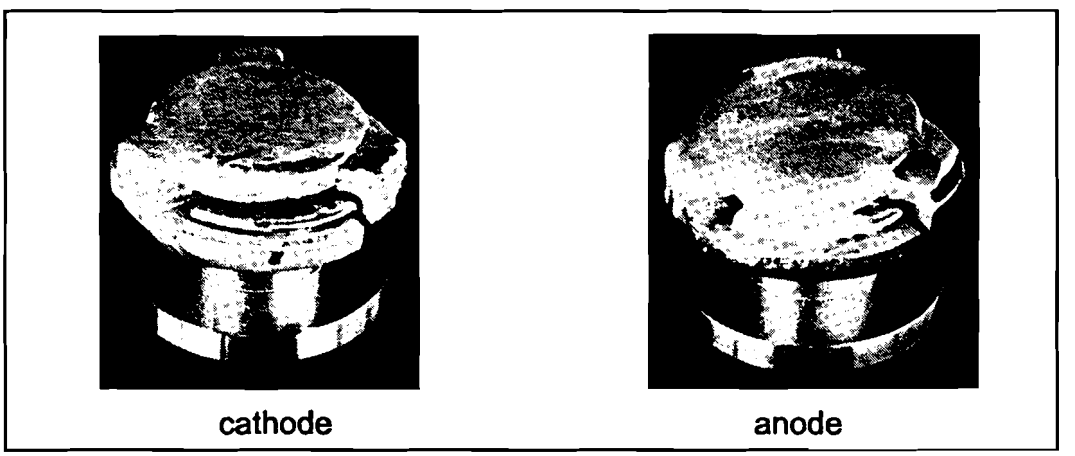

Figure 4-6: The CuCr AMF contacts after the interruption measurements.

The cathode surface not only shows the usual pattern of little craters but also shows some gross melting at one side of the contact. The whole anode surface is one large melted area. The melting of the anode was severe enough to cause a shortcut of one coil arm by the melted contact material.

The light eroded parts of the contacts show a silver alike color and the heavily eroded parts show a copper alike color. Because the contact material is only a 3 mm thick layer on a copper construction, the copper underneath the contact material probably has melted and mixed with the copper-chromium. It seems that the chromium now is drawn into the inter electrode region more easily and the relative copper content of the anode surface increases, resulting in the copper alike color of the heavily eroded parts of the contacts.

The severe erosion of the cathode and anode again caused the metal plates, denoted as "E" in Figure 4-4, to be stuck to the contact.

4.2.3 CuW AMF contacts

The copper-tungsten contacts were only lightly eroded by the interruption measurements. Figure 4-7 shows photographs of the contacts after interruption measurements with a total charge of 4688 C and a maximum arc current of 29.24 kA.

The erosion rate of the cathode contact was 66.3 μg/C and the erosion rate of the anode contact was -41.5 μg/C. The anode actually gained weight, probably due to the fact that a droplet molten material has landed on the surface.

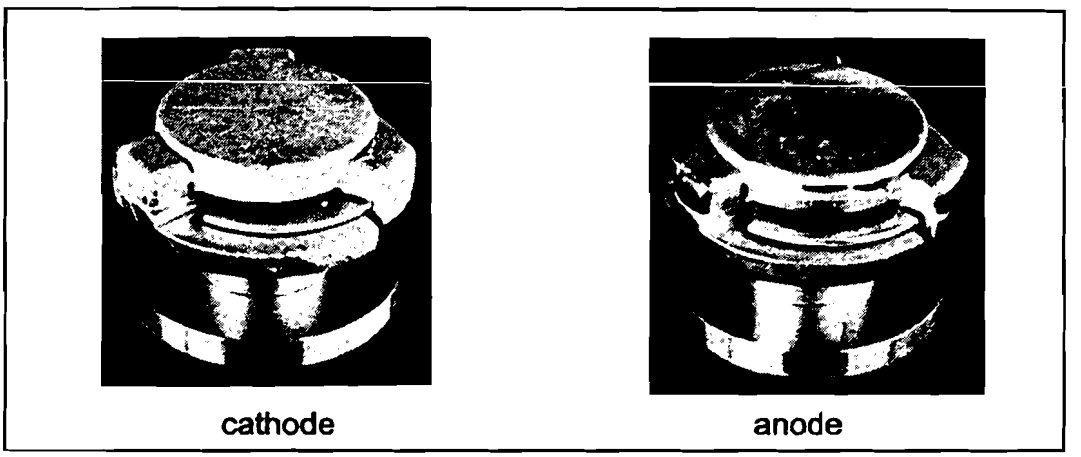

Figure 4-7: The CuW AMF contacts after the interruption measurements.

Closer observation of the anode contact shows three little anode spots. The material in these anode spots holes is made up of a large number of little round droplets, indicating localized molten material. These little round droplets were not visible in the craters on the cathode surface. The cathode craters therefore are formed by different process as are the little anode spots and the two may not be compared to each other without great care in interpretation.

The metal plate, denoted as "E" in Figure 4-4, of the anode was stuck to the contact but the plate of the cathode was not stuck.

Although the copper-tungsten contacts have a very low erosion rate and a rather good interruption performance, the material is not suited for interrupting high currents without some precautions in regard with the screen of the vacuum tube.

During the interruption measurements often zero dips followed by oscillations up to 40 kV occurred in the recovery voltage. Figure 4-9 shows an example of such an oscillation. These very high voltage oscillations not only stress the vacuum circuit breaker but are also dangerous with respect to the equipment connected by the vacuum circuit breaker.

Most reignitions occurred during or just after the oscillations. These reignitions however were not recorded by the camera and therefore were probably along the screen of the sectional vacuum tube. Measurements of the floating screen potential confirmed this assumption and visual inspection of the screen of the sectional vacuum tube also showed that reignitions along the screen had occurred.

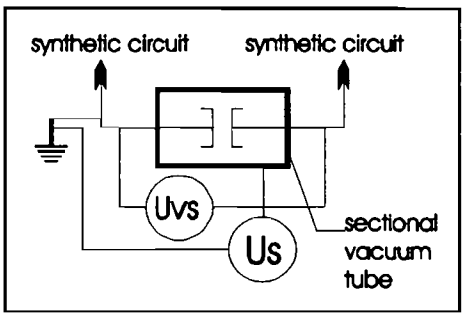

Figure 4-8: The screen potential measurement circuit.

Figure 4-8 shows the measurement setup to determine the screen voltage. If an arc is present in the vacuum tube, the screen voltage will be around zero because neither the cathode nor the anode has a high potential with respect to ground. As the arc extinguishes, the screen voltage will be between the anode and cathode potential because of the capacitive coupling between the screen and the contacts. Figure 4-9 gives an example of a screen measurement during a reignition along the screen.

During the measurement of Figure 4-9 no reignitions were observed with the camera but Figure 4-10 shows a rare recording of a reignition along the screen of the sectional vacuum tube.

Many large droplets of molten metal were visible on the screen of the vacuum tube in the direction of the gravitation force. These large molten droplets probably caused the reignitions along the screen. The boiling temperature of copper is lower than the melting temperature of tungsten, as can be seen in Table 4-3. Reignitions because of copper vapor from the molten droplets copper-tungsten on the screen, are therefore not impossible.

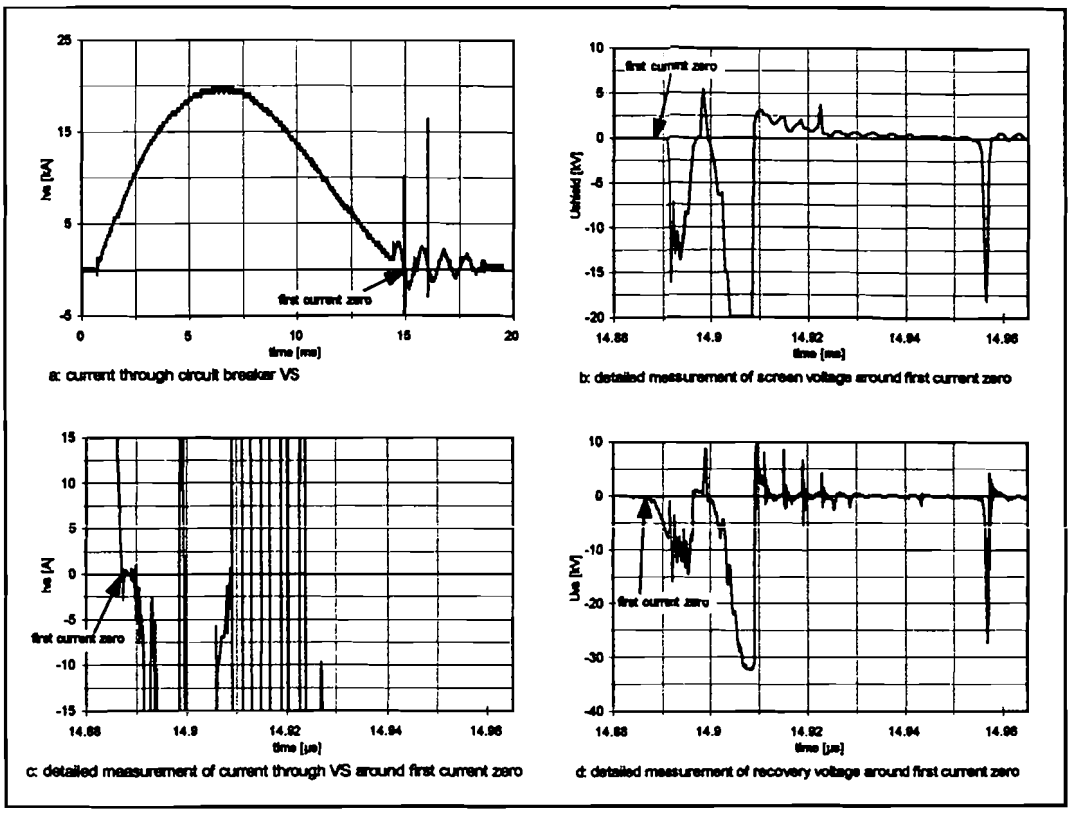

Figure 4-9: Screen voltage measurement with reignition along the screen of the vacuum tube.

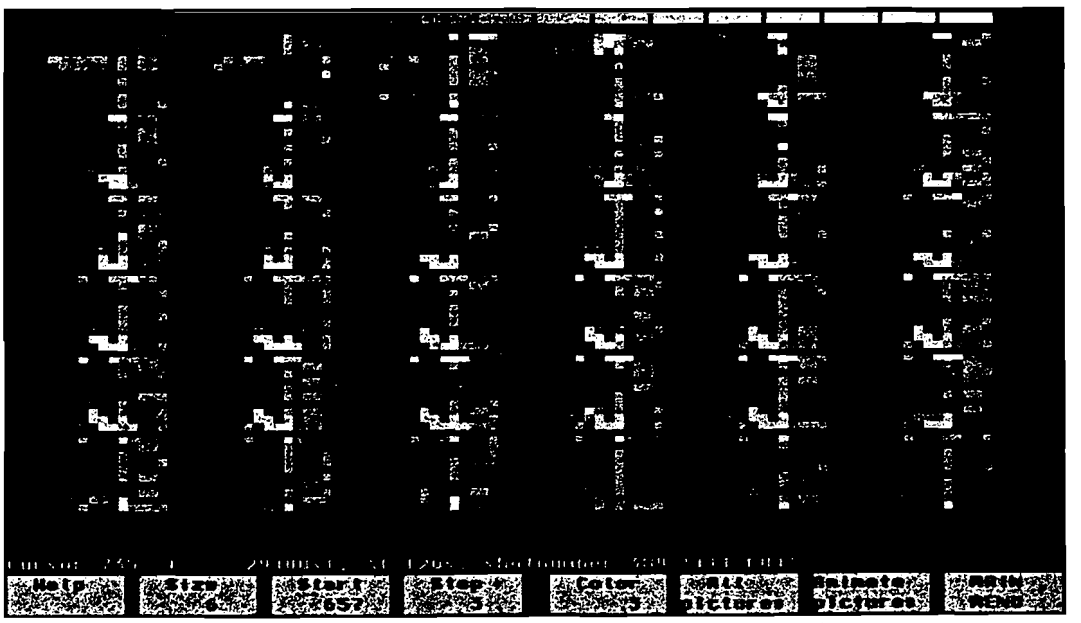

Figure 4-10: A recording of a reignition along the screen of the vacuum tube.

Using copper-tungsten as a contact material, great care has to be taken with respect to possible molten droplets of contact material on the screen of the vacuum tube.

4.2.4 AgWC AMF contacts

The silver-tungsten-carbide contacts have, like the copper-tungsten contacts, a low erosion rate. The erosion rate of the cathode is 21.9 μg/C and the erosion rate of the anode is 19.6 μg/C.

A low erosion rate however does not mean a good interruption performance. The measurement results presented in appendix C show that the AgWC AMF contacts have the worst electrical interruption performance. The AgWC AMF contacts have a low average reignition field strength and have the highest average number of reignitions.

Especially the high average number of reignitions makes the AgWC less suitable for interrupting high currents. In the interruption tests with the synthetic circuit, a reignition has no serious consequences because only a limited amount of electrical energy is present in the injection circuit. In electricity grids however, a continuous supply of electrical energy is present. A reignition in a vacuum circuit breaker in these grids means a new arc will be present until the next current zero crossing. The amount of extra energy absorbed by the contacts during this half period of short circuit current makes an interruption at the next current zero even more unlikely. Because of the reignitions the contacts become more and more heated and a serious failure of the circuit breaker is not unlikely at all.

Figure 4-11 shows the AgWC AMF contacts after interruption measurements with a total charge of 3514 C and a maximum arc current of 33.02 kA.

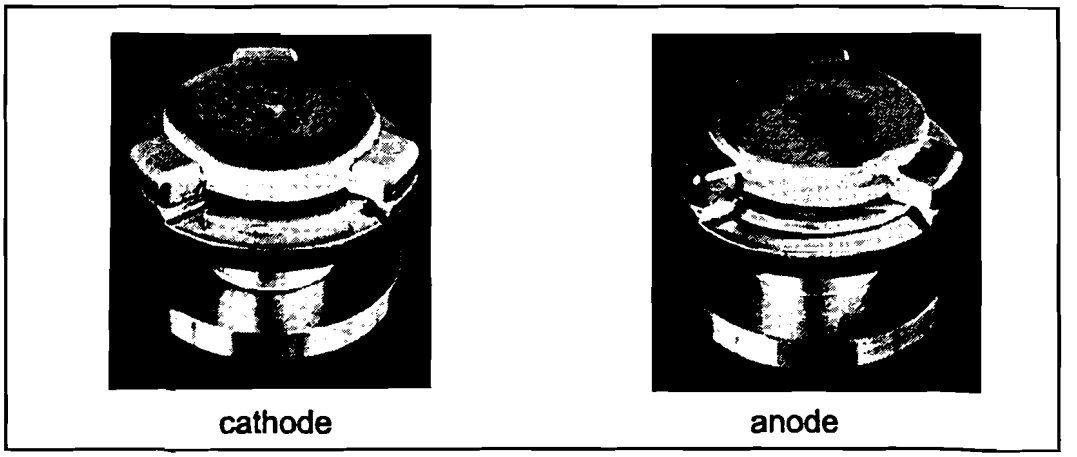

Figure 4-11: The AgWC AMF contacts after the interruption measurements.

As can be seen in Figure 4-11, the contacts have not eroded severely. Both the anode and the cathode however show some little deep craters, possibly indicating the presence of an intense arc. Both the contact surfaces also show cracks, indicating high thermal stresses in the contact material. The metal plate, denoted as "E" in Figure 4-4, was stuck on both the cathode and the anode.

The screen of the vacuum tube also contained some droplets molten metal in the direction of the gravitation force however not so many and such large ones as in the case of CuW. A few reignitions along the screen had occurred, but not so many as in the case of the CuW contacts.

One however should keep in mind that AgWC contacts are designed as "low surge" contacts. These "low surge" contacts prevent the occurrence of high transient recovery voltages under standard operation conditions.

4.3 Comparison of the interruption performance

This paragraph will start by presenting some selected measurement results from appendix C. Afterwards a discussion of the differences in performance will be presented in paragraph 4.3.1 and paragraph 4.3.2. Paragraph 4.3.3 finally gives a ranking of the interruption performance of the used contacts.

The measurement results are divided into three contact gap areas. The division into these three contact gap areas has been made because each area has it's own reignition characteristics. In the contact gap area $0 < d < 3$ mm, dielectric reignition, with the roughness of the surface as a main parameter, is the most important reignition type. For contact gaps in the area $d > 8$ mm, reignition because of plasma production, by the very hot contacts, after current zero is the most important reignition type. Contact gap area $3 < d < 8$ mm gives the best interruption performance because the gap is large enough to eliminate the effects of the electric field strengthening caused by the roughness of the contact surface and the arcing times are small enough to limit the heating of the contacts.

Table 4-1: Erosion rates measured by Binnendijk [Bin95].

Contact type		Cu butt-type	CuCr butt-type	AgWC butt-type
erosion rate	anode [µg/C]	850.3	3.6	25.3
	cathode [µg/C]	172.6	160.2	7.0
total arc charge [C]		1310	1999	2131
maximum arc current [kA]		18.5	28.3	26.9

Table 4-2: Erosion rates of the contacts used in this investigation.

contact type		CuCr butt-type	Cu coil-type	CuCr coil-type	CuW coil-type	AgWC coil-type
erosion rate	anode [µg/C]	52.6	1276	52.6	-41.4	19.6
	cathode [µg/C]	159.6	185.0	102.5	66.3	21.9
total arc charge [C]		3316	3324	6192	4688	3514
maximum arc current [kA]		36.46	26.69	39.14	29.24	33.02

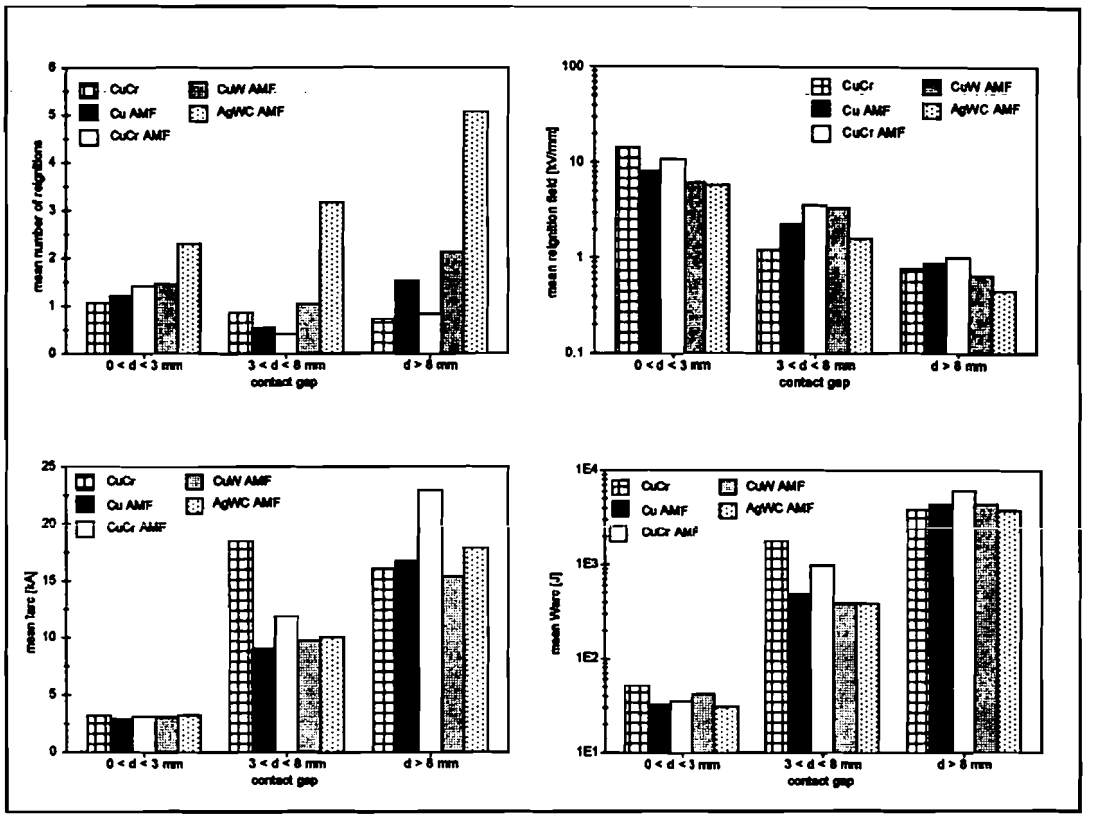

Figure 4-12: Some mean results of the interruption measurements.

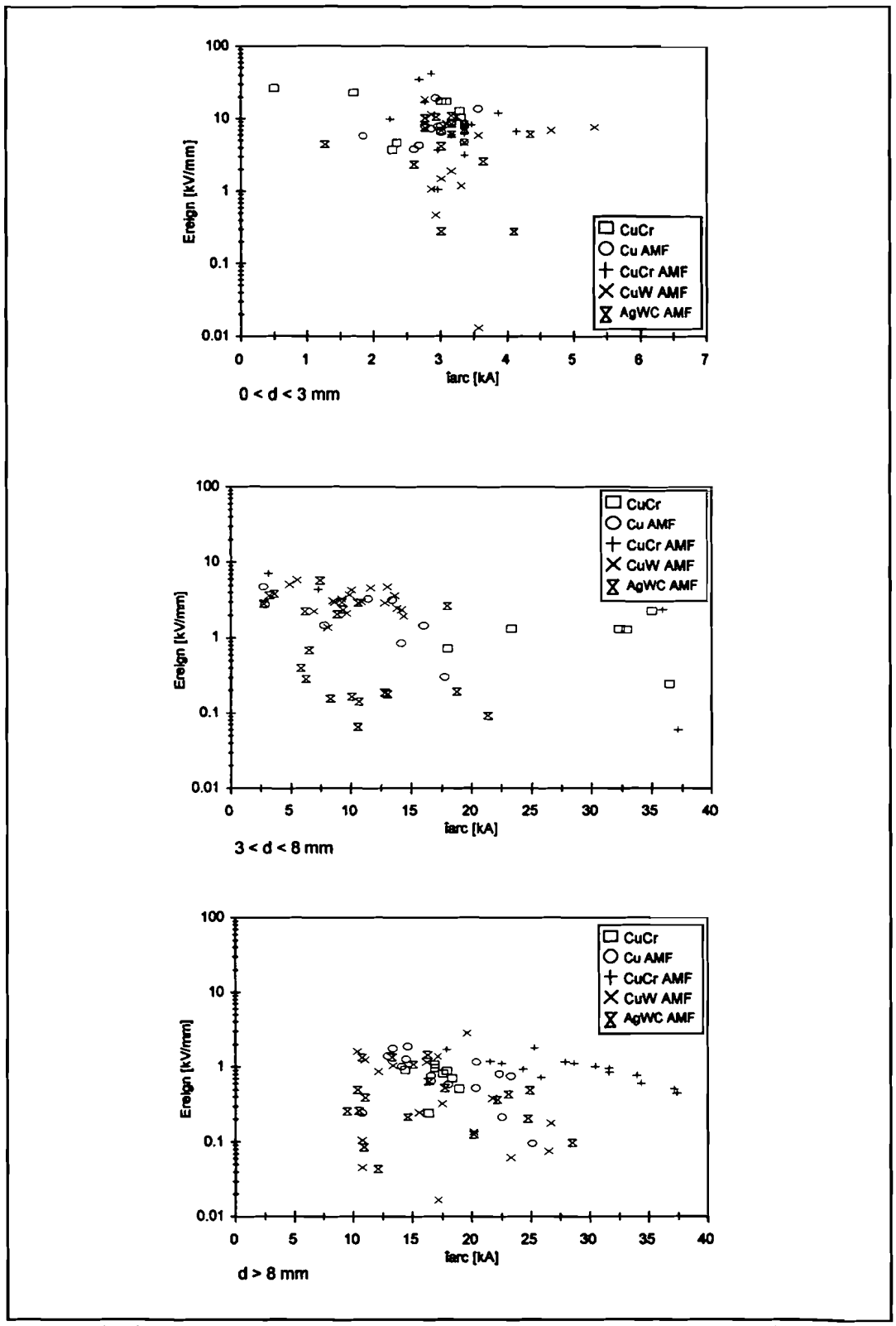

Figure 4-13: Correlation between maximum arc current and reignition field strength.

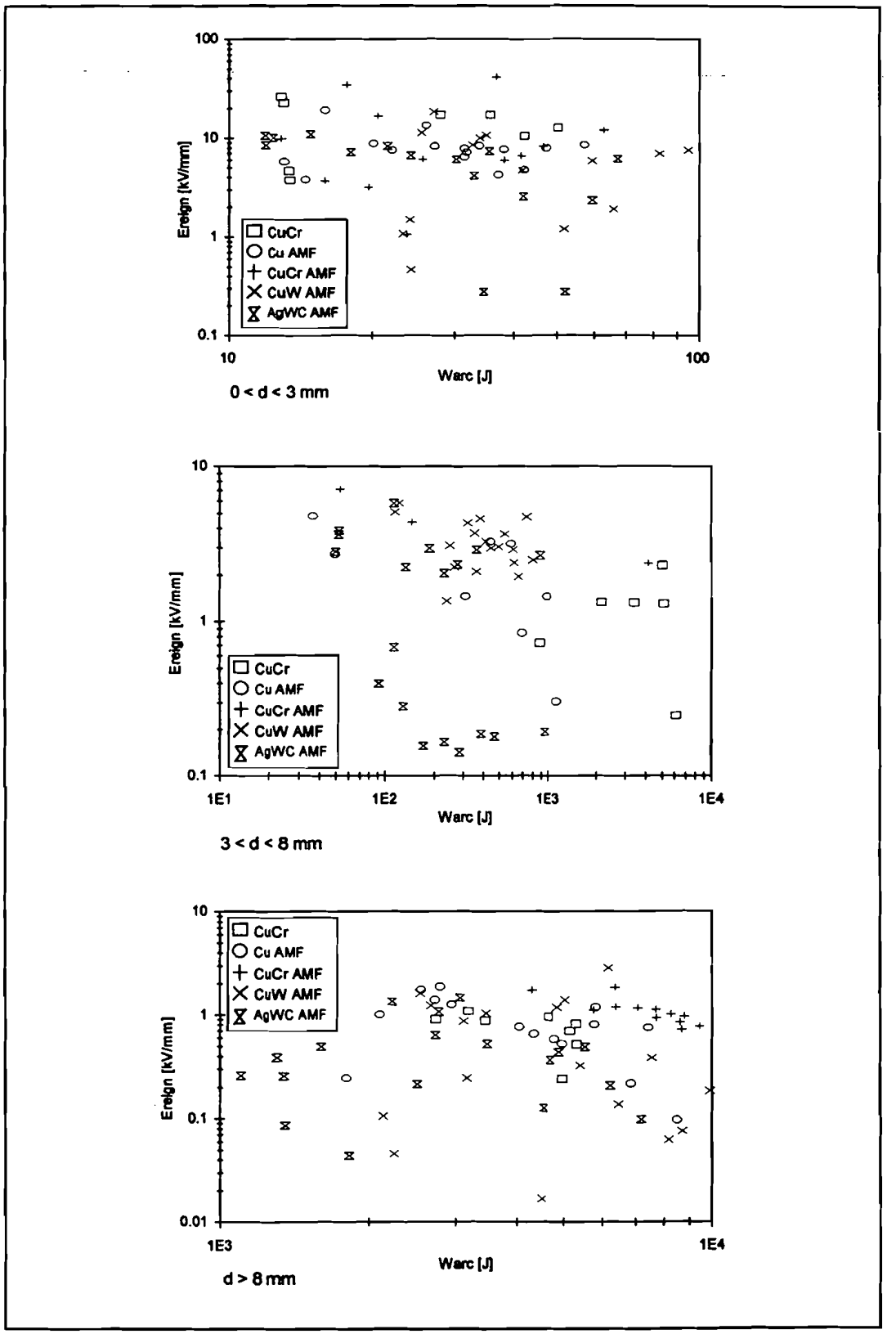

Figure 4-14: Correlation between arc energy and reignition field strength.

4.3.1 Performance of the CuCr contacts with and without axial magnetic field

As mentioned before, some unexplained differences exists between the interruption measurements of Binnendijk [Bin95] and the interruption measurements of this work. To eliminate the unexplained differences, this paragraph will only compare the interruption performance of the CuCr contacts with and without AMF used in this investigation.

As can be seen in Table 4-2, the erosion rate of the anode of the contacts with and without AMF is the same. The erosion rate of the cathode however is slightly less for the AMF contact. The difference in the erosion rate of the cathode contacts however is probably just a coincidence because the axial magnetic field does not significantly change the characteristics of the cathode spots and the cathode spots erode the cathode contact.

The fact that the erosion rate of the anode contacts is the same is rather surprising because one expects a lower erosion rate for the AMF anode contact. The lower erosion rate for the AMF anode contact is expected because of the fact that an axial magnetic field delays or prevents the formation of an anode spot. Five times however, the AMF contacts have interrupted currents with an amplitude between 37 kA and 39.2 kA and arcing times around 11 ms. Visible inspection of the contacts showed that these extreme interruptions eroded the surface much more than did all the other interruption measurements. The non-AMF contacts have not interrupted these extreme currents and therefore these extreme currents may be the cause of the unexpected high erosion rate of the AMF anode contact.

Looking at Figure 4-12 to Figure 4-14 it can be concluded that the AMF contacts only give a better interruption performance for currents above 20 kA and with long arcing time. The long arcing time here is correlated to a large contact gap ($d > 8$ mm) at current zero.

For the contact gaps $0 < d < 3$ mm, there is no difference in interruption behavior between the contacts with and without axial magnetic field. The arc currents and the absorbed energies here are too low to obtain a significant effect of the axial magnetic field. The interruption performance therefore is based mainly on the contact material and contact roughness.

For the contact gaps $3 < d < 8$ mm, there were almost no reignitions in the case of the AMF contacts but there were a number of reignitions for the higher currents in the case of the non-AMF contacts (Figure 4-12). The few reignitions that occurred in the case of the AMF contacts however have a higher reignition field strength than have the reignitions in the case of the non-AMF contacts (Figure 4-12). For these currents and contact gaps the axial magnetic field significantly improves the interruption performance.

For the contact gaps d > 8 mm, the AMF contacts again show a superior interruption performance compared to the contacts without AMF.

Now it may be concluded that the AMF contacts have a better interruption performance than have the non-AMF contacts. The superior interruption performance of the AMF contacts is mainly due to the fact that the arc is less contracted.

A more concentrated arc in the case of the non-AMF contacts might be an explanation for the higher plasma resistance per meter gap length (ρ_p) of the CuCr butt type contacts compared to the ρ_p of the CuCr AMF contacts (Table 3-1, paragraph 3.2).

Besides the interruption performance there also is a significant difference in arc voltage between the AMF contacts and the non-AMF contacts. It is surprising that both the non-AMF contacts and the AMF contacts suffered from anode spots (Figure 4-3 and Figure 4-6) but only the non-AMF contacts had high frequency oscillations on the arc voltage. A closer look at the anode spots on the contacts also reveals some differences in the anode spots. On the non-AMF anode contact (Figure 4-3) a number of anode spots that melted only a part of the contact surface can be seen while the anode spot on the AMF anode contact (Figure 4-6) covers the whole contact surface.

The observations above give rise to the idea that anode spots can be formed by two kinds of mechanisms:

- Due to strong contraction of the arc the axial current density reaches the saturation current density;
- The anode contact is overheated by the absorbed arc energy without strong contraction of the arc.

The first mechanism probably occurs on the non-AMF contacts and the second mechanism probably causes the anode spots on the AMF contacts.

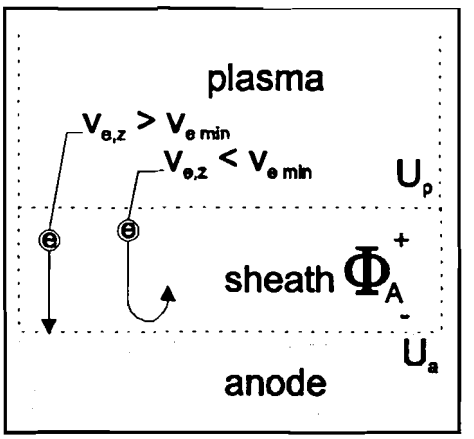

Figure 4-15: sketch of the anode sheath.

The first mechanism is caused by the fact that a space charge region in front of the anode contact is necessary to maintain current continuity [Box83]. Across the sheath a potential drop Φ_A (= U_p - U_a, Figure 4-15) develops in order to regulate the axial current density. Normally this potential drop Φ_A is assumed to be positive so the electrons experience an electric force that is directed from the anode towards the plasma. The electrons have a truncated Maxwell-Boltzman velocity distribution [Box83], so an increase in the positive potential drop Φ_A causes a decrease in the number of electrons reaching the anode and therefore causes a lower axial current density. In chapter 5.1.2 more information is given on the sheath in front of the anode.

A potential drop Φ_A of 0 V implies that all the electrons, with velocity $v_{e,z} > 0$, present in the plasma cross the sheath and reach the anode. The axial current density belonging to this potential drop of 0 V is called the saturation current density. This saturation current density is for copper-chromium in the order of 10^8 A/m^2 [Box83][Sch83]. The relation between the current density and the sheath potential Φ_A is given by formula (4-1) (chapter 5.1.2):

$$J_z = \frac{2 v_{T_{e,z}} F i \exp\left(-\frac{e\Phi_A}{k T_e}\right)}{\pi R^2 v_i \left[1 + \mathrm{erf}\left(\sqrt{\frac{e\Phi_A}{k T_e}}\right)\right]} - \frac{Fi}{\pi R^2} \qquad \textbf{(4-1)}$$

J_z	= current density in axial direction	[A/m^2]
$v_{Te,z}$	= thermal electron velocity in axial direction	[m/s]
F	= ratio of ion current and circuit current	
Φ_A	= anode sheath potential drop	[V]
k	= Boltzman's constant	[J/K]
T_e	= thermal electron energy	[J]
R	= radius of contact	[m]

When the arc becomes contracted and the circuit currents becomes high, the required axial current density may become higher than the saturation current density of a diffuse arc. This of course is not possible so the plasma parameters have to change in order to reach a higher saturation current density. One way of doing that is by increasing the thermal energy of the electrons and at the same time decreasing the number of ions reaching the anode.

The thermal energy of the electrons can be increased and at the same time the number of ions reaching the anode can be decreased by allowing the potential drop Φ_A to become negative. A negative anode sheath potential drop Φ_A will draw the electrons from the plasma into the sheath and thereby increase their speed. This situation however violates the quasi-neutrality of the plasma so drawing the electrons from the plasma actually is a movement of the sheath-plasma edge towards the cathode. The movement of this sheath-plasma edge perhaps can be described by the continuous transition model of Andrews and Varey [And71]. The movement of the sheath edge will be very fast and therefore will cause a sharp rise of the arc voltage. The increased electric field between the contacts increases the energy of the electrons, decreases the speed of the ions towards the anode and increases the field emission of electrons from the cathode. Now the saturation current density will be higher and the sheath-plasma edge could move back to the anode due to overshoot effects. The movement of the sheath-plasma edge towards the anode lowers the arc voltage and the electric field between the contacts so the process can repeat itself.

The movement of the sheath-plasma edge might be an explanation for the high frequency oscillations in the arc voltages of the contacts without axial magnetic field. The increased energy of the accelerated electrons might cause a strong heating of a small part of the contact surface (contracted arc) and an anode spot may be formed.

During the formation of an anode spot by the second mechanism, the saturation current density is not exceeded but the absorbed arc energy becomes so high that large parts of the contact surface become overheated and start to melt [Wat96-2]. In this case the thickness of the contact material layer is important because the rest of the contact is made of copper that has a rather low melting temperature (Table 4-3) and may start melting before all the contact material has melted. This way the contact material may be washed down the contact as can be seen on the anode contact of Figure 4-6.

The formation of an anode spot by the second mechanism does not have to be accompanied by a contraction of the arc. The hot anode contact however will emit a significant amount of metal vapor [Wat96-2]. This metal vapor can change the parameters of the plasma and thereby create the conditions for contraction of the arc. Figure 3-8d gives an example of contraction of the arc due to strong evaporation of the anode contact material.

4.3.2 Performance of the contact materials

This paragraph compares the interruption performance of the different axial magnetic field contacts. Table 4-3 gives some thermal characteristics of the different materials that are used to compose the contact materials.

Table 4-3: Thermal characteristics of the materials used to compose the used contact materials [CRC82][BIN86].

Electrode material	T_m [K]	T_v [K]	λ [$Wm^{-1}K^{-1}$]	$\kappa \cdot c_s$ [$Jm^{-3}K^{-1}$]
Cu	1356	2840	483	$3.47 \cdot 10^6$
Cr	2130	2945	158	$3.24 \cdot 10^6$
W	3683	5933	235	$2.61 \cdot 10^6$
C	3823	5100	160	$1.58 \cdot 10^6$
Ag	1234	2485	450	$2.52 \cdot 10^6$

Comparing Table 4-2 to Table 4-3 a strong correlation between erosion rates, melting temperatures and boiling temperatures can be made. The materials with a high melting and boiling temperature like tungsten and carbide have the lowest erosion rates. Also a high heat conduction coefficient λ and a high $\kappa \cdot c_s$ factor are important for a low erosion rate. Based on the erosion rates the following ranking of contact materials for the interruption of high currents can be made (beginning with the worst): Cu, CuCr, CuW, AgWC.

The erosion rate however is not the only criterion used to judge the interruption performance. The electrical characteristics of the contacts also play an important role in judging the interruption performance.

Figure 4-12 clearly shows that AgWC has the worst electrical performance for the interruption of high currents. Not only has AgWC the lowest mean electric reignition field strength but AgWC also has the highest mean number of reignitions. It has already been mentioned before that a reignition in an electricity grid means that the contacts at least have to absorb another half period of short circuit arc energy. This absorbed arc energy is larger than the absorbed arc energy at the first reignition. It is therefore doubtful whether the interruption will be successful at the next current zero crossing. AgWC however seems to be a very suitable material for "low surge" breakers.

The electrical performance of the Cu and the CuW contacts do not differ so much and is better than the performance of the AgWC contacts. Both the Cu and the CuW however have a significant disadvantage. For the Cu contacts the very high erosion rate (Table 4-2) is the main problem and for the CuW contacts the hot droplets of evaporating contact material on the screen of the vacuum tube (chapter 4.2.3) is the main problem.

The CuCr contacts have superior electrical characteristics, for the interruption of high currents, compared to the other contact materials (Figure 4-12). No significant disadvantages for the CuCr contact material have been noticed so from the used contact materials CuCr can be used best for interrupting high currents.

Figure 4-12 and the discussion above give rise to the idea that the constant ionization voltage U_0 in Table 3-1 (paragraph 3.2) is an indication of the electrical performance of the contact material. The higher the ionization voltage U_0 the better the electrical characteristics of the material. The ionization voltage U_0, however, only is a very rough indication.

4.3.3 Ranking of the performance of the used contacts

Based on the comparisons above, the following ranking of the contacts for the interruption of high currents can be made.

The worst two contacts are the Cu AMF and the AgWC AMF contacts. The Cu AMF contacts have the very high erosion rate as main disadvantage and the AgWC AMF contacts have the low electric reignition field strength as main disadvantage. Which of the two contacts has the worst interruption performance depends on the short circuit situation of the electricity grid they are used in.

Up to about 20 kA the CuCr butt type contacts have a better interruption performance than have the Cu AMF and AgWC AMF contacts. Above 20 kA the effect of the axial magnetic field of the AMF contacts improves the interruption performance of the AMF contacts compared to the CuCr butt type contacts.

The CuW AMF contacts have a little bit better interruption performance for the interruption of high currents than have the CuCr butt type contacts. The interruption performance of the CuW AMF contacts becomes better compared to the CuCr butt type contacts for arc energies higher than ± 1 kJ. In the case that measures are taken to avoid the hot droplets CuW on the screen of the vacuum tube (paragraph 4.2.3), the interruption performance of the CuW AMF contacts probably improves significantly.

The CuCr AMF contacts have the best interruption performance, for interrupting high currents, of all the contacts used in this investigation.

5. Current contraction model

This chapter describes a model for the calculation of the current density in a vacuum arc. The model is part of a larger two dimensional anode spot model that can be used to calculate the temperature of the anode contact. The full-fledged anode spot model could not be realized totally because of a lack of time and lack of experience with finite element method (FEM) programs.

One of the main problems of interrupting high currents with a vacuum circuit breaker is the formation of the so called anode spots. Theories available for the formation of these anode spots can be divided into three groups (chapter 2.1.1, [Mil85]):

- Column Controlled Theories;
- Anode Controlled Theories;
- Anode-Column Interaction Theories.

All these theories state that an anode spot is formed by a contraction of the arc and strong heating of the anode contact. The way the arc is contracted and the anode is heated is different in the different groups of theories.

In the anode spot model described in this paragraph, the anode contact is heated by absorbing the arc energy. In the model used here, the arc energy is directly correlated to the current density. The distribution of the current density therefore determines the distribution of the arc energy on the contact surface. The arc energy is absorbed by the contact and by heat conduction inside the contact material the contact is heated.

The anode spot model belongs to the group of column controlled theories because the contraction of the arc precedes the formation of an anode spot. The assumption that the absorbed arc energy is distributed by means of heat conduction only, is an appropriate first order assumption [Box83][Gol87][Bin95].

When parts of the contact surface reach the boiling temperature of the contact material, metal vapor will be emitted [Wat96-2]. This metal vapor of course will influence the contraction of the arc. This secondary effect however is not implemented in the contraction model yet and is a recommendation for further investigation.

The anode spot model is a two dimensional model that has a cylindrical geometry with reference directions as stated in Figure 5-1.

The model can be divided into two main parts. The first part calculates the contraction of the current in the plasma and the second part calculates the heat flow in the anode contact. As already mentioned this chapter only describes the current contraction part of the model. The heat-transfer part of the model is subject of further investigations.

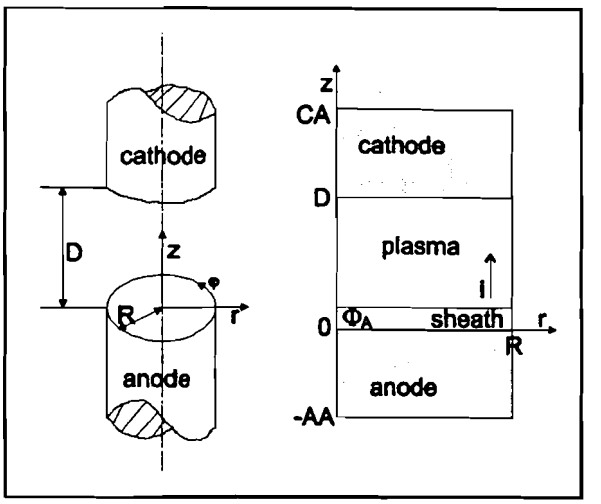

Figure 5-1:The model geometry.

5.1 Contraction model

The model of the current contraction is based on the work of Izraeli [Izr85], Boxman and Goldsmith [Box83].

In this model the arc plasma is modeled as a conducting fluid that flows in a tube with the same diameter as the contacts and with frictionless walls. The following assumptions are made:

- The model geometry is circle cylindric
- There is no mass constriction in the plasma
- The plasma is quasi-neutral
- The electron density is constant
- The plasma velocity is constant and directed from the cathode to the anode.
- The plasma conductivity is constant
- The anode is a perfectly absorbing surface

For calculation of the current constriction in the plasma the quasi-static magnetic field system approximation form of Maxwell's equations is used. This approximation can be used because the magnetic field diffusion time constant in the arc plasma is in the order of 10 ns [Izr85] which is much smaller than the time constant of the power frequency currents used in the experiments of this work.

The assumptions above result in the following form of Maxwell's equations:

$$\nabla \times \mathbf{E} = 0 \tag{5-1}$$

$$\nabla \times \mathbf{B} = \mu_0 \mathbf{J} \tag{5-2}$$

$$\nabla \bullet \mathbf{B} = 0 \tag{5-3}$$

∇	= gradient operator	
E	= electric field vector	[V/m]
B	= magnetic field vector	[T]
μ_0	= permeability of vacuum	[H/m]
J	= current density vector	[A/m^2]

Ohm's law provides the fourth equation:

$$\mathbf{E} = \frac{1}{\sigma}\left(\mathbf{J} + \frac{\sigma}{e n_e}(\mathbf{J} \times \mathbf{B})\right) - (\mathbf{v} \times \mathbf{B}) \tag{5-4}$$

σ	= plasma conductivity	[Ω^{-1}m^{-1}]
v	= plasma velocity vector	[m/s]

Inserting (5-4) and (5-2) into (5-1) gives:

$$\nabla \times \nabla \times \mathbf{B} + \frac{\sigma}{e n_e}\left\{\nabla \times \left[(\nabla \times \mathbf{B}) \times \mathbf{B}\right]\right\} - \mu_0 \sigma \left[\nabla \times (\mathbf{v} \times \mathbf{B})\right] = 0 \tag{5-5}$$

Reformulation of (5-5) gives:

$$\nabla(\nabla \bullet \mathbf{B}) - \Delta \mathbf{B} + \frac{\sigma}{e n_e}\left\{\nabla \times \left[(\nabla \bullet \mathbf{B})\mathbf{B} - \nabla(\mathbf{B} \bullet \mathbf{B})\right]\right\} - \mu_0 \sigma \left[(\nabla \bullet \mathbf{B})\mathbf{v} - (\nabla \bullet \mathbf{v})\mathbf{B}\right] = 0 \tag{5-6}$$

Δ	= Laplace operator

Using (5-3)and the fact that the plasma velocity is assumed to be constant, equation (5-6) reduces to:

$$\Delta \mathbf{B} = 0 \tag{5-7}$$

To solve equation (5-7) one must know the boundary conditions. Because of the cylindrical geometry, cylinder coordinates (r, φ, z) will be used. The magnetic field vector **B** has to be resolved in it's three components. On the edge of the plasma region sufficient boundary conditions exist to solve component B_φ. Components B_r and B_z however do not have sufficient boundary conditions on the edge of the plasma region and therefore have to be solved in the contacts.

5.1.1 The azimuthal magnetic field component

The azimuthal magnetic field component B_φ has the following boundary conditions (Figure 5-2):

Boundary 3: On the cathode a constant current density is assumed. With equation (5-2) the boundary condition for B_φ on the cathode is given by:

$$B_{\varphi_{boundary\,3}}(r) = \frac{\mu_0 i\, r}{2\pi R^2} \quad (5\text{-}8)$$

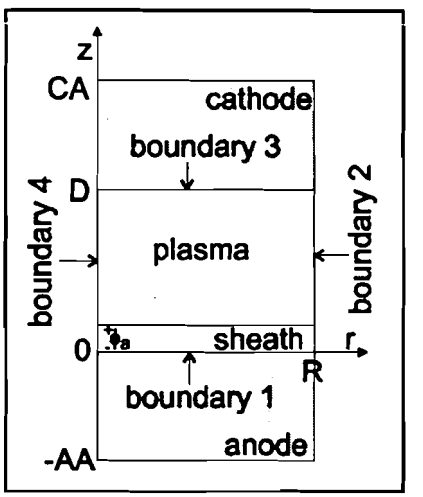

Figure 5-2: The boundaries for the azimuthal magnetic field component.

Boundary 4: This boundary represents the cylinder axis. The azimuthal magnetic field encircles no current here so the following boundary condition is valid:

$$B_{\varphi_{boundary4}} = 0 \quad (5\text{-}9)$$

Boundary 2: This boundary represents the cylinder wall. The azimuthal magnetic field here encircles the total current so boundary condition (5-10) is valid:

$$B_{\varphi_{boundary2}} = \frac{\mu_0 i}{2\pi R} \quad (5\text{-}10)$$

Boundary 1: On the anode the current density is unknown. As a first approximation the anode however can be treated as an equipotential surface. This implies that the radial electric field E_r on the anode is zero. The assumption above gives the following boundary condition for the azimuthal magnetic field:

$$E_{r_{boundary\,1}} = 0 = \frac{1}{\sigma} J_r + \frac{1}{e n_e} (\mathbf{J} \times \mathbf{B})_r - (\mathbf{v} \times \mathbf{B})_r$$
$$= -\frac{1}{\sigma \mu_0} \frac{\partial B_\varphi}{\partial z} - \frac{1}{e n_e \mu_0} \frac{\partial B_\varphi^2}{\partial r} + v_z B_\varphi \qquad \textbf{(5-11)}$$

A few remarks however have to be made applying condition (5-11):

- In equation (5-11) B_r and B_z are assumed to be zero. This is only a correct assumption if the contacts used in the vacuum circuit breaker do not generate an axial or transversal magnetic field. The axial and radial magnetic field components change the boundary condition for the azimuthal magnetic field on the anode. In paragraph 5.1.3 the boundary condition for boundary 1 is given if the contacts do generate an axial or transversal magnetic field.

- The anode may be an equipotential surface but Boxman and Goldsmith [Box83] have shown that a space charge layer in front of the anode is necessary to maintain current continuity. Paragraph 5.1.2 treats the boundary condition for azimuthal magnetic field on the anode when the space charge layer is taken into account.

5.1.2 Anode sheath

Boxman and Goldsmith [Box83] have shown that a sheath in front of the anode is necessary in order to maintain current continuity. Calculations of the electron mean free path and the Debye length indicate that the anode sheath may be modeled collisionless [Box83].

Across the sheath a potential drop Φ_A (=U_p - U_a, Figure 5-3) develops in order to regulate the electron density. This potential drop Φ_A is positive in the case the anode potential is lower than the plasma-sheath edge potential. Normally Φ_A is assumed to be positive so the electrons in the sheath experience a repelling electric force directed from the anode to the plasma.

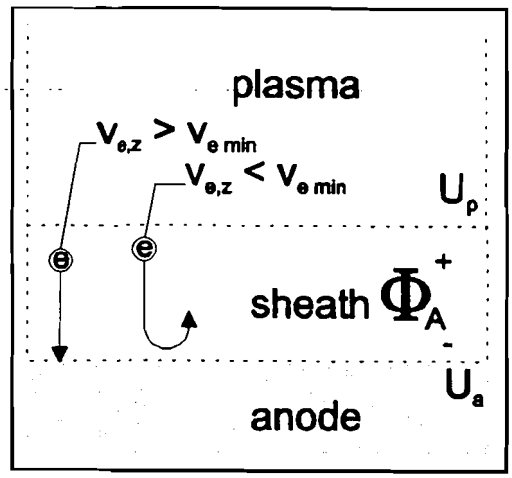

Figure 5-3: The movement of the electrons in the sheath.

In this simple model of the anode region the anode surface is assumed to be perfectly absorbing and the electrons receive their thermal energy in the collision dominated plasma.

With the assumptions mentioned above it is possible to calculate the potential drop Φ_A.

The minimum energy in z-direction required for the electrons to cross the sheath is equal to the electron charge times the potential drop Φ_A. Because the plasma is assumed to be quasi-neutral and collision-dominated, the electrons have thermal energy only on the plasma-sheath edge. The minimum speed in negative z-direction (Figure 5-1) required for the electrons to cross the sheath is now given by:

$$v_{z,min} = \sqrt{\frac{2e\Phi_A}{m_e}} = \sqrt{\frac{k\,T_{e,min}}{2\pi\,m_e}} \qquad (5\text{-}12)$$

m_e = electron mass [kg]
T_e = thermal electron energy [J]

The electron velocity distribution in the sheath is a truncated Maxwell-Boltzman distribution [Box83]:

$$f_e(v_x, v_y, v_z) = n_{es}\sqrt{\frac{m_e}{2\pi\,k\,T_e}}\exp\left[-\left(\frac{m_e}{2\,k\,T_e}\right)\left(v_x^2 + v_y^2 + v_z^2\right)\right] \bullet h\left\langle\sqrt{v_z^2 - \frac{2e\Phi_A}{m_e}}\right\rangle \qquad (5\text{-}13)$$

n_{es} = electron density in the sheath region [1/m^3]
k = Boltzman's constant [J/K]

where h<x> is the Heaviside function:

$$h<x>=\begin{cases}0 & x<0\\ 1 & x>0\end{cases} \tag{5-14}$$

The sheath potential can now be determined by invoking the following matching requirements at the plasma-sheath edge:

1) charge neutrality:

$$\int_{-\infty}^{+\infty}\iint f_e(v)\,dv = n_{es}\frac{1}{\sqrt{2\pi}}\int_{\sqrt{\frac{2e\Phi_A}{kT_e}}}^{\infty}\exp\left(-\frac{\xi^2}{2}\right)d\xi = \frac{FJ}{ev_i} \tag{5-15}$$

ξ = help variable

2) electron current continuity:

$$\int_{-\infty}^{-\sqrt{\frac{2e\Phi_A}{m_e}}}\int_{-\infty}^{+\infty}\iint v_z f_e(v)\,dv = -n_{es}\sqrt{\frac{kT_e}{2\pi m_e}}\exp\left(-\frac{e\Phi_A}{kT_e}\right) = -\frac{(1+F)J_z}{e} \tag{5-16}$$

Taking the ratio of (5-15) and (5-16) and using (5-17), equation (5-18) is found.

$$v_{Te_z} = \sqrt{\frac{kT_e}{2\pi m_e}} \tag{5-17}$$

$$\frac{v_{Te_z}\exp\left(-\frac{e\Phi_A}{kT_e}\right)}{\frac{1}{\sqrt{2\pi}}\int_{\sqrt{\frac{2e\Phi_A}{kT_e}}}^{\infty}\exp\left(-\frac{\xi^2}{2}\right)d\xi} = \frac{v_i(1+F)}{F} \tag{5-18}$$

Using expressions (5-19) and (5-20) [Izr85] equation (5-18) can be written as (5-21). Equation (5-21) finally reveals the relation between the axial current density on the plasma sheath edge and the sheath potential.

$$\frac{v_i(1+F)}{F} = \frac{J_z + FJ_b}{\frac{FJ_b}{v_i}} \tag{5-19}$$

$$J_b = \frac{i}{\pi R^2} \tag{5-20}$$

$$J_z = \frac{2 v_{Te_z} F i \exp\left(-\frac{e \Phi_A}{k T_e}\right)}{\pi R^2 v_i \left[1 + \mathrm{erf}\left(\sqrt{\frac{e \Phi_A}{k T_e}}\right)\right]} - \frac{Fi}{\pi R^2} \tag{5-21}$$

Physically seen the model of the sheath region ends as the sheath potential Φ_A becomes negative. This also implies that there is a saturation current density that represents the maximum current density possible on the anode. This saturation density is given by (5-22).

$$J_{sat} = \frac{2 v_{Te_z} Fi}{\pi R^2 v_i} - \frac{Fi}{\pi R^2} \tag{5-22}$$

J_{sat} = saturation current density [A/m^2]

A sheath potential of 0 V implies that all electrons present in the plasma cross the sheath region with their axial directed velocity. The current density belonging to this sheath potential of 0 V is the saturation current density J_{sat}. If the sheath voltage Φ_A becomes negative, the sheath will start to draw electrons from the plasma. The plasma however is assumed to be quasi-neutral so an increase of electron speed at the plasma-sheath edge will lead to an unstable situation that perhaps can become stable again by the following mechanism.

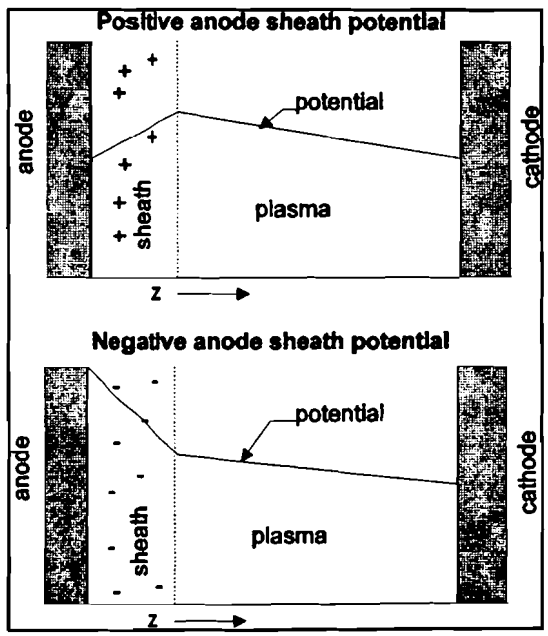

Figure 5-4: Positive and negative sheath potentials.

To reach a stable situation the sheath potential drop Φ_A has to become positive again. This means the saturation current density has to increase. One way of doing that is to increase the thermal energy of the electrons and to decrease the speed of the ions. If the sheath potential drop Φ_A becomes negative, both effects will occur. The plasma however was assumed to be quasi neutral. No violation of this assumption means that the plasma-sheath edge has to move towards the cathode. The movement of the plasma sheath edge in turn has a number of effects:

- The sheath region can no longer be modeled as a collisionless layer because it has become wider than a Debye-length. This implies that there are collisions between accelerated electrons and decelerated ions. These collisions can cause an increase in the ionization rate of the ions, thereby increasing the number of electrons reaching the anode. A second effect of these collisions is the increase in the thermal energy of the electrons.

- As already mentioned a negative sheath potential not only increases the directed electron speed in the space charge layer but also decreases the drift velocity of the ions. Sheath potentials in the order of -40 V even cause ions to change direction and return to the plasma. One effect of this change in the directed ion velocity is a reduction of the negative contribution of the ions to the circuit current (formula (2-1), paragraph 2.1.1). The decrease in speed of the ions also increase the positive charge present in the space charge layer and thereby causes an increase of Φ_A.

- The movement of the plasma-sheath edge creates a higher axial electric field on the cathode that in turn increases the production of electrons from the cathode.

The effects mentioned above can cause an increase in the saturation current density which in turn causes the sheath potential to become positive again. The movement of the plasma-sheath edge towards the cathode and back to the anode will be very fast and will cause high arc voltage oscillations. The movement of the plasma-sheath edge perhaps can be described by the continuous transition model or matrix model [And71]. The movement of the plasma-sheath edge could be an explanation for the noisy high arc voltages measured at the onset of an anode spot.

Wieckert and Egli disagree with the discussion above. In their article [Wie89] they state that the current density can not be higher than the saturation current density. Their saturation current density seems not to be effected by a negative anode sheath potential drop Φ_A.

In their article Wieckert and Egli [Wie89] calculate anode sheath potential drops Φ_A down to -36 V when using their assumptions of "sheath stiffness" G=0.5 and a thermal electron energy of 2 eV. However they also assume directed ion energies of 30 eV which means that the ions do not have enough energy to reach the anode when Φ_A is -36 V. Normally the ratio of ion current to total current (F) is around 0.1 [Sch83]. This means the current density has to increase with 10% when the anode sheath potential drop Φ_A decreases form 0 V to -36 V. Negative sheath potential drops Φ_A therefore do influence the saturation current density.

Implementation of the sheath into the plasma model changes the boundary condition for the azimuthal magnetic field on boundary 1 (formula (5-11), Figure 5-2) into:

$$E_{r_{boundary1}} = -\frac{\partial \Phi_A}{\partial r} = \frac{1}{\sigma} J_r + \frac{1}{e n_e} (\mathbf{J} \times \mathbf{B})_r - (\mathbf{v} \times \mathbf{B})_r$$
$$= -\frac{1}{\sigma \mu_0} \frac{\partial B_\varphi}{\partial z} - \frac{1}{e n_e \mu_0} \frac{\partial B_\varphi^2}{\partial r} + v_z B_\varphi \qquad (5\text{-}23)$$

Boundary condition (5-23) actually has to be applied to the plasma-sheath edge. The space charge sheath however is very thin compared to the contact gap so boundary condition (5-23) may be applied to the anode surface.

5.1.3 The axial and radial magnetic field components

The calculation of the axial and radial magnetic field component is little bit more complicated than the calculation of the azimuthal magnetic field component. The axial and radial magnetic field can not be solved in the plasma region only because there are not sufficient boundary conditions. Deep inside the contact material however it may be assumed that the axial magnetic field, generated by the coil type contact, is constant and it also may be assumed that the radial magnetic field component is zero deep inside the contacts.

Using the assumptions made above, the following boundary conditions can be used (Figure 5-5):

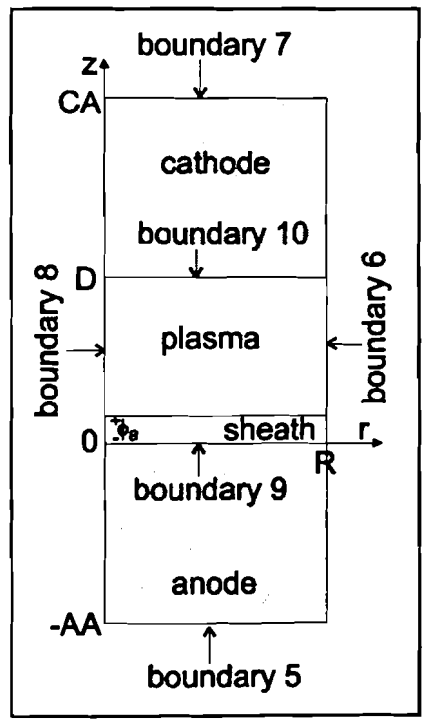

Figure 5-5: Boundaries for the axial and radial magnetic field components.

Boundary 5: Boundary 5 is located deep inside the contact material. Deep inside the contact material the axial magnetic field component is assumed to be constant and the radial magnetic field component is assumed to be zero. The boundary conditions therefore are given by (5-24) and (5-25).

$$B_{r_{boundary5}} = 0 \qquad \textbf{(5-24)}$$

$$B_{z_{boundary5}} = K_{B_z} \qquad \textbf{(5-25)}$$

K_{Bz} = Amplitude of axial magnetic field component deep inside the contact material [T]

Boundary 6: This boundary is the outside of the cylinder formed by the contacts and the plasma. The boundary condition for the axial magnetic field on boundary 6 is not totally clear because of the lack of an axial magnetic field source in the model. From continuity point of view, boundary conditions (5-26) and (5-27) are applied on boundary 6:

$$B_{r_{boundary6}} = 0 \qquad \textbf{(5-26)}$$

$$\left.\frac{\partial B_z}{\partial r}\right|_{boundary6} = 0 \qquad \textbf{(5-27)}$$

Further investigation into the boundary conditions on boundary 6 is advised.

Boundary 7: This boundary also is located deep inside the contact material. Boundary conditions (5-24) and (5-25) therefore can also be applied to boundary 7.

Boundary 8: This boundary is the rotation axis. Because of continuity considerations, boundary conditions (5-26) and (5-27) have to be applied to this boundary.

Boundary 9: No strong boundary conditions can be given for this boundary. The relative magnetic permeability (μ_r) of the used contact materials however is approximately equal to one. The radial (B_r) and axial (B_z) magnetic field components therefore have to be continuous on boundary 9.

The boundary condition for the azimuthal magnetic field component (B_φ) on boundary 9 however changes when a radial (B_r) and an axial (B_z) magnetic field component are present. The boundary condition for the azimuthal magnetic field component is now given by formula (5-28).

$$E_{r_{boundary\,9}} = -\frac{\partial \Phi_A}{\partial r} = \frac{1}{\sigma} J_r + \frac{1}{e\,n_e}(\mathbf{J} \times \mathbf{B})_r - (\mathbf{v} \times \mathbf{B})_r$$
$$= -\frac{1}{\sigma \mu_0}\frac{\partial B_\varphi}{\partial z} - \frac{1}{e\,n_e\,\mu_0}\frac{\partial (B_r + B_\varphi + B_z)^2}{\partial r} + v_z B_\varphi \qquad \textbf{(5-28)}$$

Taking B_r and B_z zero in equation (5-28) gives back equation (5-23).

Boundary 10: The same considerations as for boundary 9 can be made for boundary 10. The radial (B_r) and axial (B_z) magnetic field components therefore also have to be continuous on boundary 10.

5.1.4 Implementation of electric field effects

Until now the model only contained a magnetic field that was responsible for the current contraction. For a better correlation with the physical reality the model, however, also needs some effects of the electric field.

The contraction model is assumed to be rotation symmetric. This means that equation (5-29) is valid.

$$\frac{\partial \mathbf{E}}{\partial \varphi} = 0 \qquad \textbf{(5-29)}$$

The equations for the magnetic field are time independent so according to Maxwell equation (5-30) is valid.

$$\oint \mathbf{E}\,d\mathbf{l} = 0 \qquad \textbf{(5-30)}$$

Combining equations (5-29) and (5-30) reveals that the azimuthal component of the electric field (E_φ) is zero. Using this in equation (5-4), the following condition for the magnetic field is found:

$$\frac{\partial B_r}{\partial z} - \frac{\partial B_z}{\partial r} - \mu_0 \sigma v_z B_r = 0 \qquad \textbf{(5-31)}$$

Equation (5-31) however is not the only result of the electric field that has to be taken into account. Another effect of the electric field that has to be taken into account is caused by the assumption that the plasma has a constant conductivity (paragraph 5.1). A contraction of the current in the plasma therefore means that a potential drop in radial direction, that opposes the contraction of the current, is present. The electric field caused by the potential drop can be calculated by equation (5-32).

$$\frac{\partial}{\partial r}\int_D^\xi E_z \, dz = E_r \qquad \textbf{(5-32)}$$

Equation (5-32) uses the standard directions as stated in Figure 5-1. Eliminating the integral of equation (5-32) gives:

$$\frac{\partial E_z}{\partial r} = \frac{\partial E_r}{\partial z} \qquad \textbf{(5-33)}$$

Using equation (5-4) in equation (5-33), gives the following condition for the magnetic field:

$$\frac{\partial}{\partial r}\left[\frac{1}{r}\frac{\partial\left(rB_\varphi\right)}{\partial r}\right] = -\frac{\partial^2 B_\varphi}{\partial z^2} \qquad \textbf{(5-34)}$$

Using the effects of the electric field mentioned above, the contraction model uses equations (5-35) to (5-37) to calculate the components of the magnetic field. The boundary conditions described in paragraph 5.1.1, paragraph 5.1.2 and paragraph 5.1.3 are used as boundary conditions for equations (5-35) to (5-37).

$$\Delta B_r + \frac{\partial B_r}{\partial z} - \frac{\partial B_z}{\partial r} = \mu_0 \sigma v_z B_r \tag{5-35}$$

$$\Delta B_\varphi + \frac{\partial}{\partial r}\left[\frac{1}{r}\frac{\partial\left(r B_\varphi\right)}{\partial r}\right] = -\frac{\partial^2 B_\varphi}{\partial z^2} \tag{5-36}$$

$$\Delta B_z + \frac{\partial B_r}{\partial z} - \frac{\partial B_z}{\partial r} = \mu_0 \sigma v_z B_r \tag{5-37}$$

5.2 Numerical implementation of the contraction model

The finite element method (FEM) program PDEase2 [SPD95] was used to implement the contraction model described in paragraph 5.1. This program uses a description file in which the problem is described with simple commands. The program uses the description file as input and automatically starts calculating and refining the grid until the selected accuracy is reached. Appendix D gives an example of such a description file.

Although the program is easy to run there are three significant disadvantages:

- The program does not use the computer memory consequently;
- It is almost impossible to influence the calculation process;
- The program does not allow changing geometries.

The last disadvantage becomes important when the program is used to calculate the temperature of the anode contact. The absorbed arc power has to be integrated over the arcing time in order to calculate the temperature of the anode contact. During the arcing time, however, the contact gap changes and therefore the geometry has to change. In order to calculate the anode temperature with PDEase2, a current contraction description file for each time step and a description file for the heat flow calculation is required. These description files can be generated best by writing a little program (in Turbo Pascal for example) that generates all the required description files. The description files of course use the results of the last time step as a start in order to reduce the calculation time.

The process described above requires a lot of computer time and therefore it is recommend to look for a FEM program that is more suited for these calculations.

In order to calculate the current constriction a few plasma parameters have to be known. Literature gives many and also contradicting values for the plasma parameters. In this report the plasma parameters measured by Schellekens [Sch83] are used as an indication for the plasma parameters in the model. The parameters measured by Schellekens were measured using copper electrodes. In this work however only the interruption performance of CuCr has been measured for butt type contacts. The measurements of the CuCr butt-type contacts therefore are compared to the calculations of current contraction in a copper vapor arc when the model contains a butt-type contact configuration.

In order to draw more fundamental conclusions with respect to the contraction model, it is advised to collect the plasma parameters belonging to the used contact materials.

From Schellekens [Sch83] the following required plasma parameters are used:

- Electron density n_e. The electron density depends strongly on the arc current. The measurement results indicate a peak electron density that can be described by:

$$\begin{aligned} n_e &= 5.6\cdot10^{17}\bullet i - 4.5\cdot10^{20} \quad \wedge \quad i < 4\cdot10^{3}A \\ n_e &= 3.3\cdot10^{17}\bullet i + 7.0\cdot10^{20} \quad \wedge \quad i \geq 4\cdot10^{3}A \end{aligned} \tag{5-38}$$

- Ratio F of ion current to total current. F is measured to be around 0.1.

- Plasma velocity v. The mean plasma velocity can be determined by using the ion velocity and the ratio of ion current to total current [Sch83]. Using this method, the mean plasma mass velocity (v_z) is around 500 m/s directed from the cathode towards the anode.

- Thermal electron energy kT_e. The electron temperature is independent of the current but depends on the applied axial magnetic field. The electron temperature seems to be around 2.7 eV.

- Plasma conductivity σ. Schellekens [Sch83] does not give an explicit value or formula for the plasma conductivity. Therefore a theoretical approximation of σ is used.

According to Mitchner and Kruger [Mit73] the plasma conductivity can be calculated by using formula (5-39):

$$\sigma = \frac{n_e e^2}{m_e v_e n_i Q_{ei}} \tag{5-39}$$

v_e = thermal electron velocity in all directions [m/s]
Q_{ei} = electron-ion momentum transfer collision cross section [m^2]

Formula (5-39) however can only be used if local thermal equilibrium (LTE) or partial local thermal equilibrium (PLTE) is assumed.

The average electron-ion momentum transfer collision cross section is given by [Mit73]:

$$\overline{Q}_{ei} = 6\pi \overline{b}_0^2 \ln(\Lambda) \tag{5-40}$$

where

$$\overline{b}_0 = \frac{ze^2}{12\pi\varepsilon_0 k T_{arc}} \tag{5-41}$$

ε_0 = electric permitivity of vacuum [Fm^{-1}]
T_{arc} = arc temperature [K]

and where

$$\Lambda = 12\pi n_e \left(\frac{\varepsilon_0 k T_{arc}}{n_e e^2}\right)^{\frac{3}{2}} \tag{5-42}$$

Combining equations (5-39) to (5-42) yields:

$$\sigma = \frac{24\pi\varepsilon_0^2 (k T_{arc})^{\frac{3}{2}}}{ze^2 (3 m_e)^{\frac{1}{2}} \ln(\Lambda)} \tag{5-43}$$

Schellekens [Sch83] measured an average ion charge number around one and an electron temperature of 2.7 eV. Because no clear indication of T_{arc} is given, T_{arc} is assumed to be equal to the electron temperature. Using these figures in formula (5-43) a plasma conductivity of $5.7 \cdot 10^3\ \Omega^{-1}m^{-1}$ is found for a 10 kA arc.

Implementation of the axial and radial magnetic field components also requires a calculation of the magnetic field inside the contacts. This however leads to still unsolved numerical problems.

PDEase2 does not allow different equations in different regions of the geometry and therefore also tries to solve the plasma equations inside the contacts. To overcome this problem the plasma parameters like plasma velocity, electron thermal energy, etc. were taken zero in the contact region resulting in "divide by zero" errors of the program. Consequently PDEase2 can not be used to calculate the current contraction when an external magnetic field is present.

Due to the numerical problems mentioned above, results of the calculations of the current contraction in a coil-type configuration (implementation of all three magnetic field components) are not yet available. The discussion of the contraction model will therefore be limited to a discussion of the results of the butt-type configuration (only the azimuthal magnetic field component is accounted for).

5.3 Discussion of the contraction model in the case of butt-type contacts

In this paragraph an interruption of a 13 kA current with CuCr butt-type contacts is compared to the calculations of the current contraction model. This comparison however is very limited because the measurement gives no information on the current density. The comparison however reveals some rough characteristics indicating a reasonable performance of the current contraction model.

Figure 5-6 to Figure 5-9 show the measurement results and some of the results of the calculations with the current contraction model. Both the measurement results and the results of the calculation are presented more extensively in appendix E. The markings A to C in Figure 5-6 denote the points that have been used in the calculations.

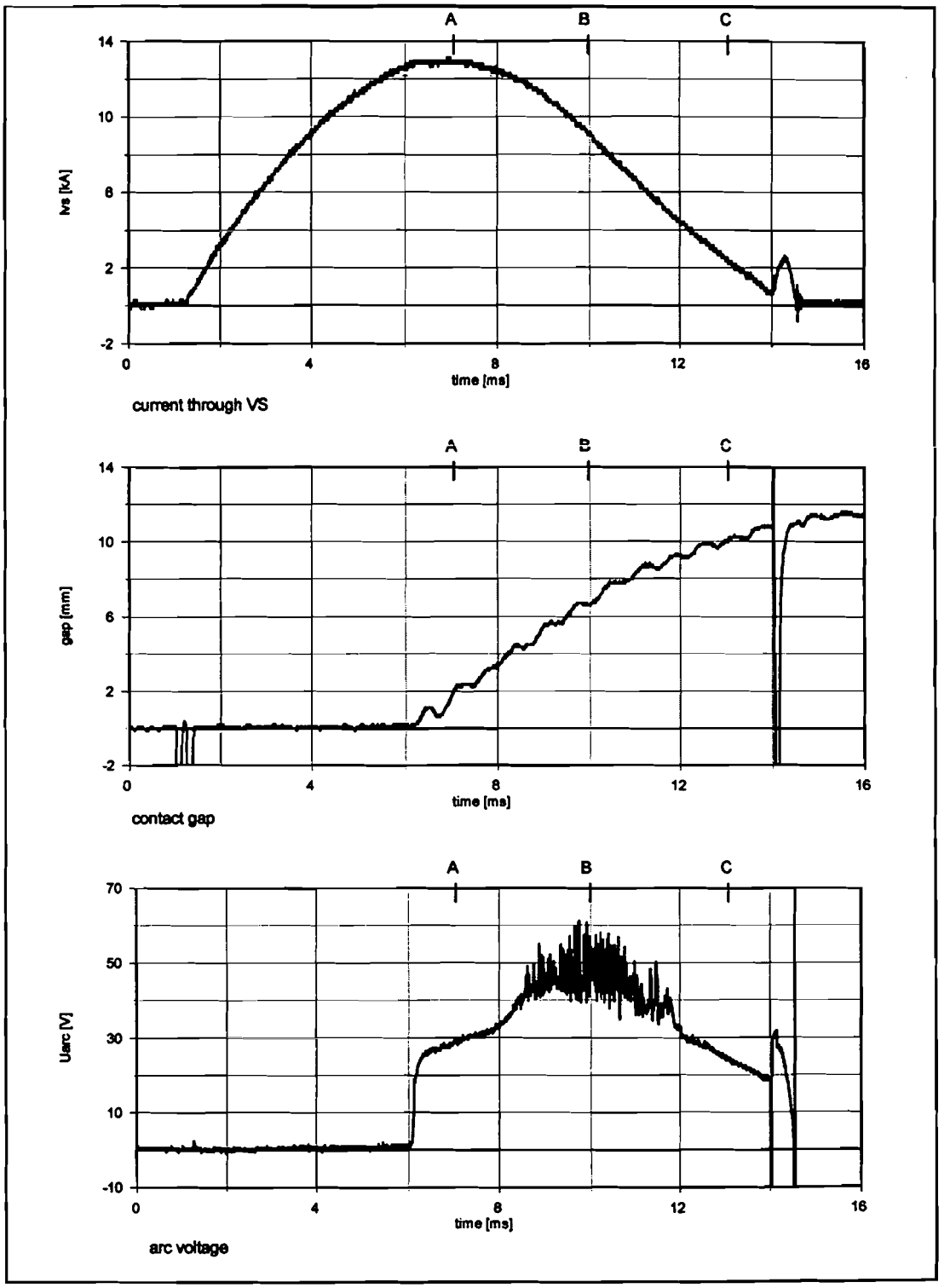

Figure 5-6: Measurement I13_53 used as configuration for the current contraction model.

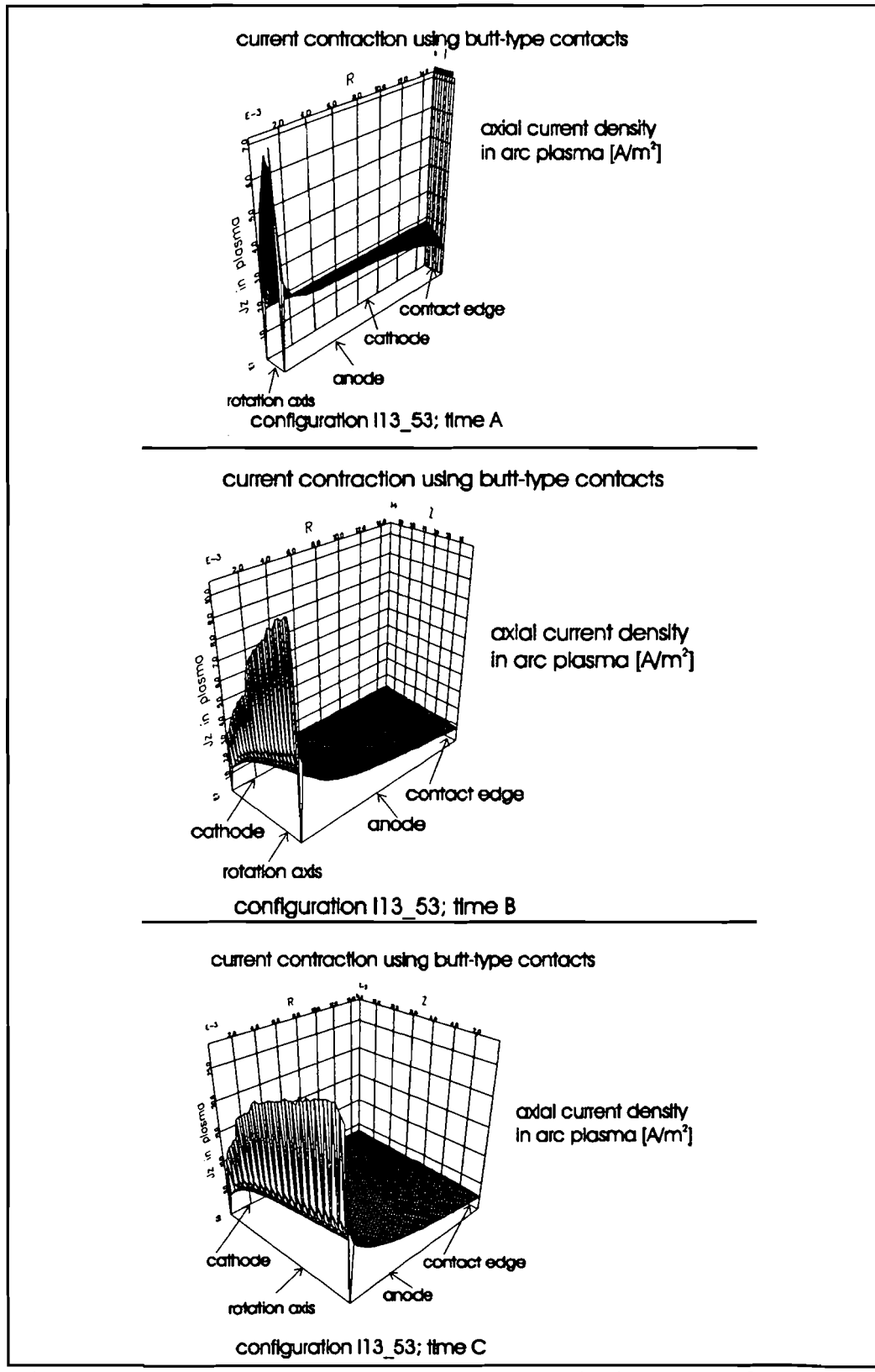

Figure 5-7: Calculations of the axial current density in the arc plasma.

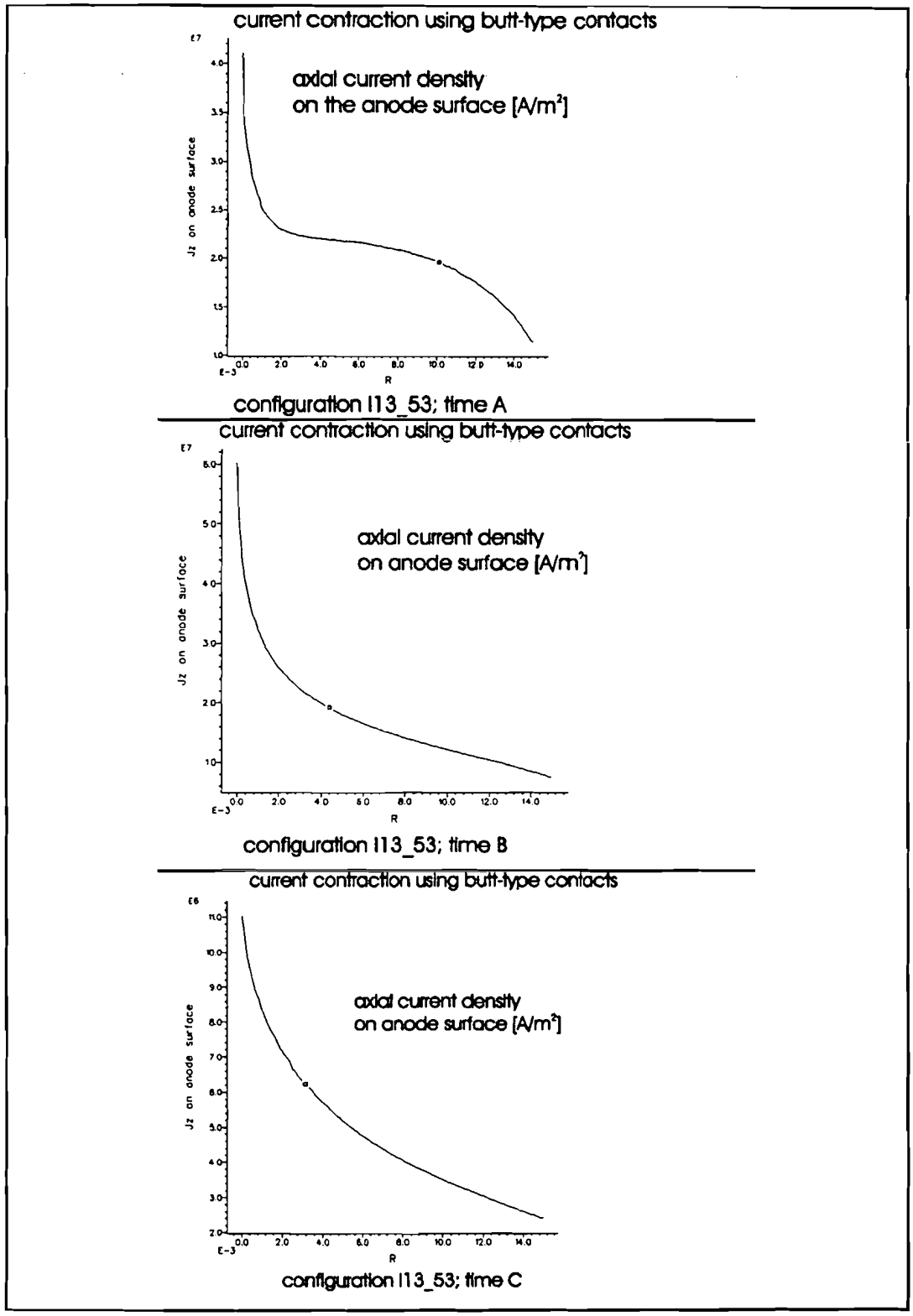

Figure 5-8: Calculations of the axial current density on the anode surface.

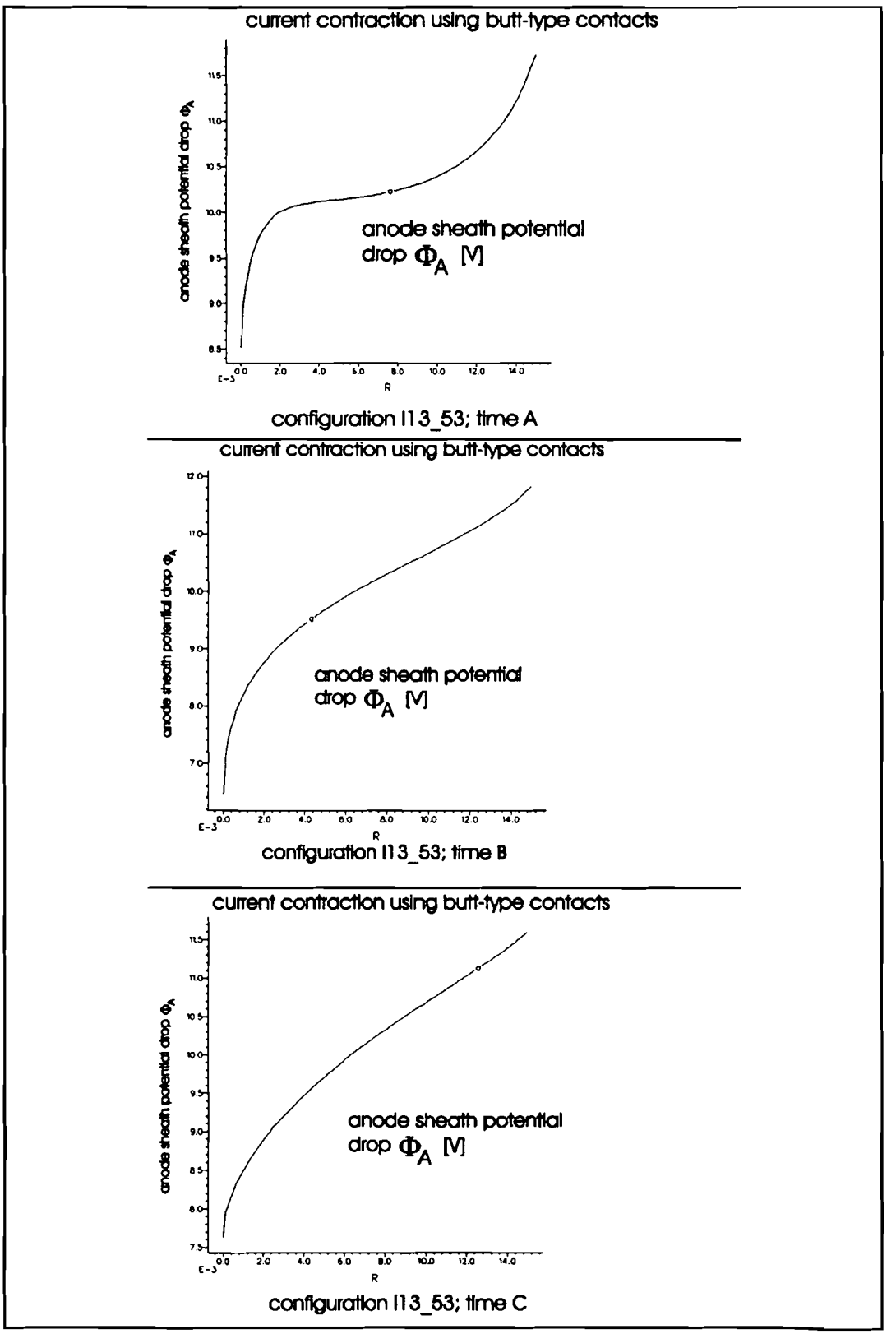

Figure 5-9: Calculations of the anode sheath potential drop Φ_A.

Figure 5-7 shows two strange negative peaks in the axial current density at the intersections of the rotation axis with the cathode and with the anode. These peaks are not present in Figure 5-8 although Figure 5-8 presents the axial current density on the anode surface. The peaks therefore probably represent a numerical problem. This numerical problem however has not been solved yet.

Figure 5-7 clearly shows an increasing contraction of the current towards the anode and corresponds to the expectations [Sch83][Izr85][Sha89][Wat96-1].

Figure 5-8 presents the axial current density on the anode. First thing to be remarked is the difference in current density profile at time A and at time B and C. The main difference between time A and the other two times is the small contact gap at time A (1.7 mm). The positive peak in the axial current density near the rotation axis at time A could be caused by problems at the rotation axis. The peak however also can be caused by a physical phenomenon. Schulman [BSc94] measures bridge columns during the first two milliseconds of arcing and Wieckert and Egli [Wie89] calculated comparable current density profiles.

Figure 5-8 also shows that the highest current density occurs at time B. Time B is located in the arc voltage oscillation area (Figure 5-6) and therefore is expected to have the highest current density. The oscillations in the arc voltage often are associated with arc instabilities and anode spot formation (chapter 2.1.1). Schellekens [Sch83] reports on current densities of $9 \cdot 10^7$ A/m^2 near anode spot formation.

Figure 5-9 presents the calculations of sheath potential drop Φ_A. Here time B has the lowest sheath potential drop and therefore is closest to the saturation current density. Figure 5-9 points into the direction of the theory proposed in chapter 4.3.1 but does not correspond to it. The theory proposed that the voltage oscillations occur when the saturation current density is reached. For a better comparison it is recommended to correlate the electron density to the current density.

The electron density is assumed to be constant. Schellekens [Sch83] however measured varying electron density. The electron density also affects the plasma conductivity and thereby affects the current density distribution in two ways.

According to the discussion above, the contraction model seems to work reasonably in the case of butt-type contacts. The results of the model however have to be compared to current density measurements to make a more substantial comparison.

If the contraction model is coupled to an anode heating model, more practical comparisons between anode spot formation and the temperature distribution in the anode material can be made. The coupling between the axial current density and the energy input into the anode has been described by several authors: [Jol82], [Box83], [Wie89], [Wat96-2].

Recommendations to improve the model are:

- Correlate the electron density to the current density;
- Couple the contraction model to an anode heating model;
- Take the secondary emission of particles from the anode into account.

The second recommendation of course is necessary for the third recommendation.

6. Conclusions

The recordings of the high speed camera were very useful for the interpretation of the interruption measurements.

After the interruption of high currents, current peaks can occur during the first quarter of the period of the recovery voltage. These current peaks seem to coincide with the maximum derivative of the recovery voltage. The current peaks were largest when using the contact materials CuCr and CuW.

Three main types of reignitions can be distinguished: dielectric, thermal and a combination of the former two. The reignitions for contact gaps between 0 and 3 mm had a predominantly dielectric character. Reignitions for contact gaps larger than 8 mm had a predominantly thermal character. Reignitions for contact gaps between 3 and 8 mm had no predominant character.

Many currents between 10 kA and 40 kA were interrupted during this investigation. At these high currents all electrodes suffered from anode spots. The materials without tungsten however were much more eroded than were the materials with tungsten.

The CuCr butt-type contacts had an excellent interruption performance for arc energies below approximately 1 kJ. The erosion of the contacts is not very high and the electric reignition field strength is high.

The Cu coil-type contacts suffered form severe erosion. Although the contacts were damaged badly, the electric reignition field strength remained rather high.

Between the contacts investigated in this project, the CuCr coil-type contacts were of the ones that are most suited for the interruption of short circuit currents. The erosion of these contacts is not very high and the average electric reignition field strength is high.

The CuW coil-type contacts had a very low erosion rate and a rather high electric reignition field strength but suffered from hot droplets of contact materials that probably initiated reignitions between the contacts and the screen of the vacuum tube. These reignitions between contacts and screen were accompanied by high (40 kV) voltage oscillations.

The AgWC coil-type contacts had a very low erosion rate but also had low electric reignition field strengths. The contacts are not very suited for the interruption of short circuit currents but the contacts are very well suited for "low surge breakers".

The first computional results of the current contraction model confirm the existence of current contraction on the anode of butt-type contacts. Many problems however still have to be solved. The greatest problems at this moment refer to the implementation of the model into a suitable finite element method program.

7. Recommendations

It is advised to do more research into the origin of the post-arc current peaks occurring at the first maximum derivative of the recovery voltage. The current peaks often are the start of a reignition and consequently can not be neglected.

The contact material CuW seems very promising for the interruption of high currents and it is advised to do further measurements with this contact material. Perhaps the composition of the contact material can be changed a little in order to get a better interruption performance than in the case of CuCr.

Finally it is recommended to continue with the development of the anode spot model. The results of the complete model should also include computation of metal vapor production at current zero, one of the most important parameters for the reignition characteristics.

References

[And71] Andrews, J.G. and R.H. Varey, "SHEATH GROWTH IN A LOW PRESSURE PLASMA", The Physics of Fluids, Vol. 14 (1971), No. 2, p. 339-343.

[Mit73] Mitchner, M. and C.H. Kruger Jr., "PARTIALLY IONIZED GASES", Chichester: Wiley-Interscience, 1973. ISBN: 0-471-61172-7

[Mor73] Morimiya, O. and S. Sohma, T. Sugawara, H. Mizutani, "HIGH CURRENT VACUUM ARCS STABILIZED BY AXIAL MAGNETIC FIELDS", IEEE PES WM 73 (1973), p. 1723-1732.

[McC74] McClure, G.W., "PLASMA EXPANSION AS A CAUSE OF METAL DISPLACEMENT IN VACUUM-ARC CATHODE SPOTS", Journal of Applied Physics, Vol. 45 (1974), No. 5, p. 2078-2084.

[Daa78] Daalder, J.E., "CATHODE EROSION OF METAL VAPOUR ARCS IN VACUUM", Eindhoven (The Netherlands), Eindhoven University of Technology, 1978. Doctoral thesis.

[CRC82] "HANDBOOK OF CHEMISTRY AND PHYSICS", 62nd edition (1982). The Rubber Company (USA).

[Jol82] Jolly, D.C., "ANODE SURFACE TEMPERATURE AND SPOT FORMATION MODEL FOR THE VACUUM ARC", Journal of Applied Physics, Vol. 53 (1982), No. 9, p. 6121-6126.

[Box83] Boxman, R.L. and S. Goldsmith, "MODEL OF THE ANODE REGION IN A UNIFORM MULTI-CATHODE-SPOT VACUUM ARC", Journal of Applied Physics, Vol. 54 (1983), No. 2, p. 592-602.

[Mil83] Craig Miller, H., "VACUUM ARC ANODE PHENOMENA", IEEE transactions on plasma science, Vol. PS-11 (1983), No. 2, p. 76-89.

[Sch83] Schellekens, H., "MODELLING OF THE DIFFUSE ARC IN A VACUUM CIRCUIT BREAKER", Eindhoven (The Netherlands), Eindhoven University of Technology, 1983. Doctoral thesis.

[Aga84] Agarwal, M.S. and R. Holmes, "ARCING VOLTAGE OF THE METAL VAPOUR VACUUM ARC", Journal of Physics D: Applied Physics, Vol. 17 (1984), pp.757-767.

[Beh84] Behrens, Fr.-W. and A. Erk, "INTERRUPTING CAPACITY OF VACUUM CIRCUIT BREAKERS AS A FUNCTION OF CONTACT GEOMETRY", In: 12th International conference on electric contact phenomena. Chicago september 1984, p. 178-186.

[Beh85] Behrens, FW., "BOGENWANDERUNG, BOGENFORM UND LÖSCHVERMÖGEN BEI VERSCHIEDENEN ELECTRODENANORDNUNGEN FÜR VAKUUMLEISTUNGSSCHALTER", In: 5th International symposium on switching arc phenomena. Lódz. 24-26 September 1985.

[Izr85] Izraeli, I. "SPATIAL DISTRIBUTION OF THE ELECTRICAL CURRENT IN THE METAL VAPOR OF VACUUM ARCS", Tel-Aviv (Israel), Tel-Aviv University, 1985. Doctoral thesis.

[Mil85] Graig Miller, H., "A REVIEW OF ANODE PHENOMENA IN VACUUM ARCS", IEEE transactions on plasma science, Vol. PS-13 (1985), No. 5, p. 242-252.

[BIN86] "BINAS", Wolters-Noordhoff, 2e druk, 1986. ISBN 900189351 1.

[Yan85] Yanabu, S. and M. Homma, E. Kaneko, T. Tamagawa, "POST ARC CURRENT OF VACUUM INTERRUPTERS", IEEE Transaction on Power Apparatus and Systems, Vol. PAS-104 (1985), No. 1, p. 166-172.

[Yan86] Yanabu, S. and Y. Satoh, M. Honma, T. Tamagawa, E. Kaneko, "POST ARC CURRENT IN VACUUM INTERRUPTERS", IEEE Transactions on Power Delivery, Vol. PWRD-1 (1986), No.4, p.209-214.

[Gol87] Goldsmith, S. and R.L. Boxman, E. Sapir, Y. Cohen, H. Yaloz, N. Brosh, "DISTRIBUTION OF PEAK TEMPERATURE AND ENERGY FLUX ON THE SURFACE OF THE ANODE IN A MULTI-CATHODE SPOT PULSED VACUUM ARC", IEEE Transactions on Plasma Sience, Vol. PS-15 (1987), No. 5, p.510-514.

[Mit87] Mitterauer, J. and P. Till, "COMPUTER SIMULATION OF THE DYNAMICS OF PLASMA-SURFACE INTERACTIONS IN VACUUM ARC CATHODE SPOTS", IEEE Transactions on Plasma Sience, Vol. PS-15 (1987), No. 5, p.488-501.

[Oka87] Okawa, M. and S. Yanabu, E. Kaneko, K. Otobe, "THE INVESTIGATION OF COPPER-CHROMIUM CONTACTS IN VACUUM INTERRUPTERS SUBJECTED TO AN AXIAL MAGNETIC FIELD", IEEE Transactions on Plasma Sience, Vol. PS-15 (1987), No. 5, p. 533-537.

[Yan87] Yanabu, S. and M. Okawa, E. Kaneko, T. Tamagawa, "USE OF AXIAL MAGNETIC FIELDS TO IMPROVE HIGH CURRENT VACUUM INTERRUPTERS", IEEE Transactions on Plasma Sience, Vol. PS-15 (1987), No. 5, p. 524-532.

[Nem89] Nemchinskii, V.A., "CALCULATION OF THE INFLUENCE OF AN AXIAL MAGNETIC FIELD ON THE FORMATION OF ANODE SPOTS IN A VACUUM ARC", Sovjet Physics Technical Physics, Vol.34 (1989), No. 9, p. 1014-1017.

[Sha89] Shang, W-K, "THEORETICALLY ANALYSIS THE CURRENT CONSTRICTION PHENOMENA OF VACUUM ARCS AND THE INFLUENCE OF AXIAL MAGNETIC FIELD", In: Proceedings of the ECAAA. Xian, 1989, p. 116-120.

[Wie89] Wieckert, C. and W. Egli, "THEORETICAL ANALYSIS OF THE CURRENT AND ENERGY FLOW TO THE ANODE IN THE DIFFUSE VACUUM ARC", IEEE Transactions on Plasma Sience, Vol. 17 (1989), No. 5, p. 649-652.

[Sch93-1] Schellekens, H. and W. Shang, K. Lenstra, "CALCULATION OF THREE-DIMENSIONAL MAGNETIC FIELD FOR HORSESHOE ELECTRODE OF VACUUM INTERRUPTERS", ETEP, Vol. 3 (1993), No. 4, p. 299-303.

[Sch93-2] Schellekens, H. and W. Shang, K. Lenstra, "VACUUM INTERRUPTER DESIGN BASED ON ARC MAGNETIC FIELD INTERACTION FOR HORSESHOE ELECTRODE", IEEE Transactions on Plasma Sience, Vol. 21 (1993), No. 5, p. 469-473.

[BSc93] Schulman, M.B., "SEPERATION OF SPIRAL CONTACTS AND THE MOTION OF VACUUM ARCS AT HIGH AC CURRENTS", IEEE Transactions on Plasma Sience, Vol. 21 (1993), No. 5, p. 484-488.

[Mac94] Macken, K.J.P., "ONTWERP EN REALISATIE VAN EEN SYNTHETISCH TESTCIRCUIT VOOR VACUγMSCHAKELAARS", Faculteit Elektrotechniek, Technische Universiteit Eindhoven, 1994. Stageverslag EG/94/736.S.

[BSc94] Schulman, M.B., "EVALUATION OF AC AXIAL MAGNETIC FIELDS NEEDED TO PREVENT ANODE SPOTS IN VACUUM ARCS BETWEEN OPENING CONTACTS", IEEE Transactions on Components, Packaging and Manufacturing Technology - Part A, Vol. 17, (1994), No. 1, p. 53-57.

[Sme94] Smeets, R.P.P., "VERMOGENSSCHAKELAARS IN DE ELEKTRICITEITSNETTEN", Faculteit Elektrotechniek, Technische Universiteit Eindhoven, 1994. Collegedictaat 5784.

[Bin95] Binnendijk, M., "THE EFFECT OF CONTACT DISTANCE ON HIGH CURRENT INTERRUPTION IN VACUUM", Faculteit Elektrotechniek, Technische Universiteit Eindhoven, 1995. Afstudeerverslag EG/95/771.A..

[Wat96-1] Watanabe, K. and E. Kaneko, S. Yanabu, "TECHNOLOGICAL PROGRESS OF AXIAL MAGNETIC FIELD VACUUM INTERRUPTERS", In: XVIIth International Symposium on Discharges and Electrical Insulation in Vacuum. Berkely, 1996, p. 231-239.

[Wat96-2] Watanabe, K. and J. Sato, K. Kagenaga, H. Somei, M. Homma, E. Kaneko, H. Takahashi, "THE ANODE SURFACE TEMPERATURE OF CuCr CONTACTS AT THE LIMIT OF CURRENT INTERRUPTION", In: XVIIth International Symposium on Discharges and Electrical Insulation in Vacuum. Berkely, 1996, p. 291-295.

Appendix A: Equipment

C_m	: Capacitor battery. 32 cpacitors of 127.8 μF parallel; maximum voltage 15 kV. Total C = 890 μF. Each capacitor is short circuit protected with an inductance.
T1	: Distribution transformer. 10kV/400V; S = 800 kVA; Dy5; ε_{sc} = 3.64%.
C_{inj}	: Capacitor. C = 27.8 μF; maximum voltage 15 kV.
C_{trv}	: Capacitor. C = 10 nF; maximum voltage 30 kV.
L_{inj}	: Torodial coil. L = 885 μH; maximum current 5 kA. Designed at TUE.
L_d	: Coil. L = 32 μH.
S1	: Circuit breaker. ABB RM12•35; low oil volume breaker.
S2	: Circuit breaker. Toshiba SVB-10M40E; vacuum circuit breaker.
VS	: Sectional vacuum tube (see appendix B) with switching mechanism. Used to test contacts. Pressure inside the sectional vacuum tube is lower than 10^{-6} mbar.
I_r	: High current measurement. Rogowski coil in combination with matching integrator. Designed at TUE. Sensitivity without attenuator: 25.3 kA/V. Integrator connected to oscilloscope 1.
I_p	: Post arc current measurement. Pearson current transformer. Output clipped with two diode arrays consisting of 10 diodes each and switched anti-parallel. Sensitivity: 200A/V. Diodes: high speed silicon diode BAW62; repetitive peak forward current 225 mA maximum. Current transformer connected to oscilloscope 2.

U_{vs1}	: Arc voltage measurement. Probe: Tektronix P6015A (TUE id.: EG3103 SD14); 1:1000; accuracy 2%; bandwidth: 75 MHz. Probe connected to oscilloscope 1.
U_{vs2}	: Recovery voltage measurement. Probe: Tektronix P6015; 1:1000; accuracy 9%; bandwidth: 70 MHz. Probe connected to oscilloscope 2.
U_{screen}	: Screen voltage measurement. Probe: Tektronix P6015A (TUE id.: EG3104 SD15); 1:1000; accuracy 2%; bandwidth: 75 MHz. Probe connected to oscilloscope 1.
Oscilloscope 1	: LeCroy 9314M (TUE id: EG3096). 4 channels; 300 Msamples/s; 8 bit; 50 kbyte acquisition memory per channel.
Oscilloscope 2	: Lecroy 9400 (TUE id: EG3011 0F46). 2 channels; 100Msamples/s; 8 bit; 32 kbyte acquisition memory per channel.
Contact gap	: TPA laser displacement measuring system; accuracy 0.2 mm.
Vacuum level	: The pressure in the sectional vacuum tube VS (see appendix B) is measured indirectly by measuring the current of the ion getter pump.
High speed camera	: Designed at KEMA. 16 X 10 matrix of glass fibres. Each fibre is connected to an optical receiver. The signals of the optical receivers are converted by a 4-bits A/D converter with a logaritmic conversion characteristic. Maximum sample rate is 10^6 images/second. The camera has a memory for 1638 images.
Balance	: Sartorius AC 210; accuracy: 0.1 mg; range 0-210 g.

Appendix B: Drawing of the sectional vacuum tube

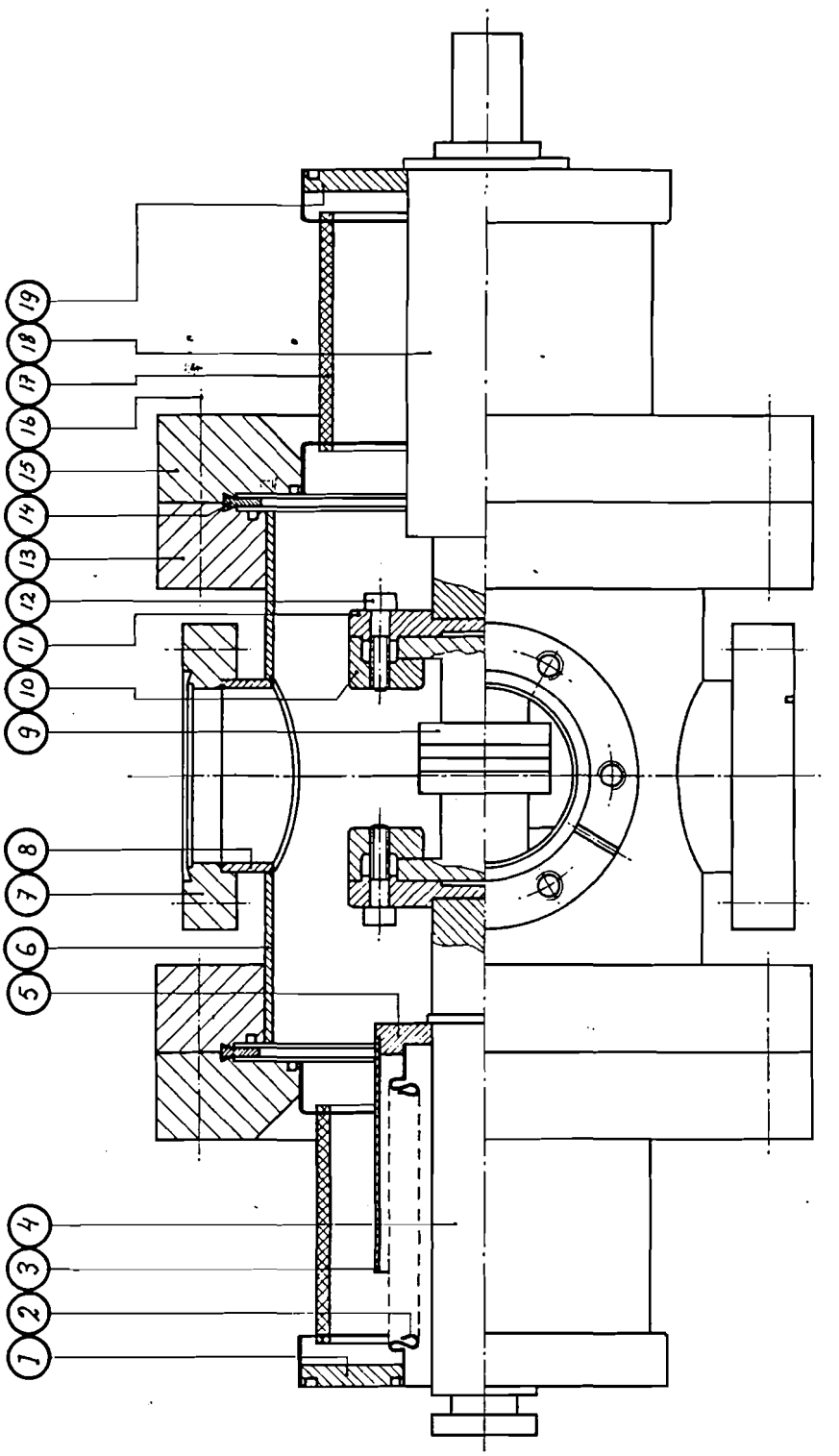

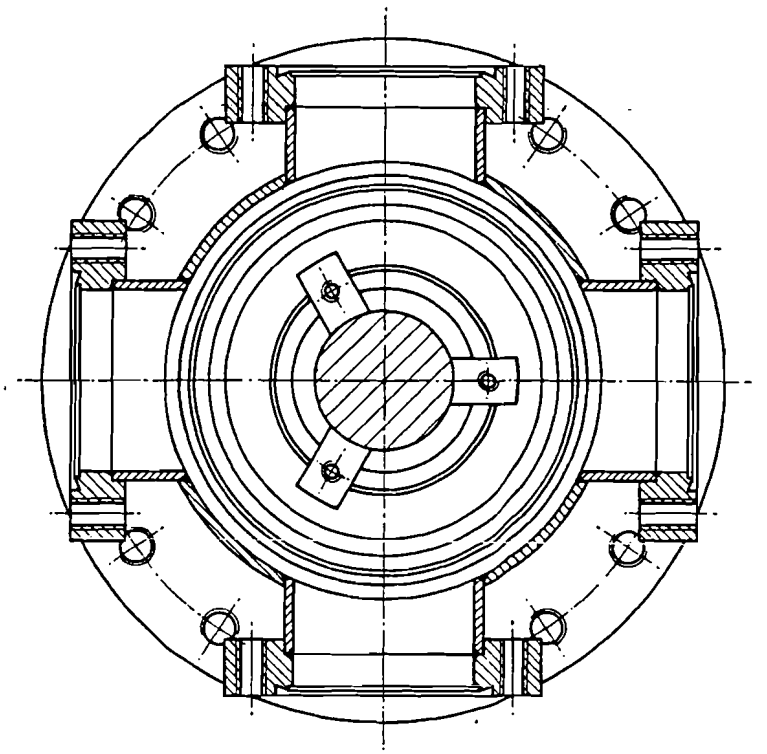

STUK NR.	AANTAL	BENAMING	MATERIAAL	NORMAAL MAGAZIJN	DETAIL TEK. NR.	OPMERKINGEN
19	1	Schijf	RVS 316		EH 116-19	
18	1	Vaste as	koper zuurstofvrij		EH 116-18	
17	2	Isolator			EH 116-17	Hazemeyer.
16	32	Bout zesk kop	RVS 316	M8x40		
15	2	Flens 6"	RVS 316		EH 116-15	
14	2	Afdichtingsring	koper			Varian
13	2	Flens 6"	RVS 316		EH 116-13	
12	6	Bout inw zesk	RVS 316	M4x18		
11	2	Kontaktbhouder	RVS 316		EH 116-11	
10	6	Beugel	RVS 316		EH 116-10	
9	2	Kontakt drager	koper zuurstofvrij		EH 116-9	
8	4	Pijp	RVS 321		EH 116-8	
7	4	Flens 2 3/4"	RVS 316		EH 116-7	
6	1	Huis	RVS 304		EH 116-6	
5	1	Verloopring	RVS 316		EH 116-5	
4	1	Beweegbare as	koper zuurstofvrij		EH 116-4	
3	1	Pijp	RVS 316		EH 116-3	
2	1	Balg	RVS		EH 116-2	Haze meyer.
1	1	Schijf	RVS 316		EH 116-1	

I.S.O.-TOLERANTIES VOLGENS:	NIET GETOLEREERDE MATEN VOLGENS:			RUWHEIDSTEKENS VOLGENS NEN 630			PROJECTIEMETHODE:		
BEHANDELING:	SCHAAL: 1:1			WIJZ.	PARAAF	D.D.	WIJZ.	PARAAF	D.D.
	GET.: V Gompel	D.D.: 22/9-92							
	GEC.:	D.D.							
	GEZ.:	D.D.							
ONDERWERP: VACUUMSCHAKELAAR				VERVANGT TEK.:					
				VERVANGEN DOOR TEK.:					
BESTEMD VOOR:				BEHOORT BIJ TEK.:					
TECHNISCHE HOGESCHOOL EINDHOVEN				FORMAAT: A1	TEKENING NR.: EH 116				
AFDELING: E	SECTIE: EH			WIJZ.					

Appendix C: Measurement results

Table C-1: Erosion rates.

contact type		CuCr butt-type	Cu coil-type	CuCr coil-type	CuW coil-type	AgWC coil-type
erosion rate	anode [µg/C]	52.6	1276	52.6	-41.4	19.6
	cathode [µg/C]	159.6	185.0	102.5	66.3	21.9
total arc charge [C]		3316	3324	6192	4688	3514
maximum arc current [kA]		36.46	26.69	39.14	29.24	33.02

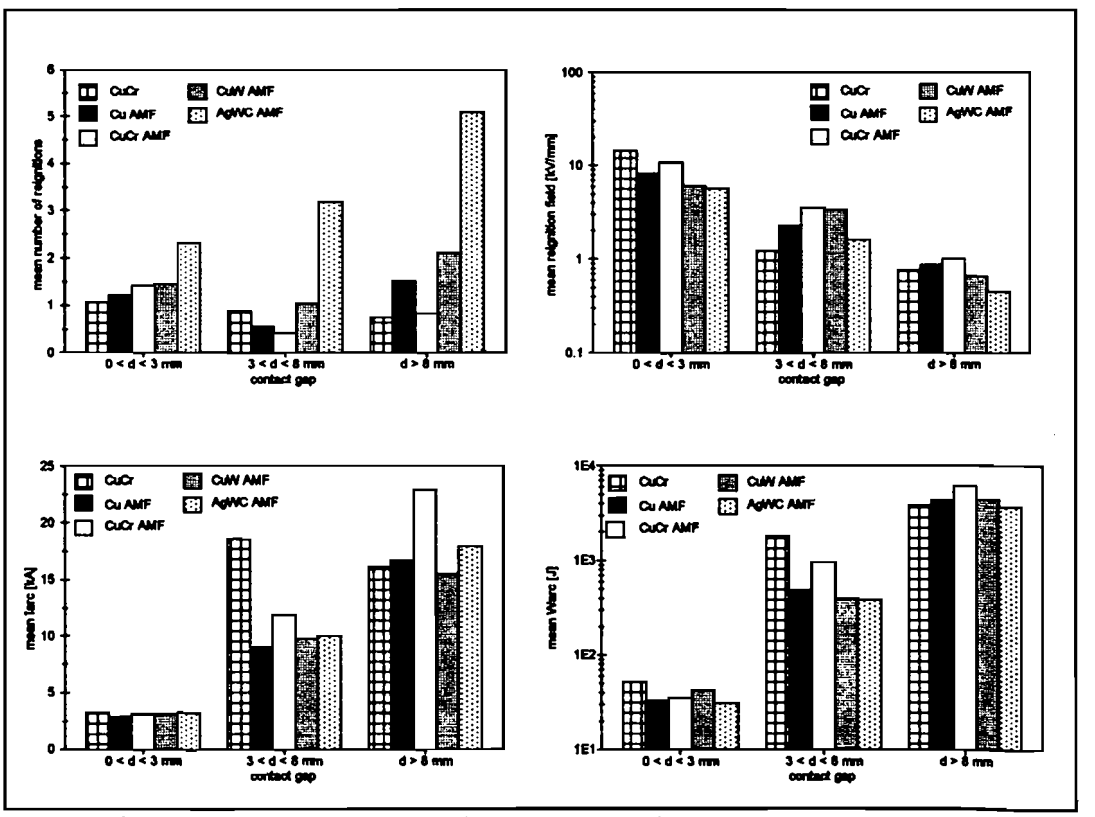

Figure C-1: Some mean results of the interruption measurements.

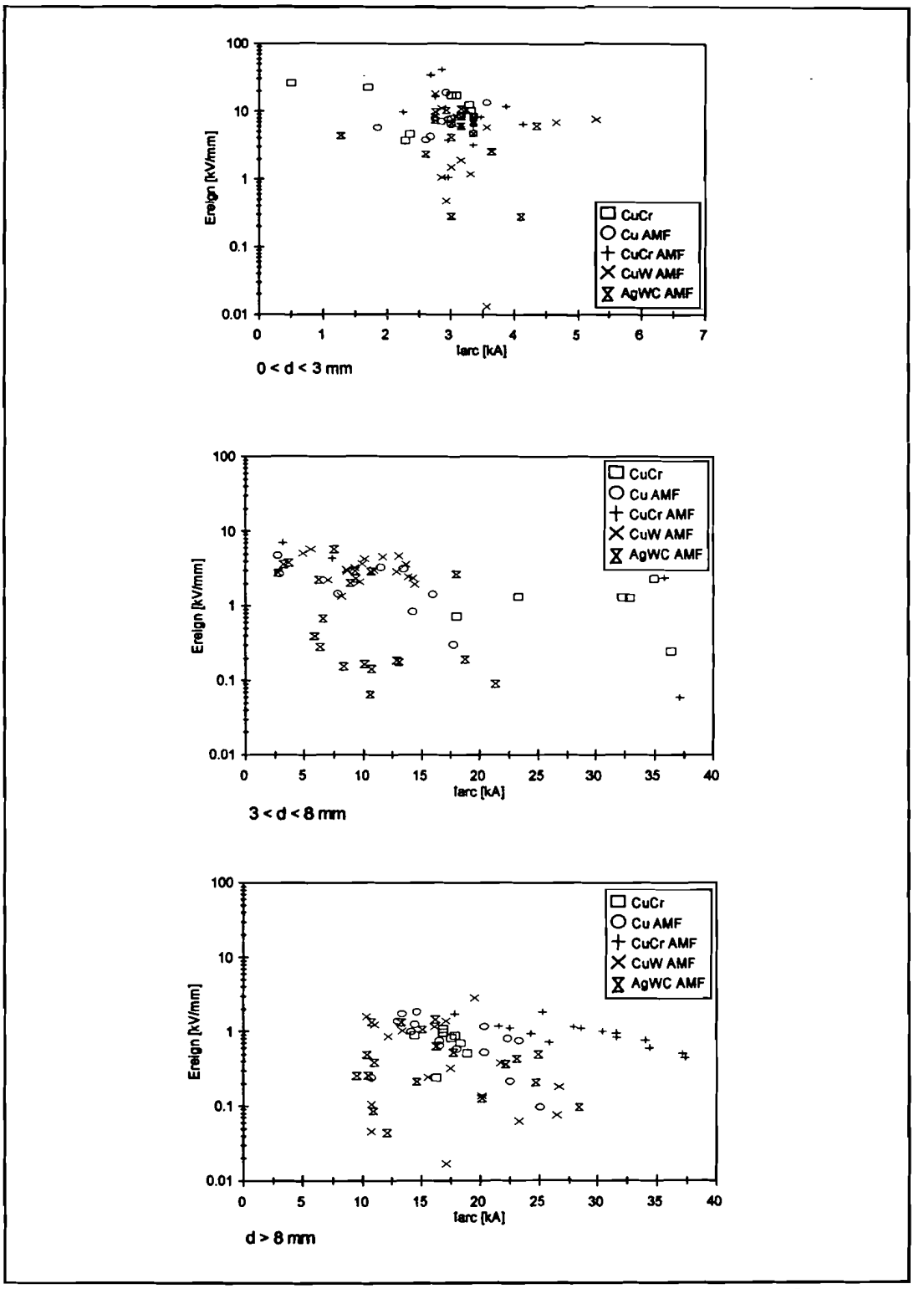

Figure C-2: Correlation between electric reignition field strength and maximum arc current.

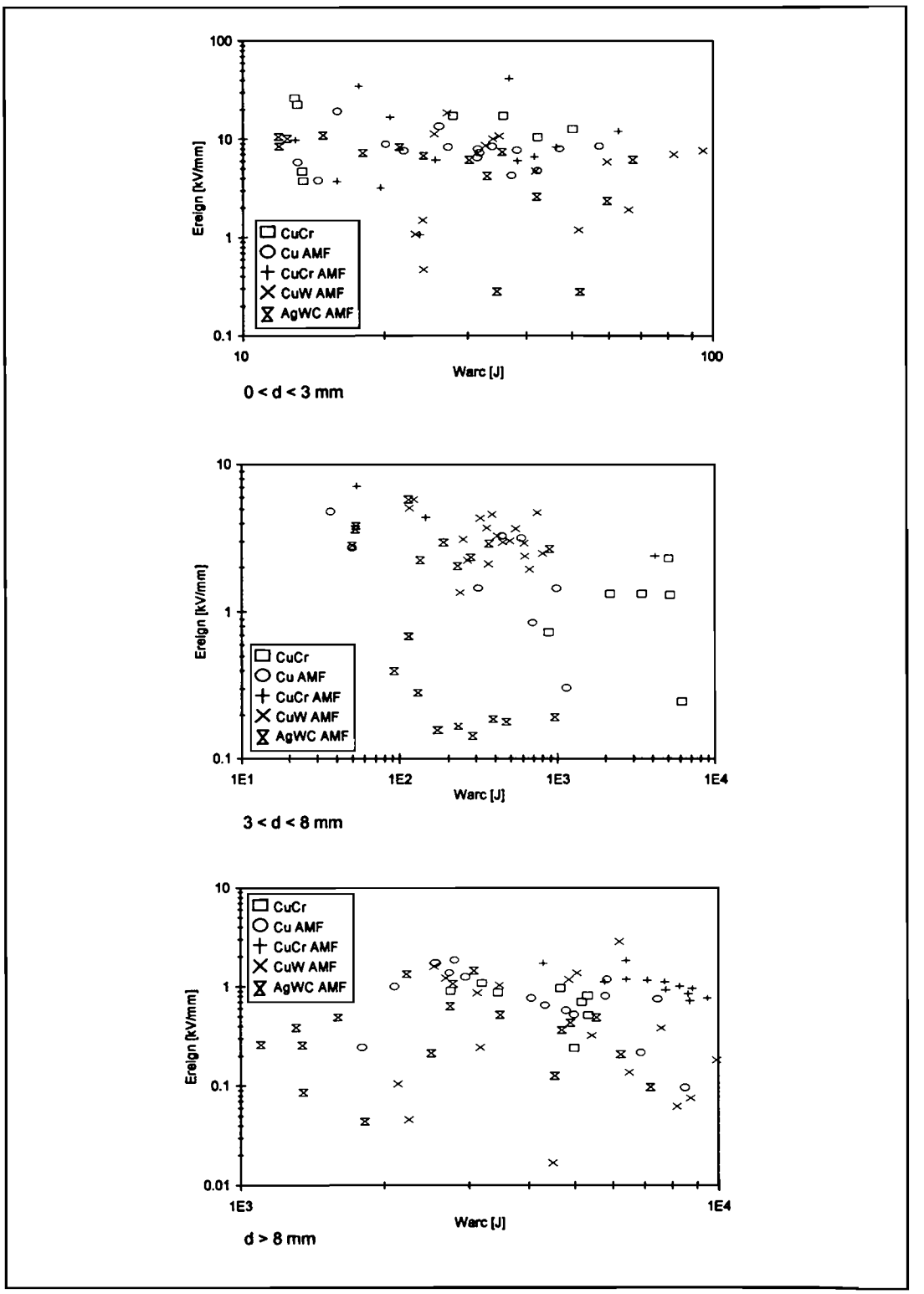

Figure C-3: Correlation between electric reignition field strength and arc energy.

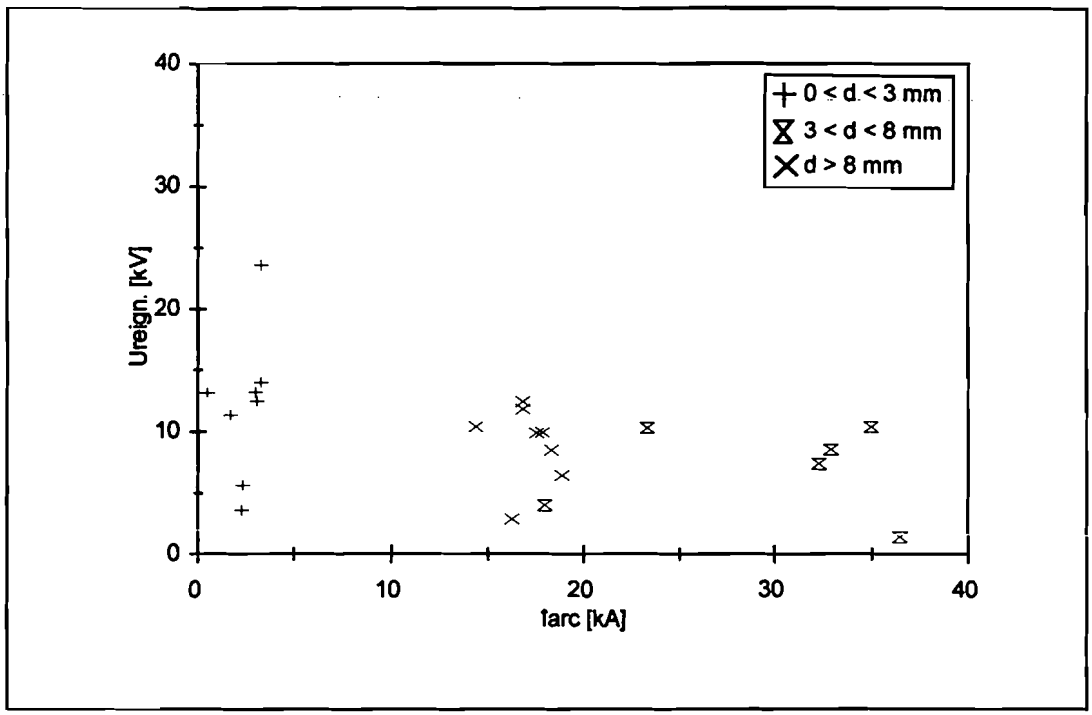

Figure C-4: Correlation between reignition voltage and maximum arc current for the CuCr butt-type contacts.

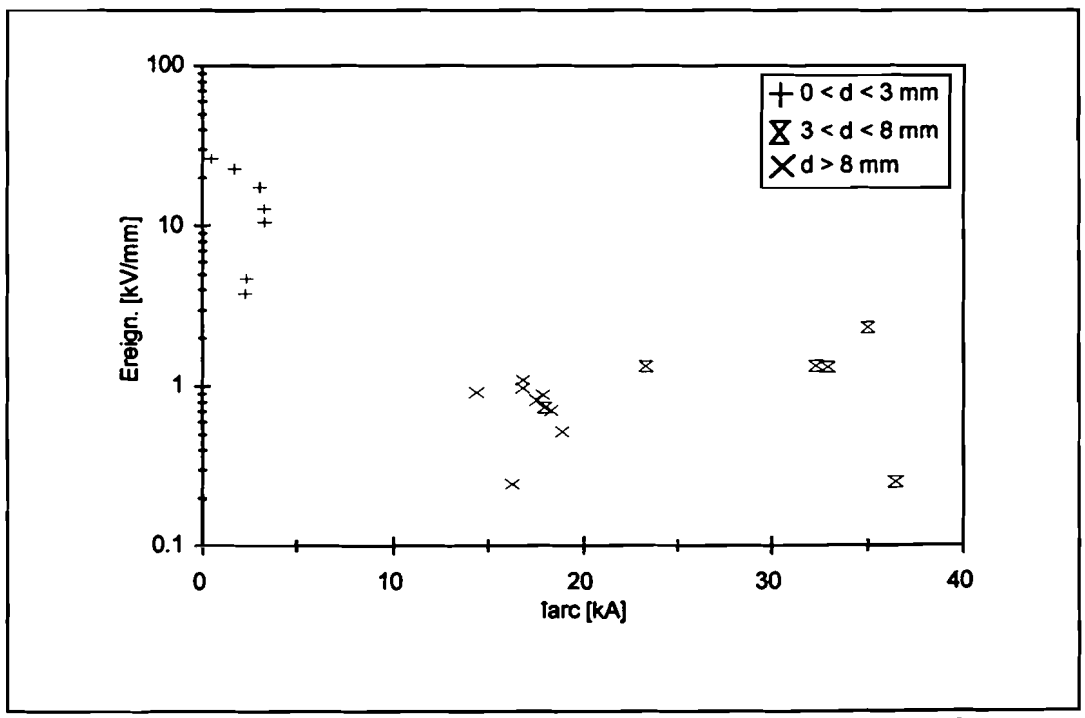

Figure C-5: Correlation between electric reignition field strength and maximum arc current for the CuCr butt-type contacts.

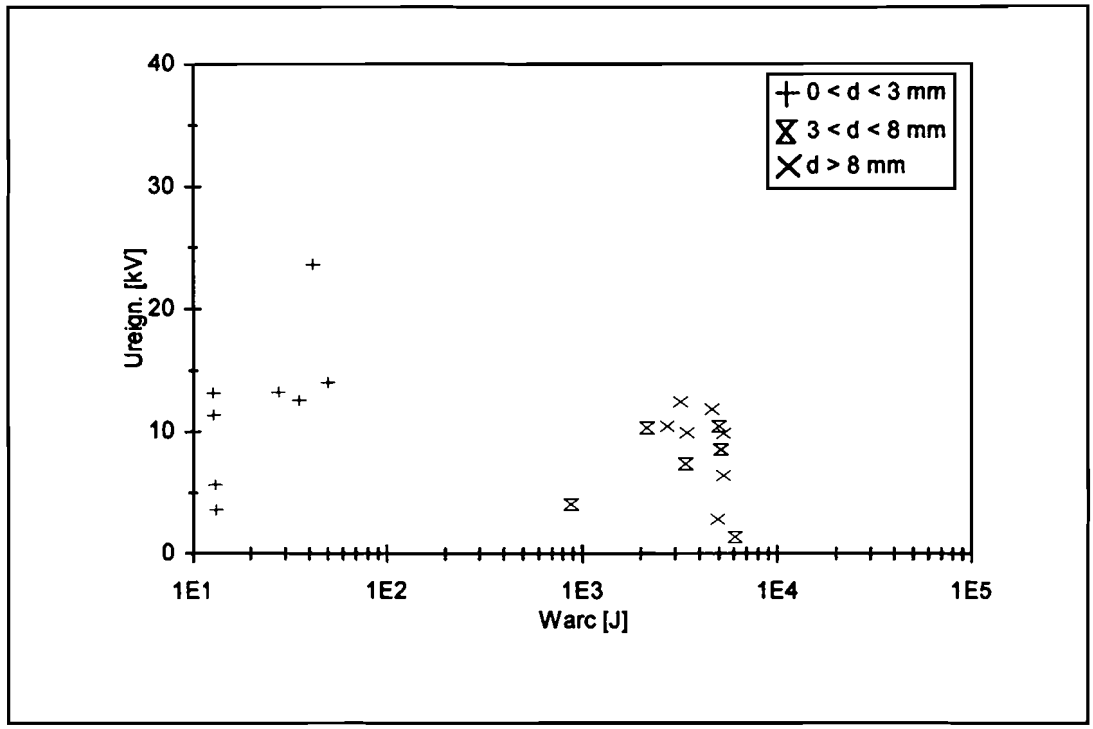

Figure C-6: Correlation between reignition voltage and arc energy for the CuCr butt-type contacts.

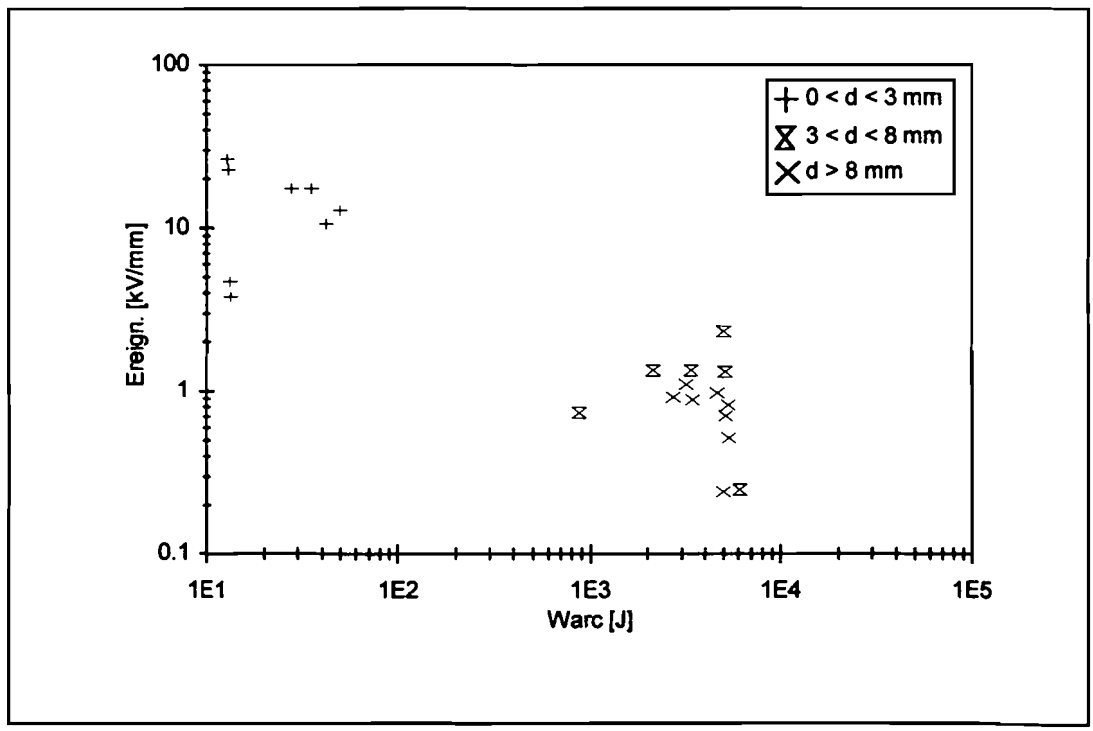

Figure C-7: Correlation between electric reignition field strength and arc energy for the CuCr butt-type contacts.

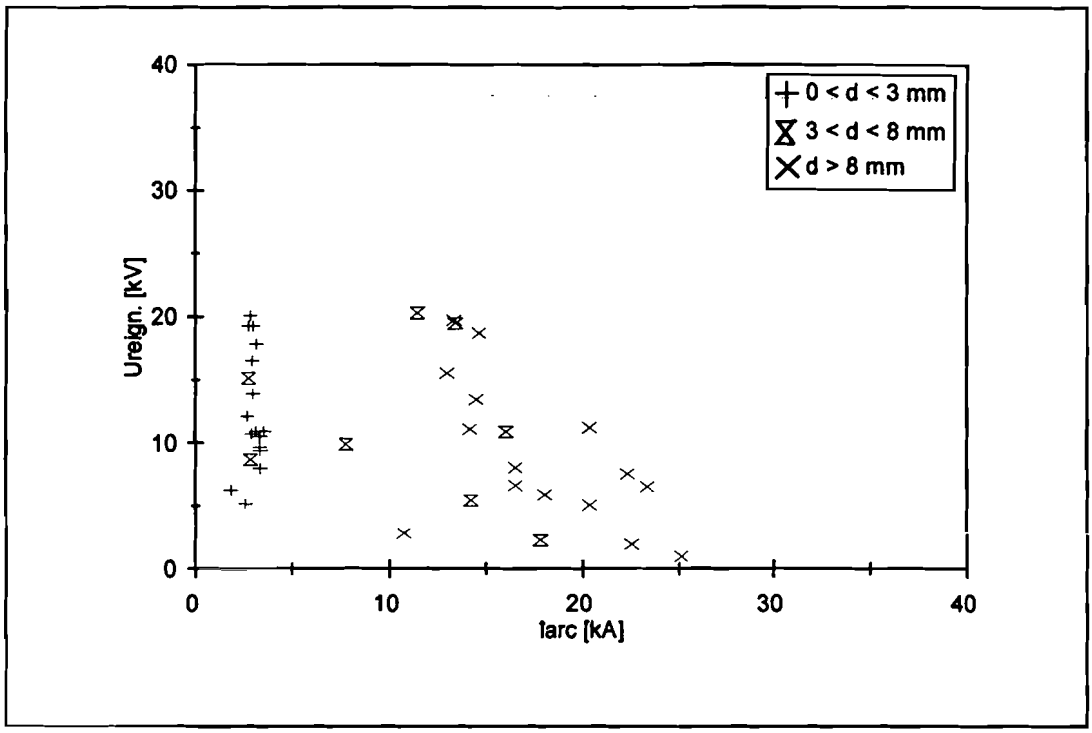

Figure C-8: Correlation between reignition voltage and maximum arc current for the Cu coil-type contacts.

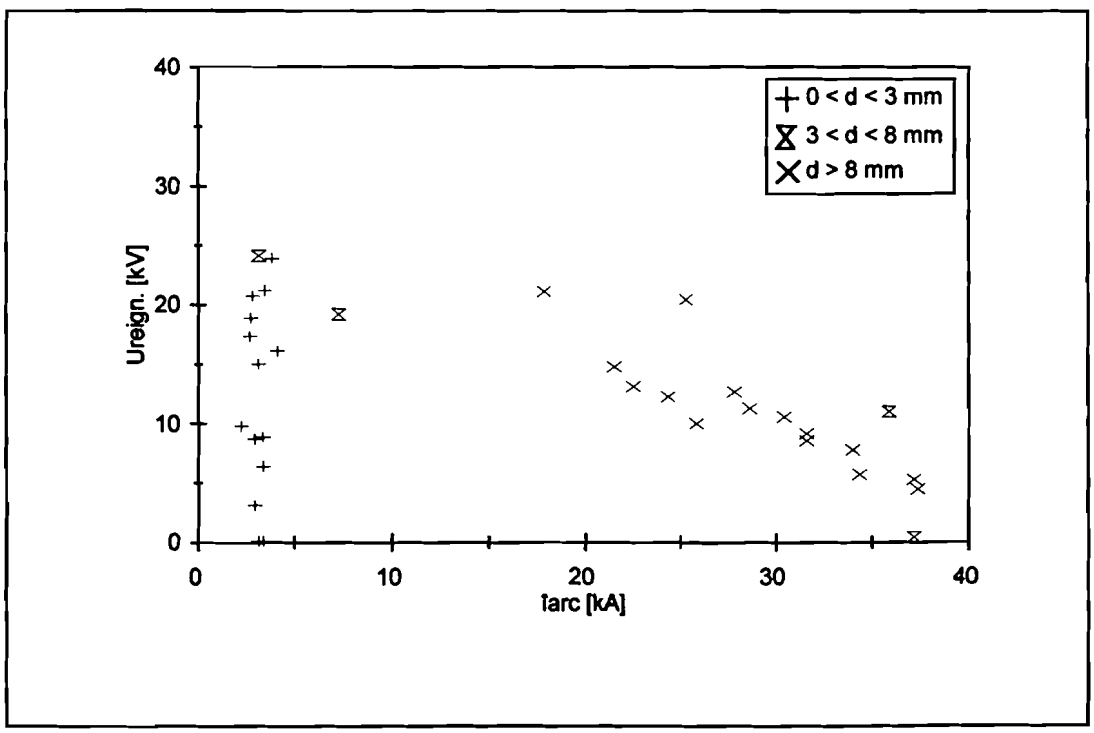

Figure C-9: Correlation between reignition voltage and maximum arc current for the CuCr coil-type contacts.

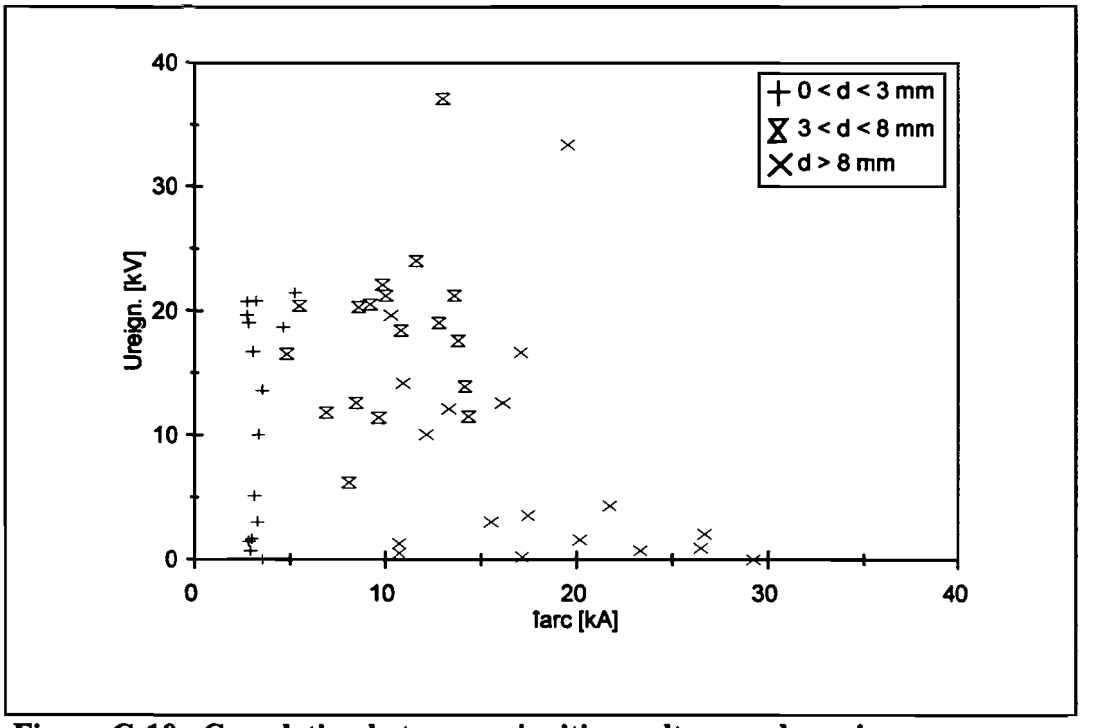

Figure C-10: Correlation between reignition voltage and maximum arc current for the CuW coil-type contacts.

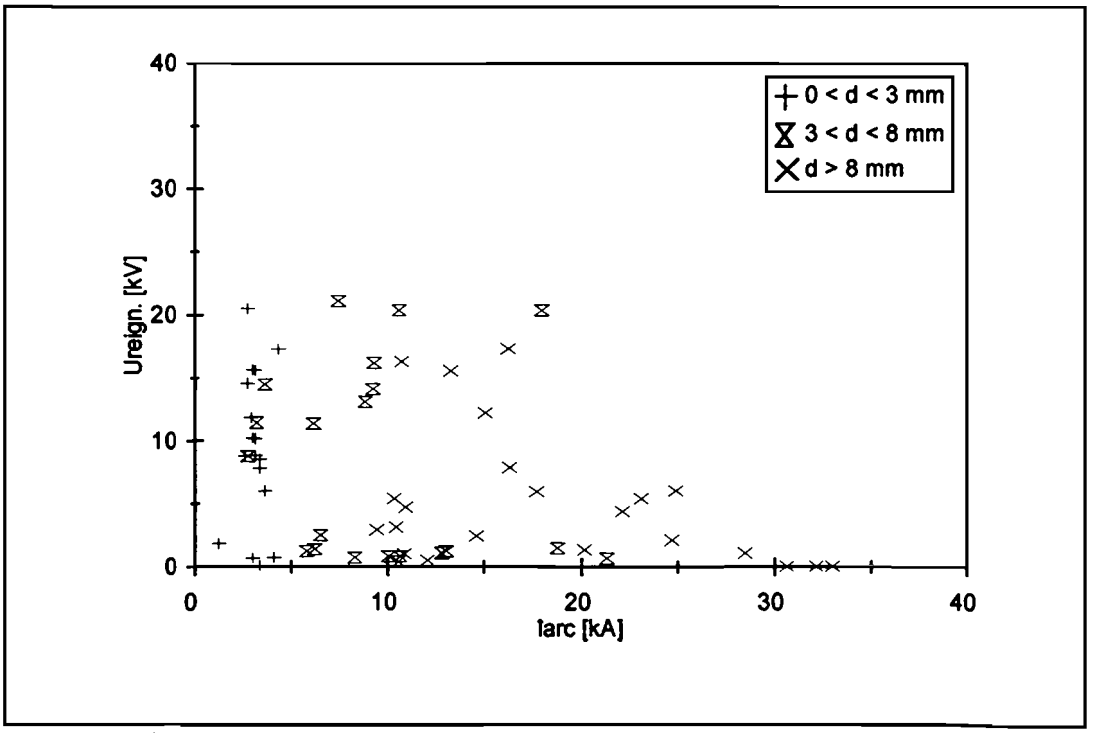

Figure C-11: Correlation between reignition voltage and maximum arc current for the AgWC coil-type contacts.

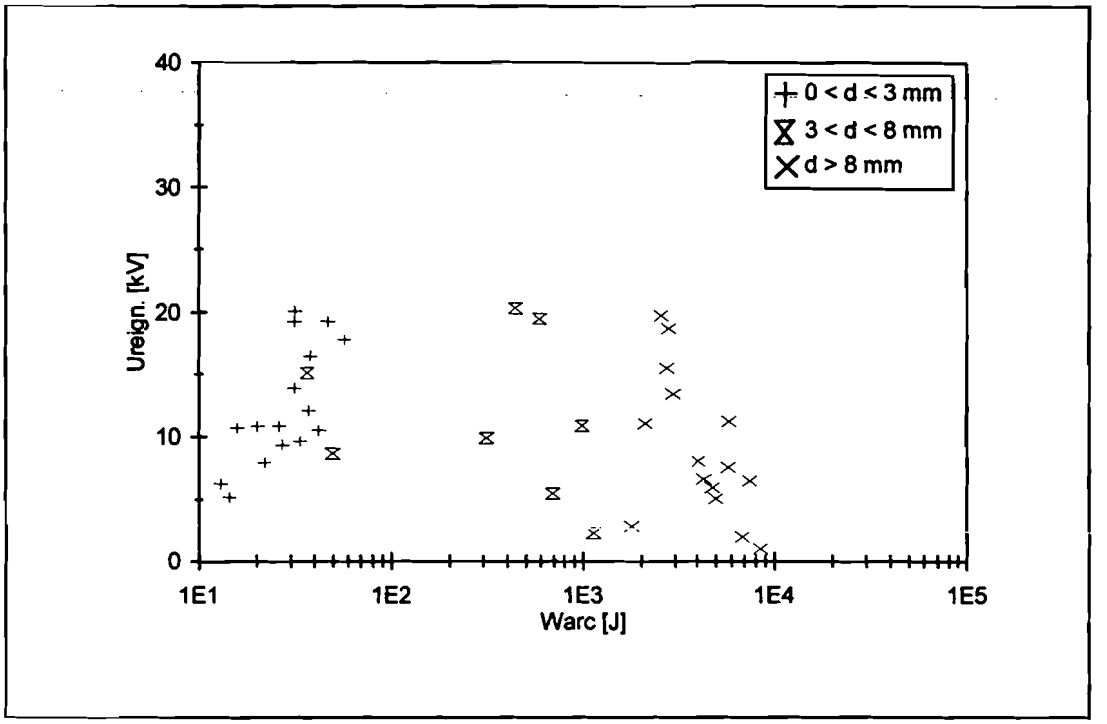

Figure C-12: Correlation between reignition voltage and arc energy for the Cu coil-type contacts.

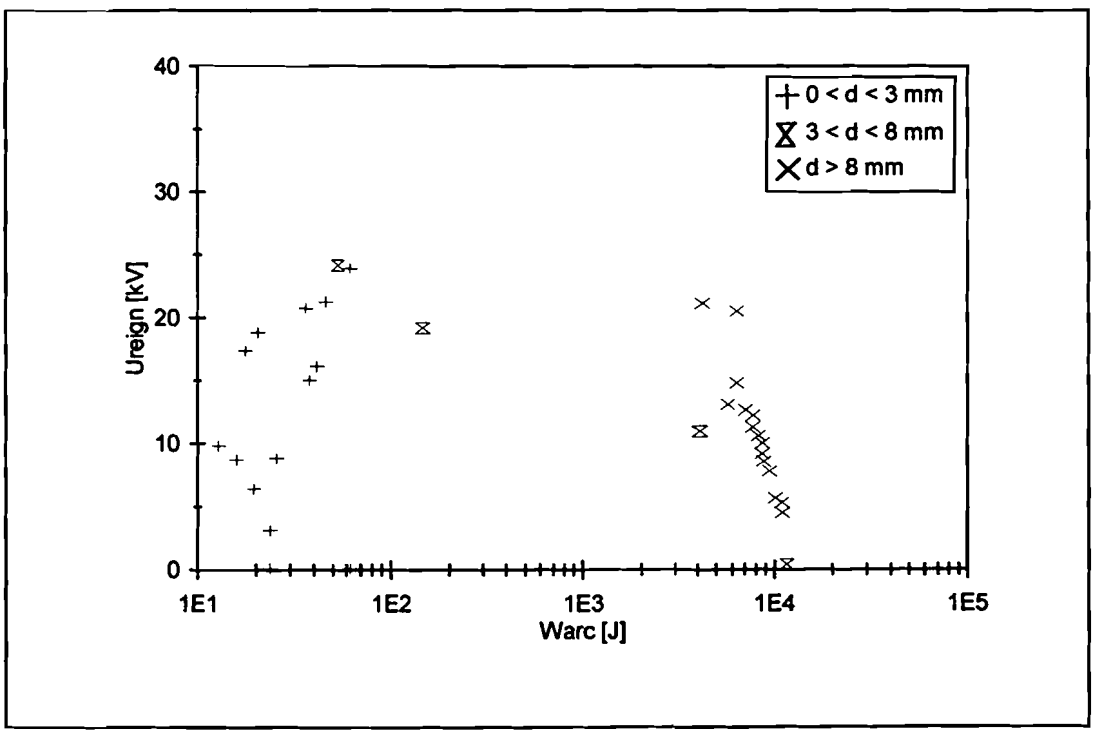

Figure C-13: Correlation between reignition voltage and arc energy for the CuCr coil-type contacts.

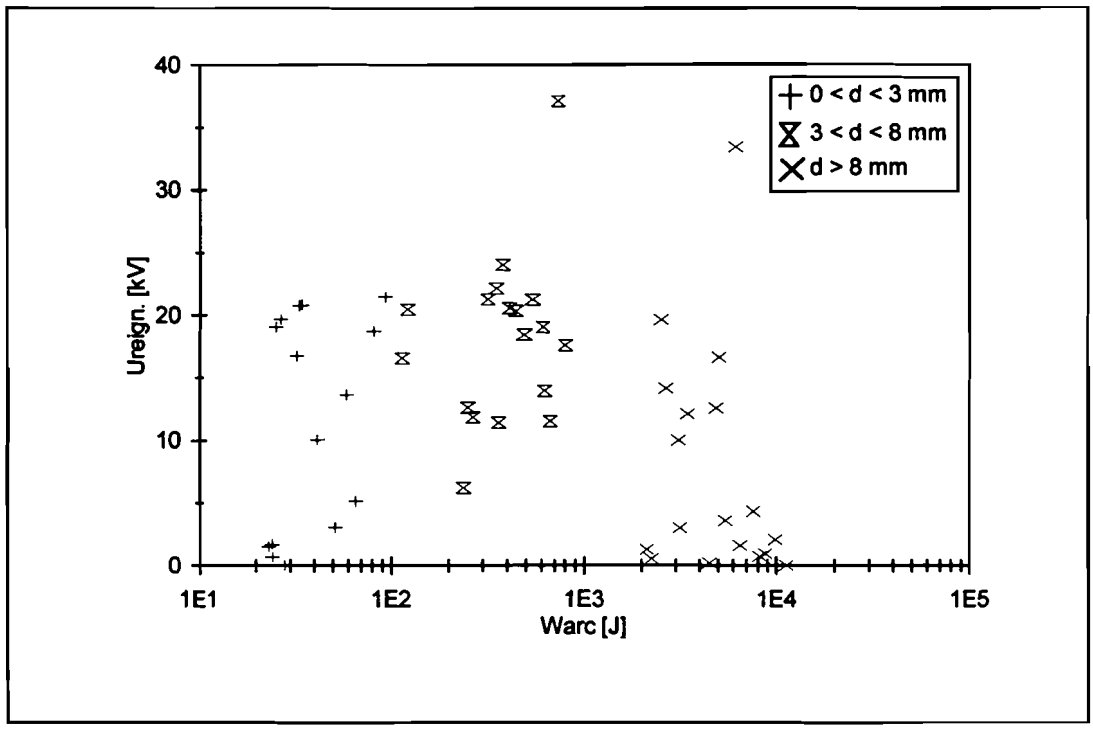

Figure C-14: Correlation between reignition voltage and arc energy for the CuW coil-type contacts.

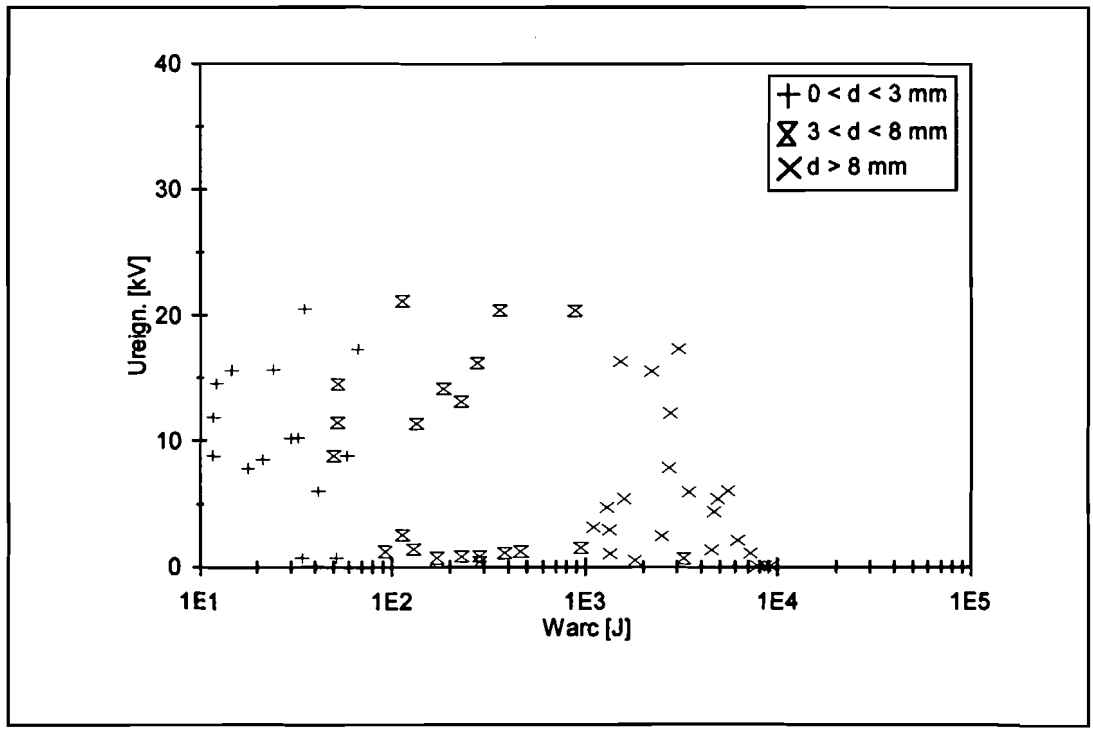

Figure C-15: Correlation between reignition voltage and arc energy for the AgWC coil-type contacts.

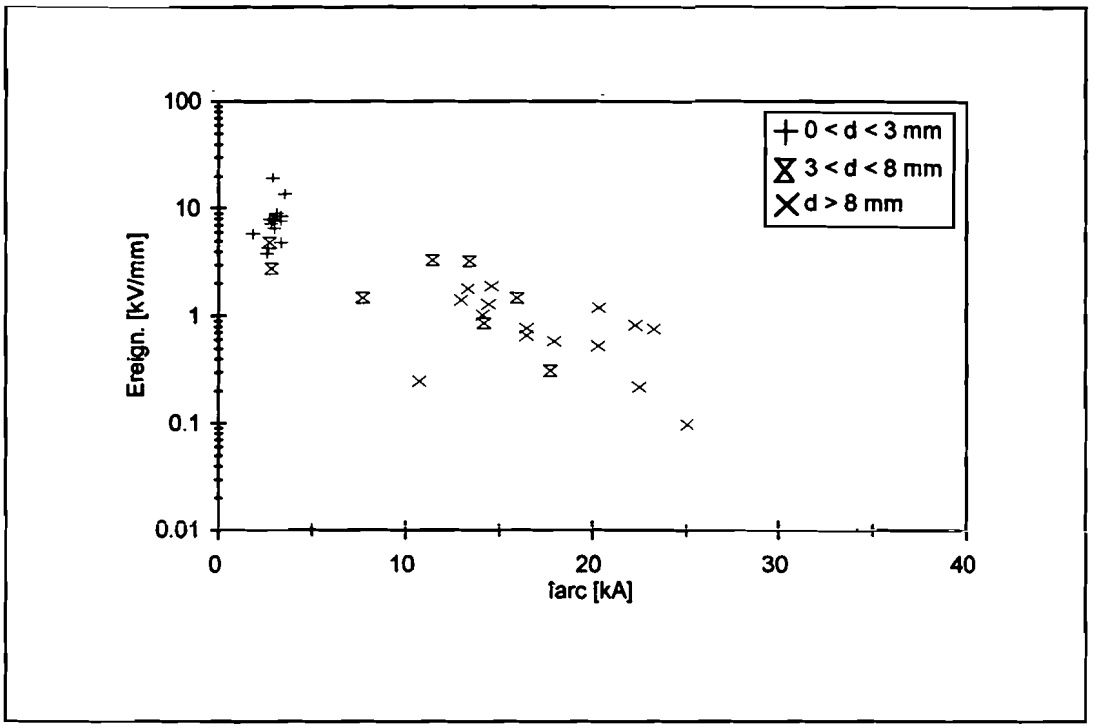

Figure C-16: Correlation between electric reignition field strength and maximum arc current for the Cu coil-type contacts.

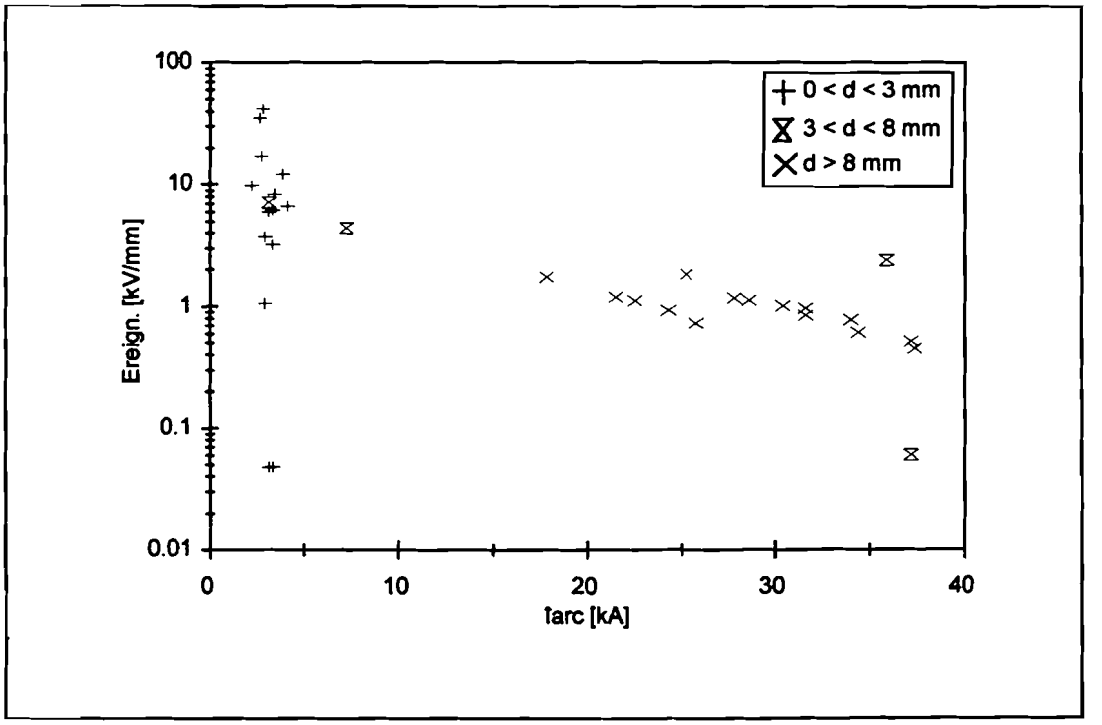

Figure C-17: Correlation between electric reignition field strength and maximum arc current for the CuCr coil-type contacts.

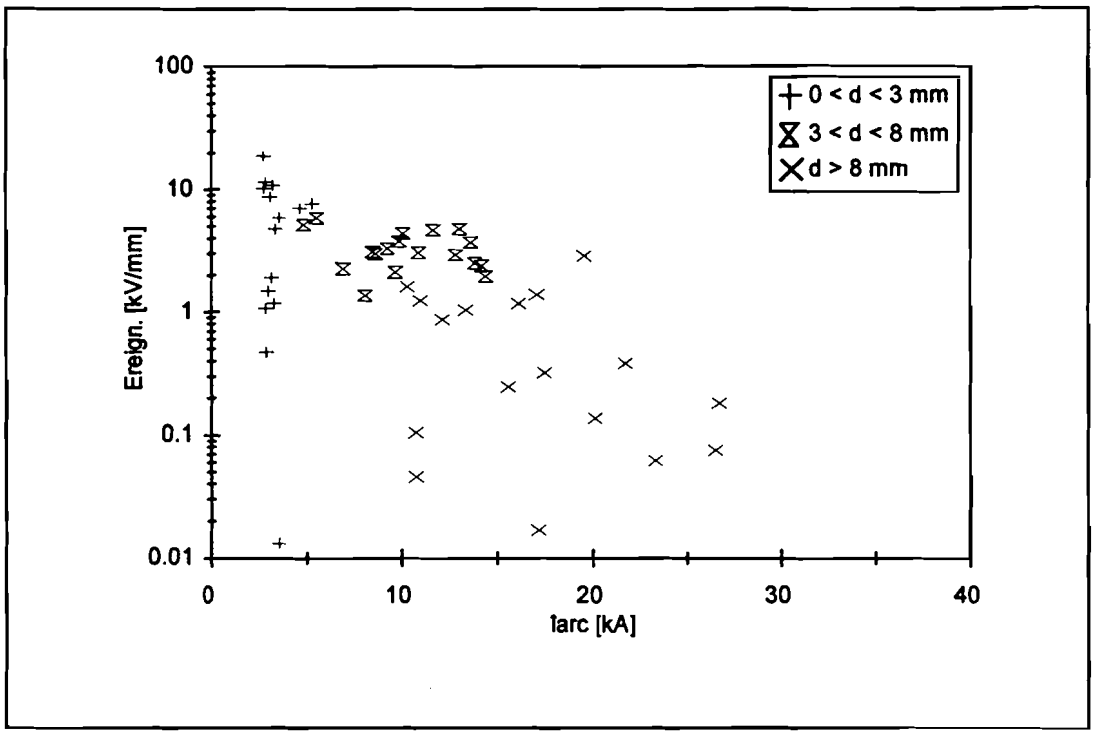

Figure C-18: Correlation between electric reignition field strength and maximum arc current for the CuW coil-type contacts.

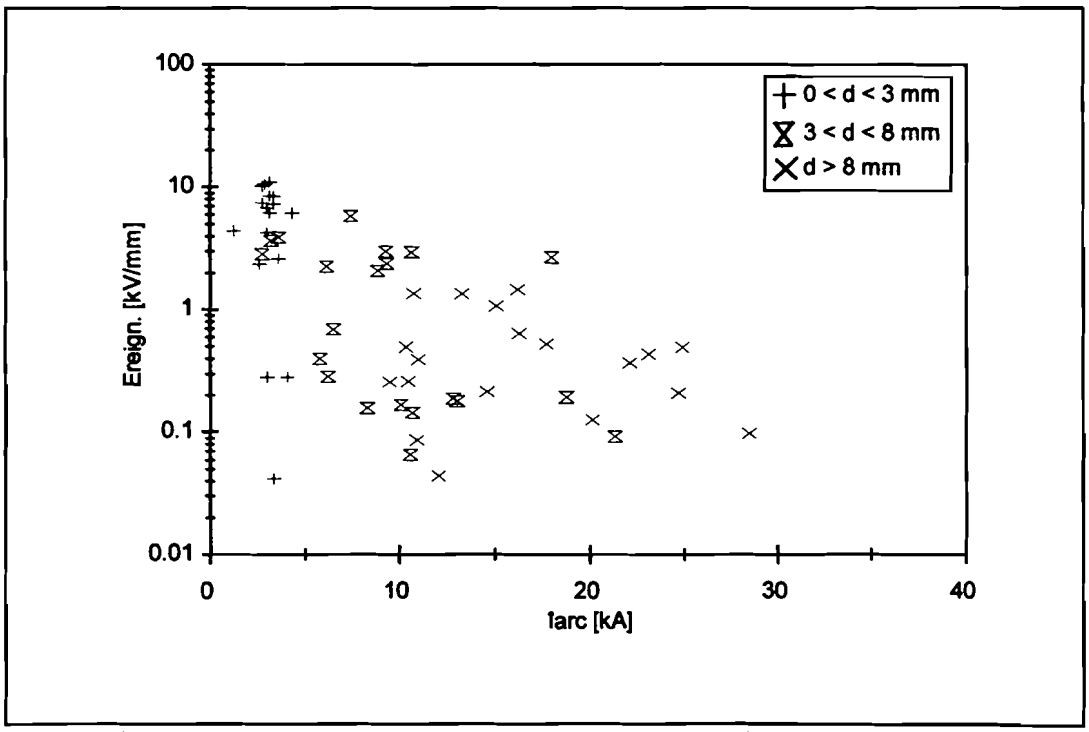

Figure C-19: Correlation between electric reignition field strength and maximum arc current for the AgWC coil-type contacts.

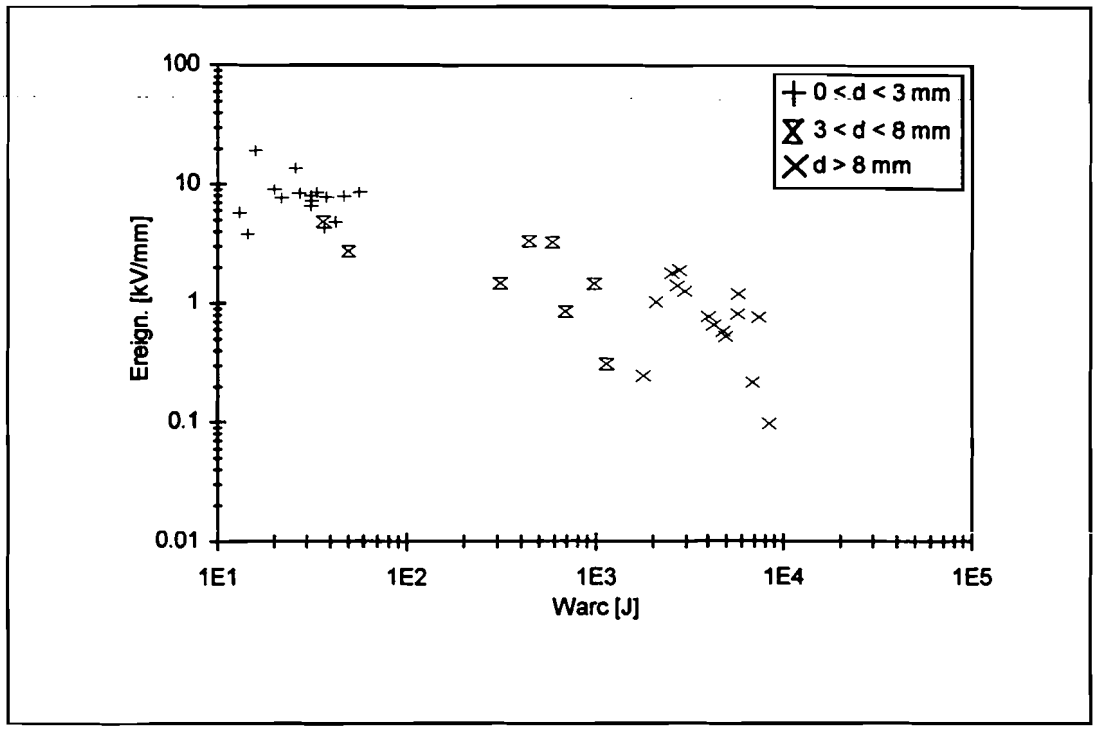

Figure C-20: Correlation between electric reignition field strength and arc energy for the Cu coil-type contacts.

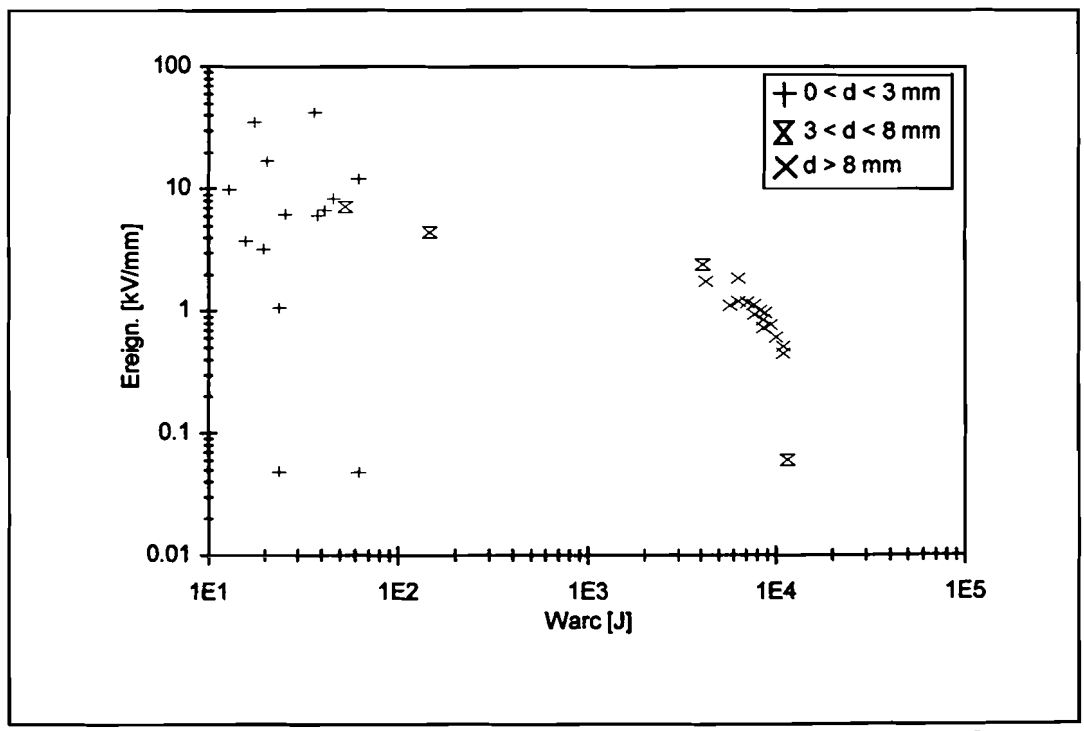

Figure C-21: Correlation between electric reignition field strength and arc energy for the CuCr coil-type contacts.

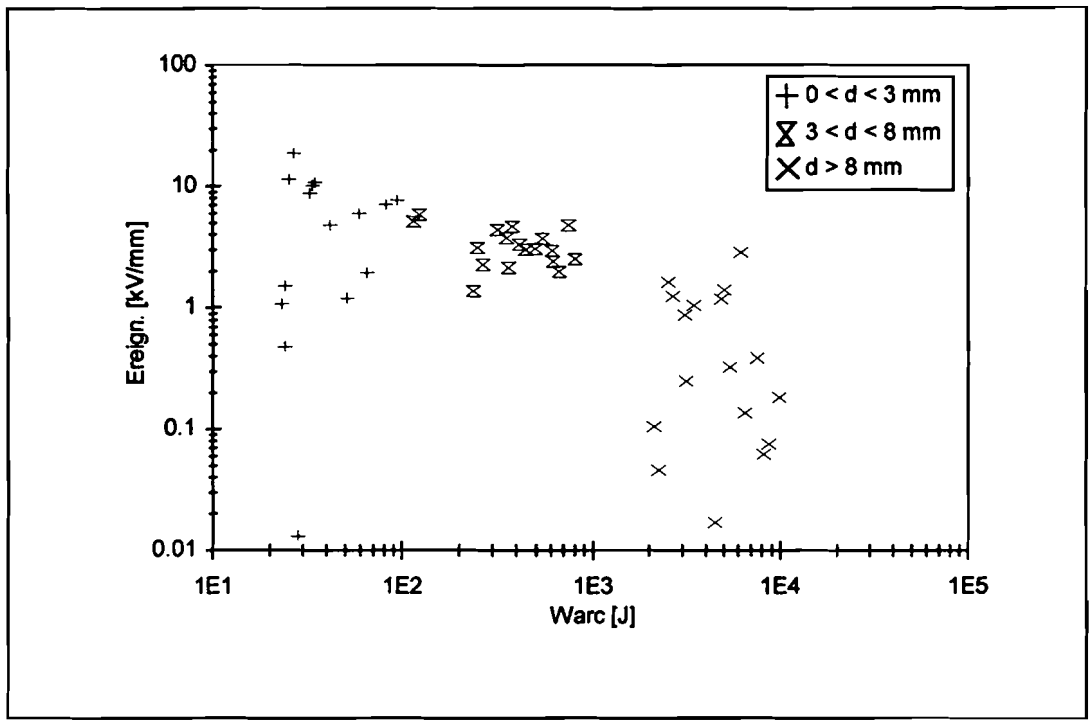

Figure C-22: Correlation between electric reignition field strength and arc energy for the CuW coil-type contacts.

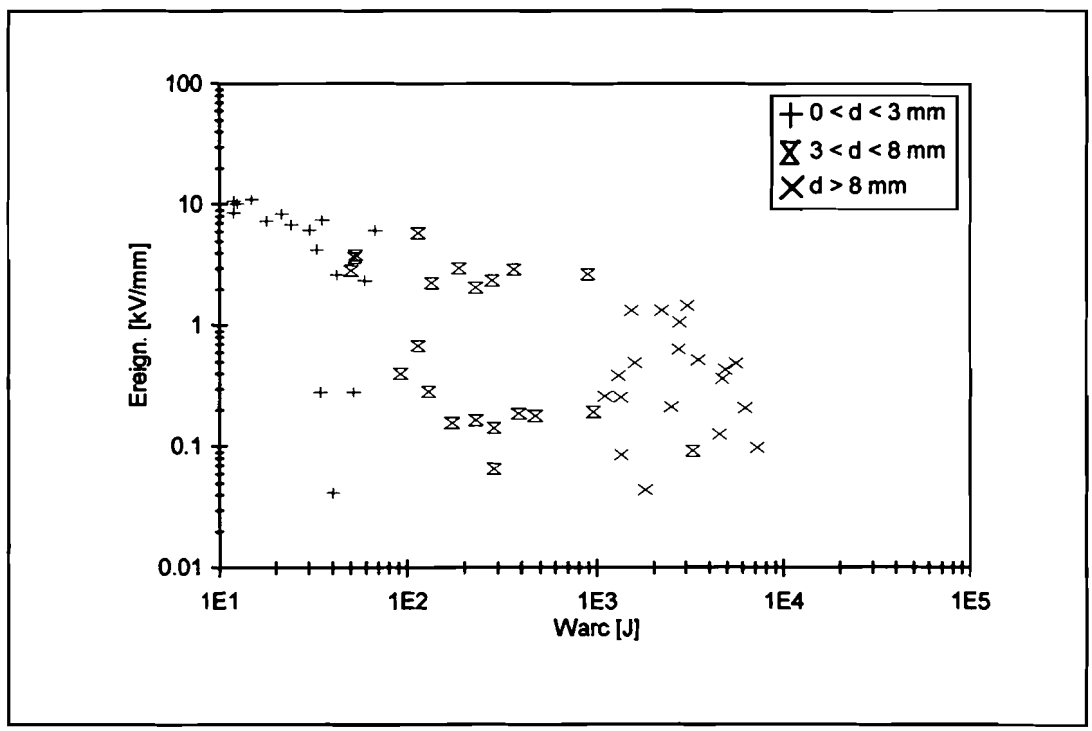

Figure C-23: Correlation between electric reignition field strength and arc energy for the AgWC coil-type contacts.

Appendix D: PDEase2 problem description file

```
title "CURRENT CONTRACTION"

     {Calculation of the azimuthal field in a vacuum arc.
      The axial current density is calculated from the
      azimuthal magnetic field.
      The used formula's are given in cylinder coordinates.
      Steady state of the plasma is asumed.
      Quasi neutral plasma is asumed.
      The radial and axial magnetic field components are not
      calculated.}

Select

     errlim = 0.00013
     gridlimit = 20


coordinates

     ycylinder("r","z")


Variables

     Ba, Ua                    {The azimuthal magnetic field
                                component, the sheath
                                potential drop Φ_A}


Definitions

     I = 9000                  {A}       {circuit current}
     D = 0.0069                {m}       {contact gap}
     rho = 0.015               {m}       {contact radius}
     mu = 1.25664e-6           {H/m}     {magnetic
                                           permeability of
                                           vacuum}
     me = 9.10939e-31          {kg}      {electron mass}
     eps = 8.85419e-12         {F}       {electric permitivity
                                           of vacuum}
     e = 1.6022e-19            {C}       {electron charge}
     k = 1.38066e-23           {J/K}     {Boltzman's constant}
     Tarc = staged (3.1e4)     {K}       {arc temperature}
     vp = -500                 {m/s}     {mean plasma
                                           velocity}
     kTe = (4.32e-19)          {J}       {mean thermal energy
                                           of the electrons}
```

```
     vTe = sqrt(kTe/(2*pi*me))
                                {m/s}      {mean thermal speed
                                            of electrons in
                                            axial direction}

     f = 0.10                              {ion fraction of
                                            total current}

     Ne = if I < 4000 then 5.6e17*I-4.5e20 else 3.3e17*I+7e20
                                {m-3}      {electron density}

     lambda = 12*pi*Ne*((eps*k*Tarc)/(Ne*e^2))^1.5
                                           {help variable}

     sigma = (24*pi*(eps^2)*(k*Tarc)^1.5)/((e^2) *
                                ((3*me)^0.5) * LN(lambda))
                                {1/Ω}      {plasma conductivity}

Initial values

     Ba = (mu*I*r)/(2*pi*rho^2)            {Jz homogenius}


Equations

     del2(Ba) + dr((dr(r*Ba))/r) = -dzz(Ba)

     (2*vTe*f*I*exp((-Ua*e)/kTe))/(pi*rho^2*(-
          vp)*(1+erf(sign(Ua)*sqrt((e*abs(Ua))/kTe)))) -
               (f*I)/(pi*rho^2) = (dr(r*Ba))/(r*mu)


Boundaries                                {Boundary conditions}


     Region "plasma"

          value(Ba)=0
          start (0,0) line to (0,D)

          value(Ba) = (mu*I*r)/(2*pi*rho^2)
          line to (rho,D)

          value(Ba) = (mu*I)/(2*pi*rho)
          line to (rho,0)

          natural(Ba) =sigma*((dr((Ba)^2))/(e*Ne)
                         - mu*vp*Ba - mu*dr(Ua))
          line to finish
```

```
Monitors              {Graphical output on computer screen}

     contour(Ba)
     contour((dr(r*Ba))/(r*mu))


plots                 {Graphical output on disk}

     surface((dr(r*Ba))/(r*mu)) as "Jz in plasma"

     elevation((dr(r*Ba))/(r*mu)) from (0,0) to (rho,0) as
     "Jz on anode surface"

     elevation(Ua) from (0,0) to (rho,0) as "Ua on plasma-
     sheath border"

     surface(Ba) as "Azimuthal magnetic field"


End
```

Appendix E: Results of the current contraction model

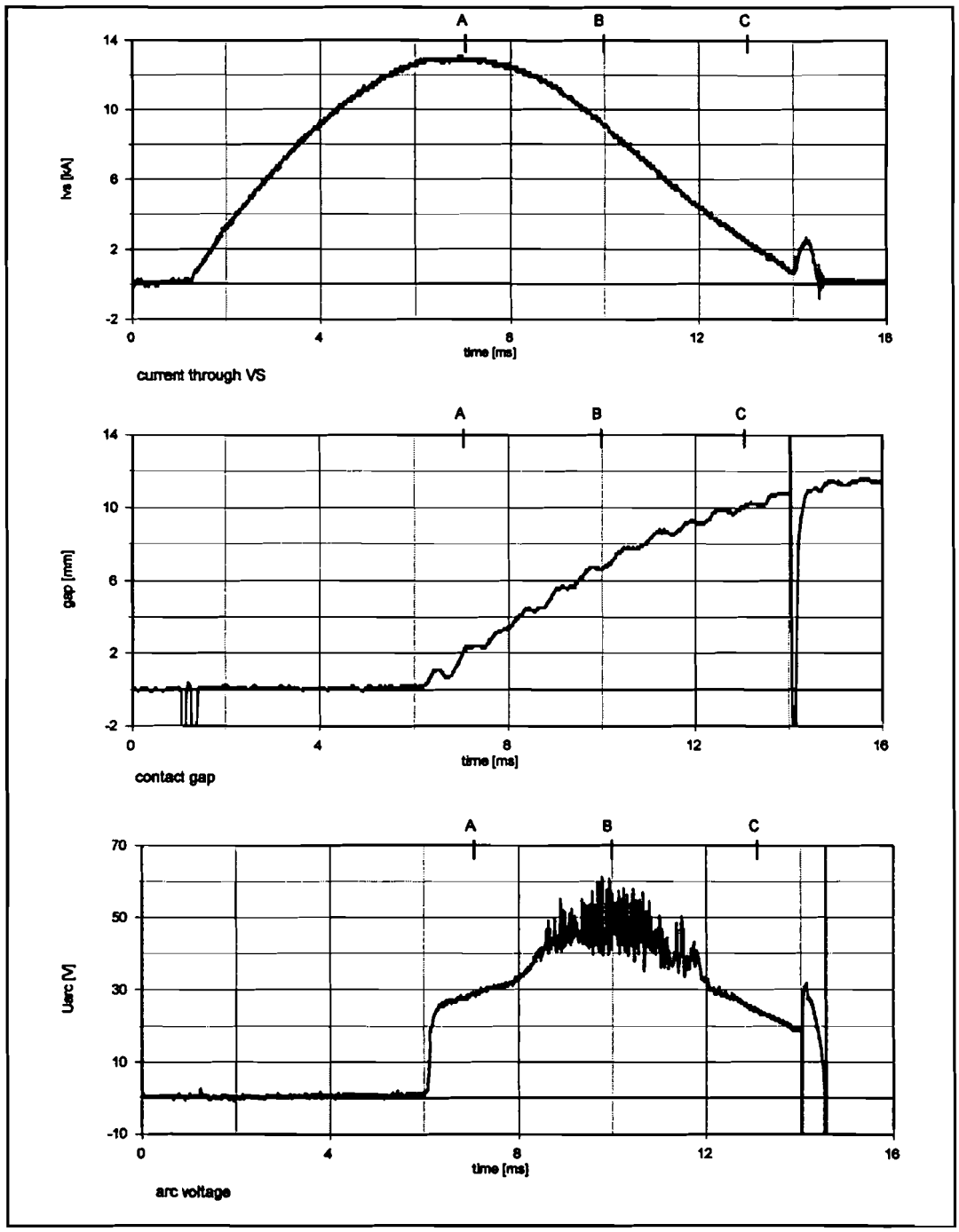

Figure E-1: Measurement I13_53 used as configuration for the current contraction model.

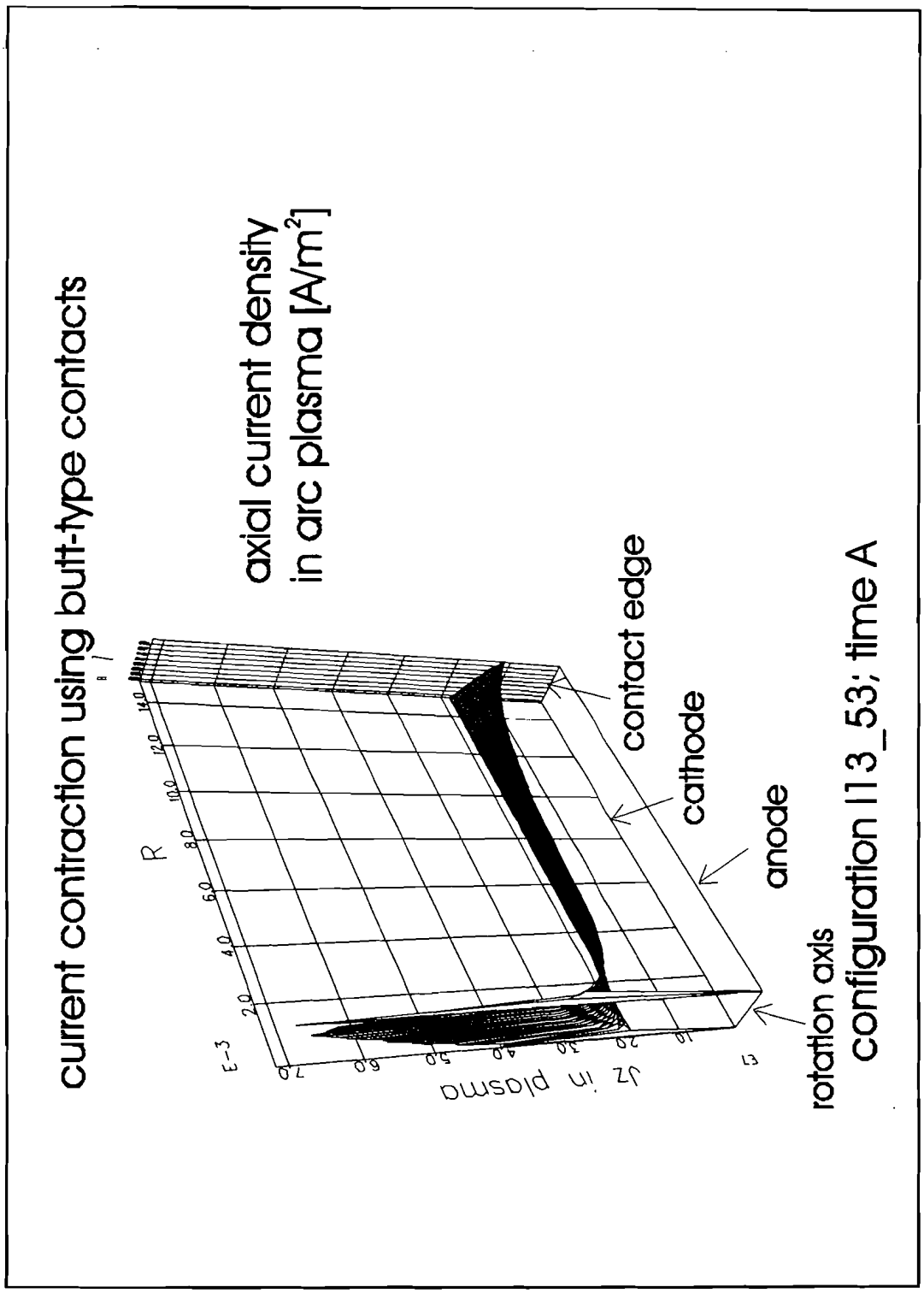

Figure E-2: Axial current density in the arc plasma at time A.

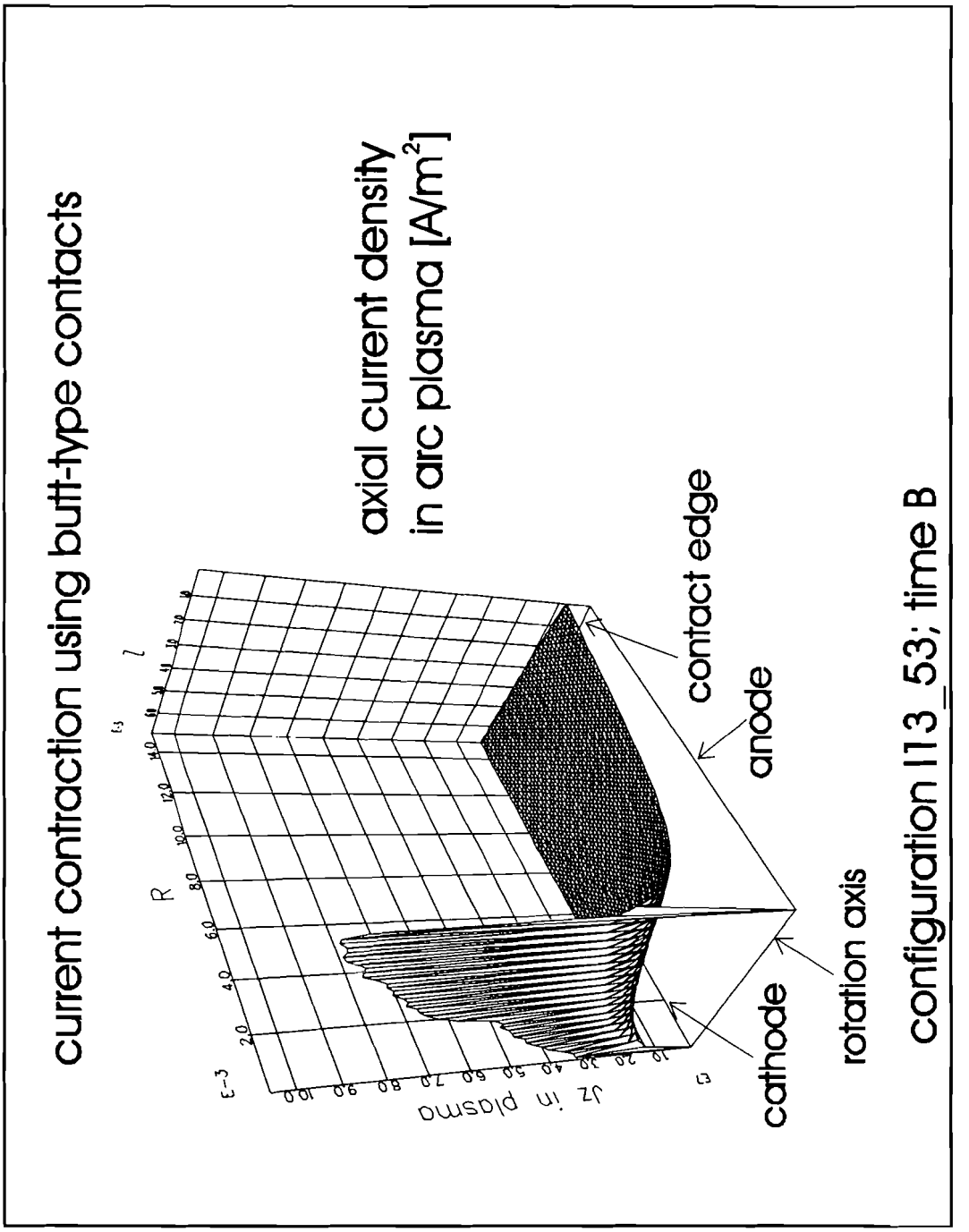

Figure E-3: Axial current density in the arc plasma at time B.

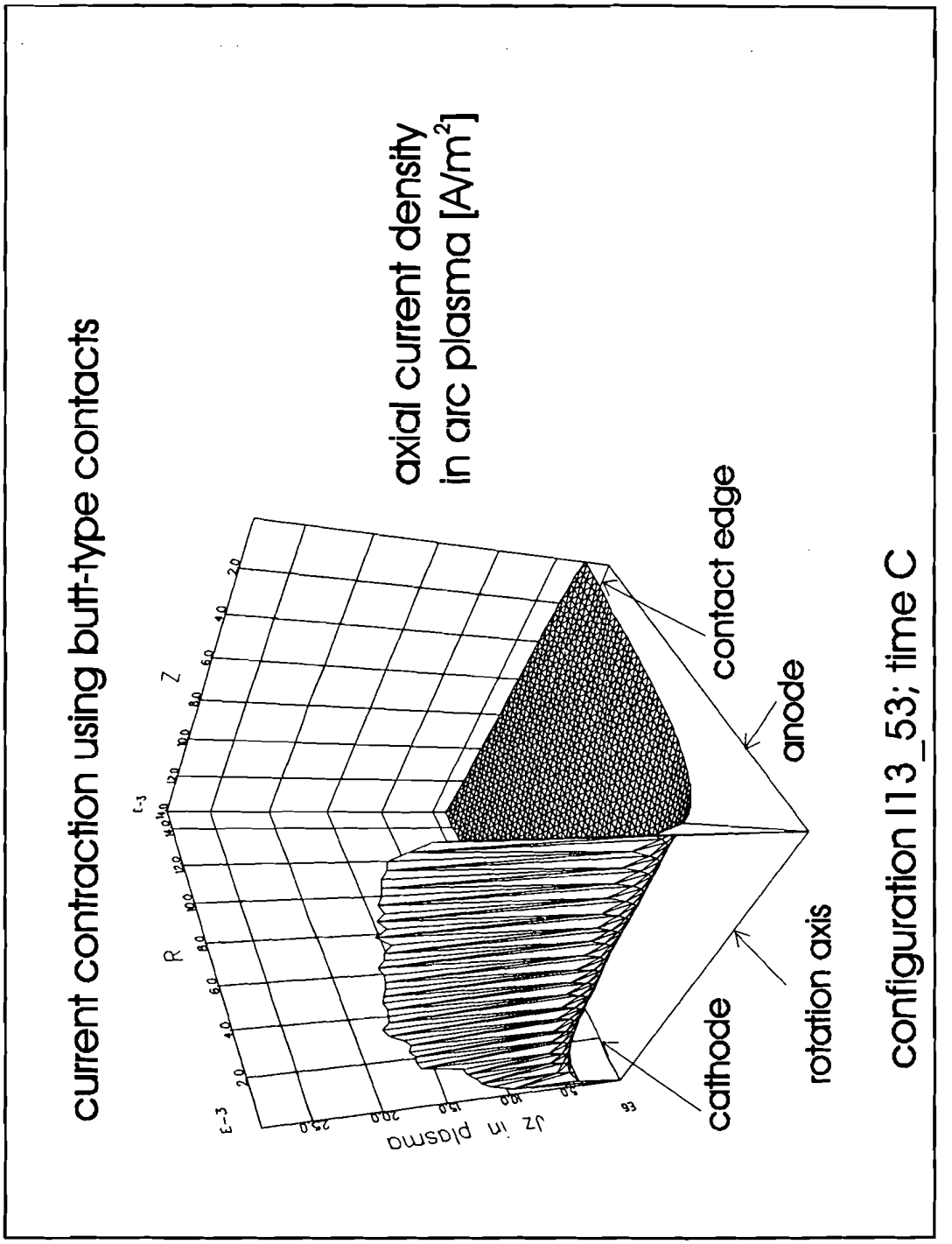

Figure E-4: Axial current density in the arc plasma at time C.

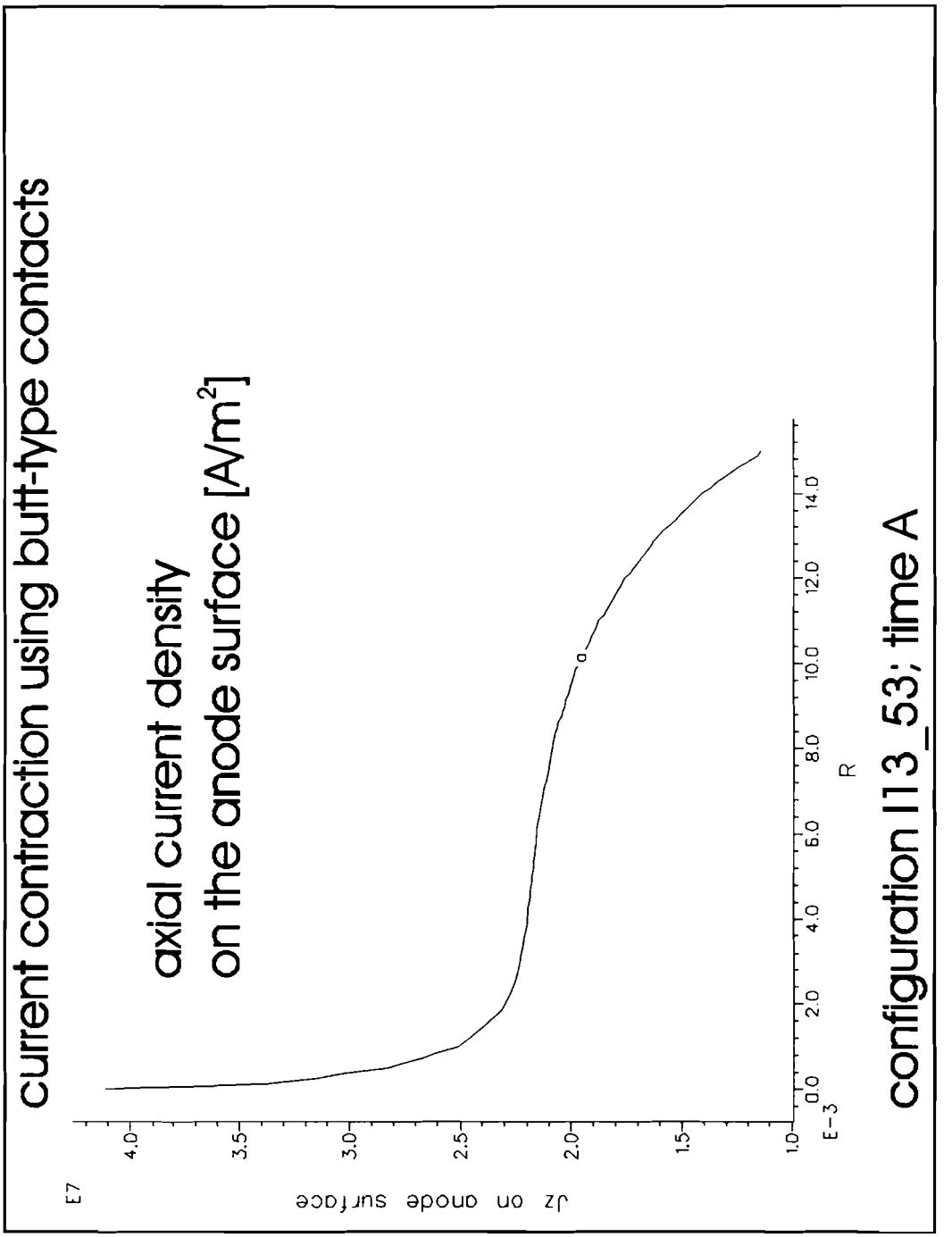

Figure E-5: Axial current density on the anode surface at time A.

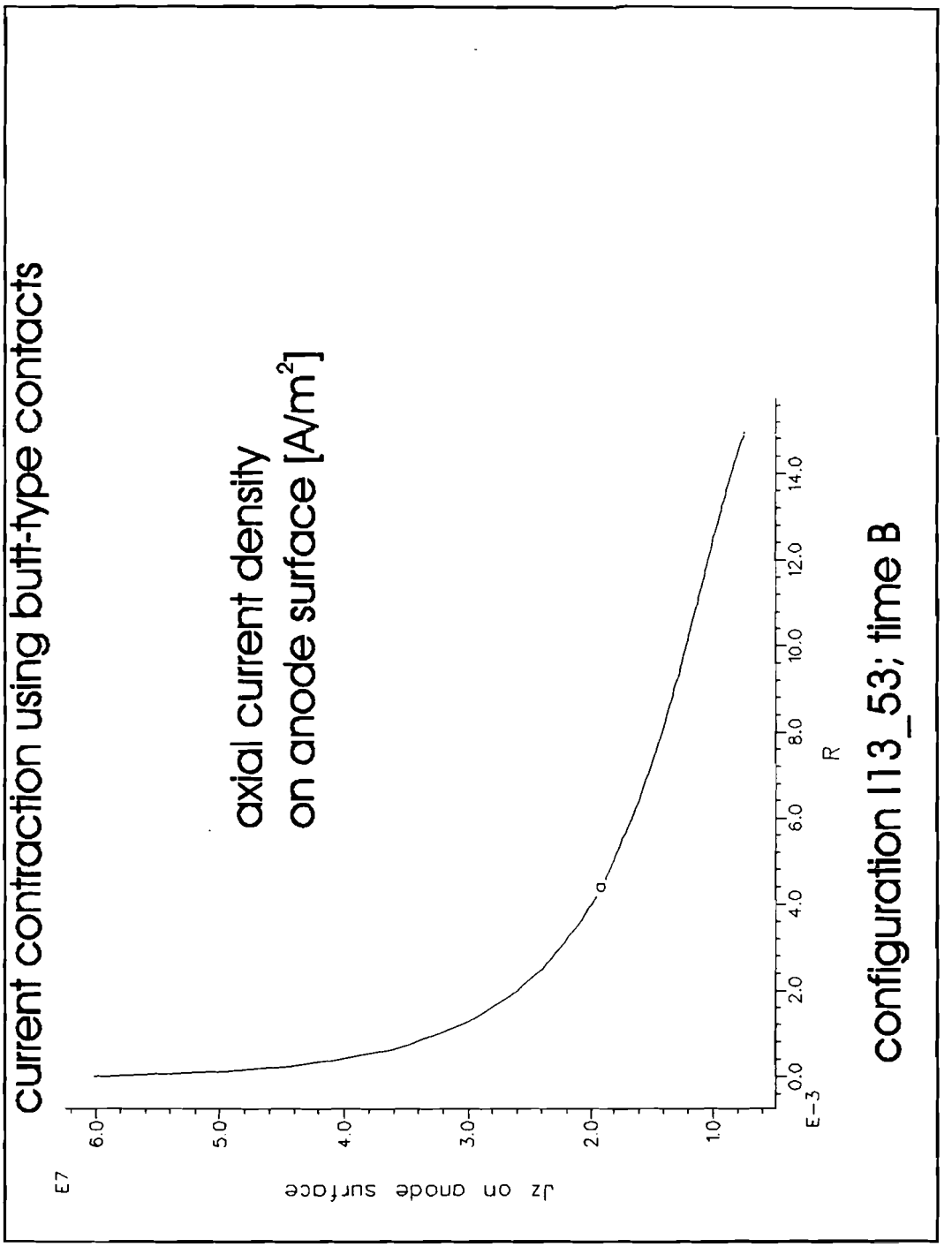

Figure E-6: Axial current density on the anode surface at time B.

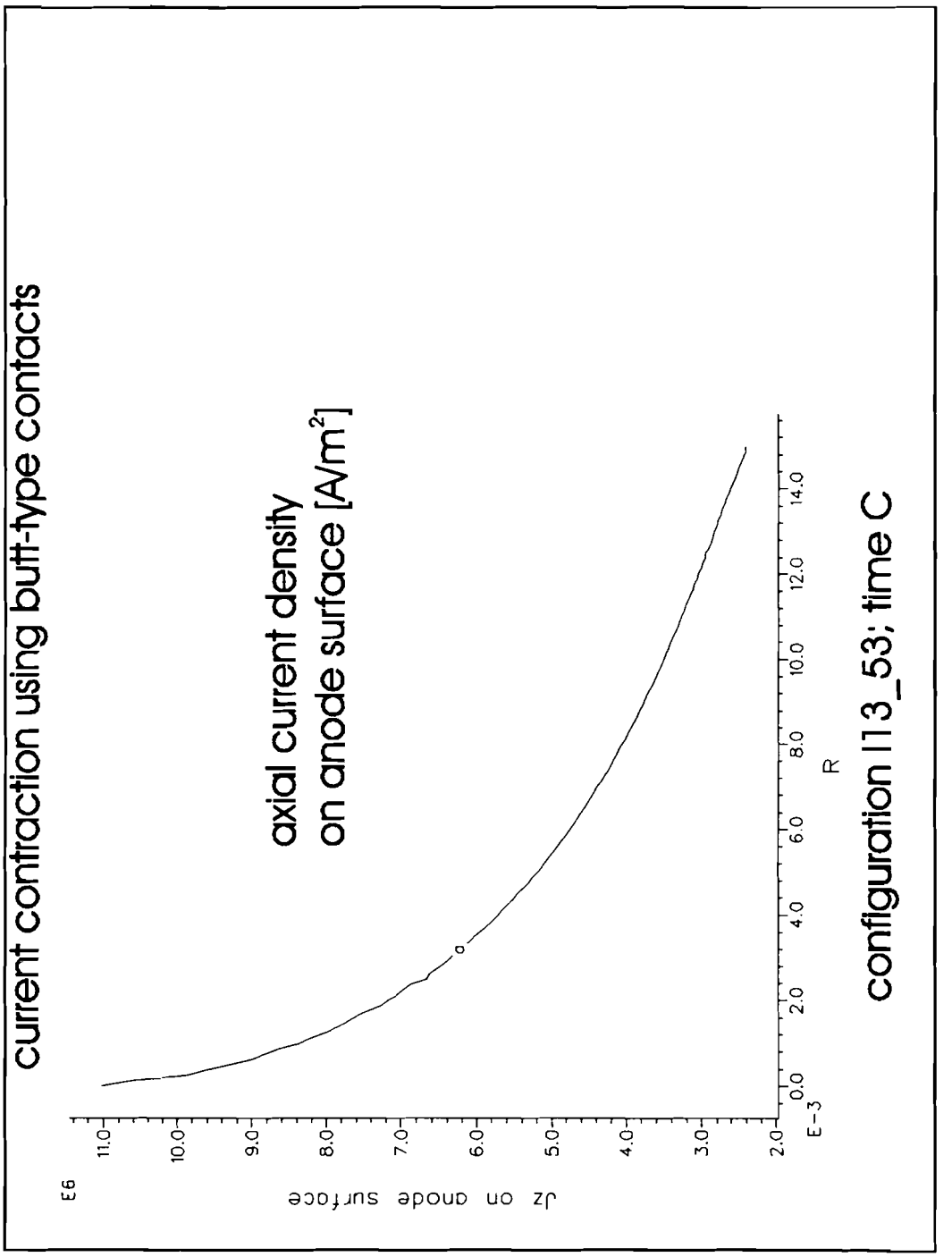

Figure E-7: Axial current density on the anode surface at time C.

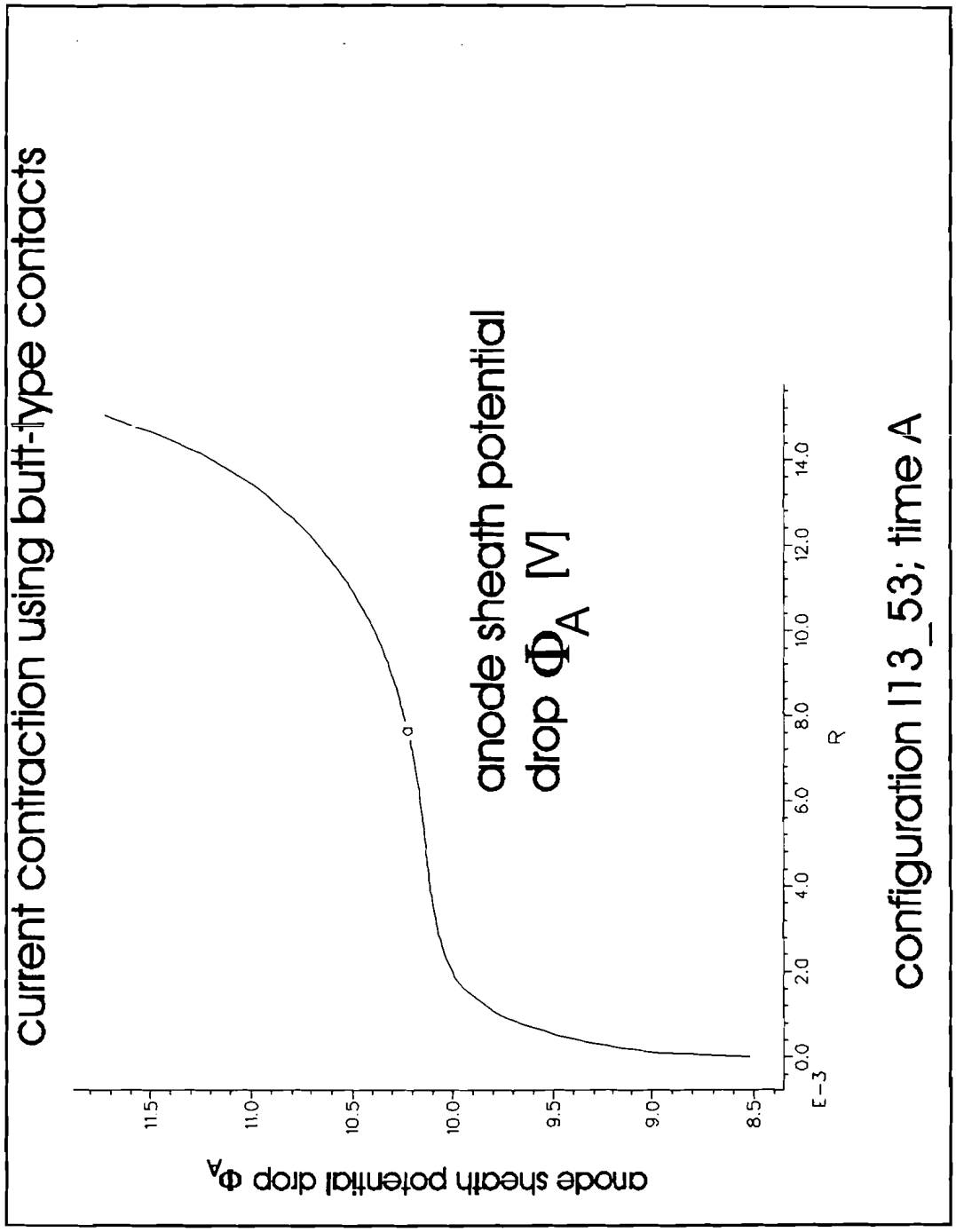

Figure E-8: Anode sheath potential drop Φ_A at time A.

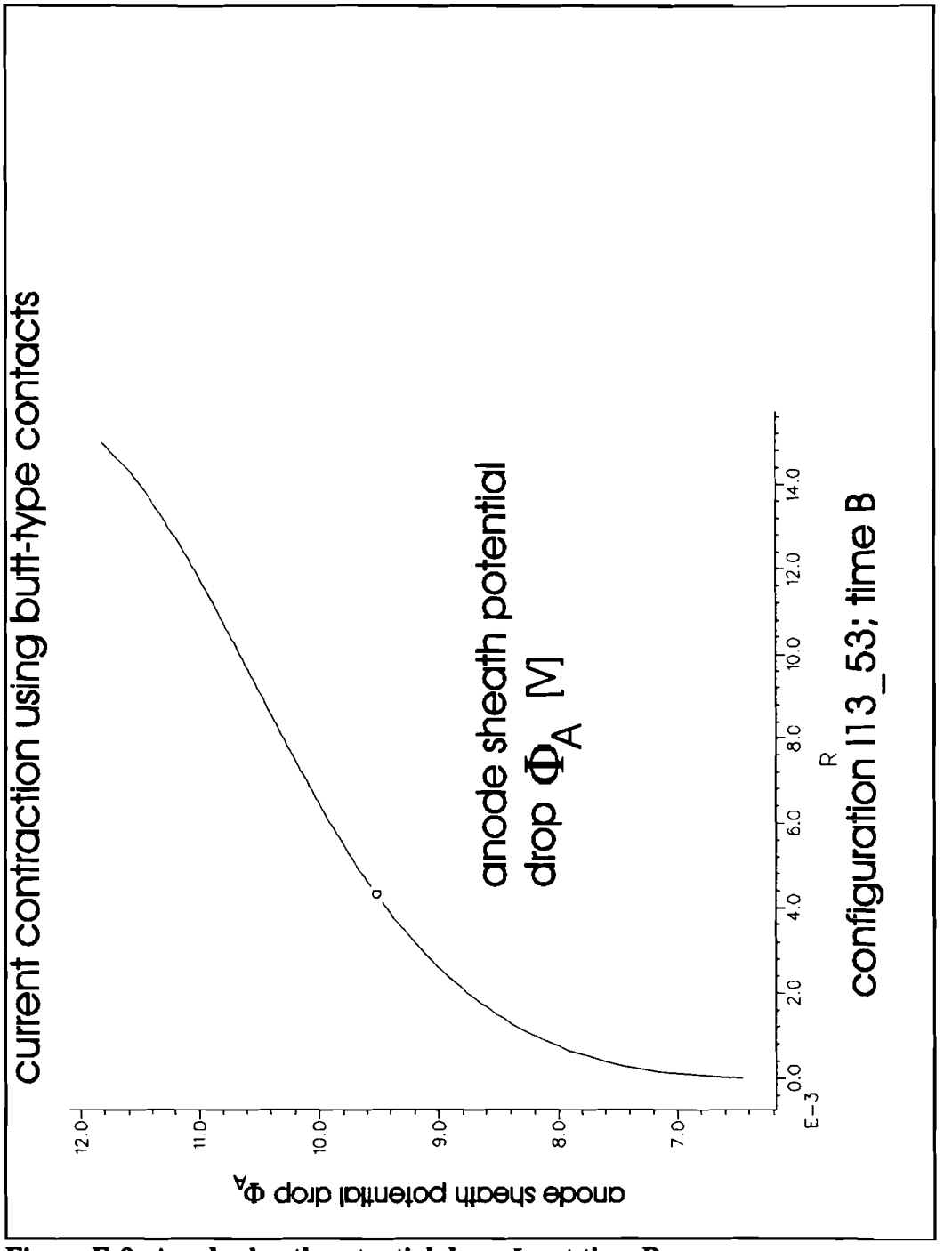

Figure E-9: Anode sheath potential drop Φ_A at time B.

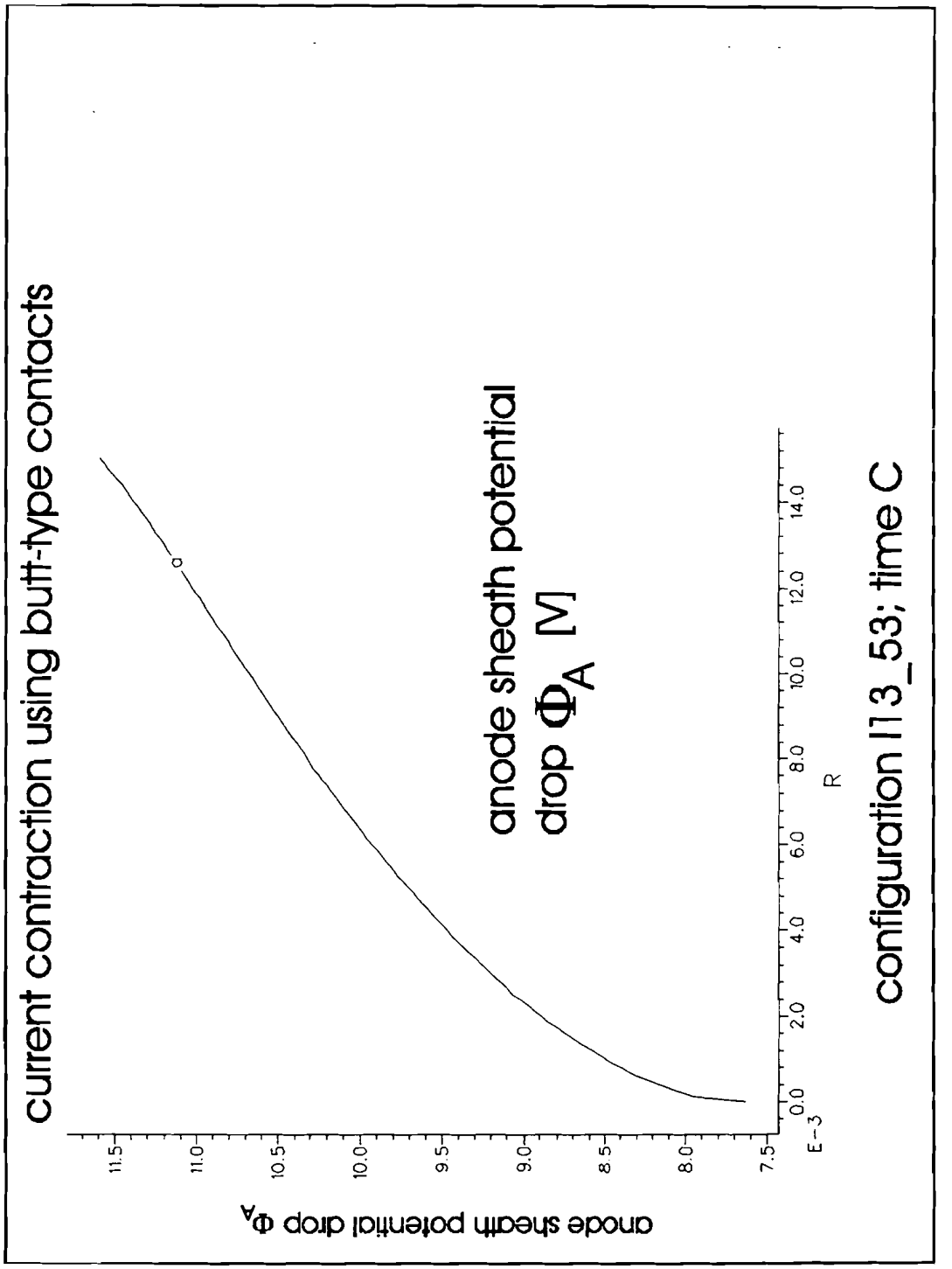

Figure E-10: Anode sheath potential drop Φ_A at time C.

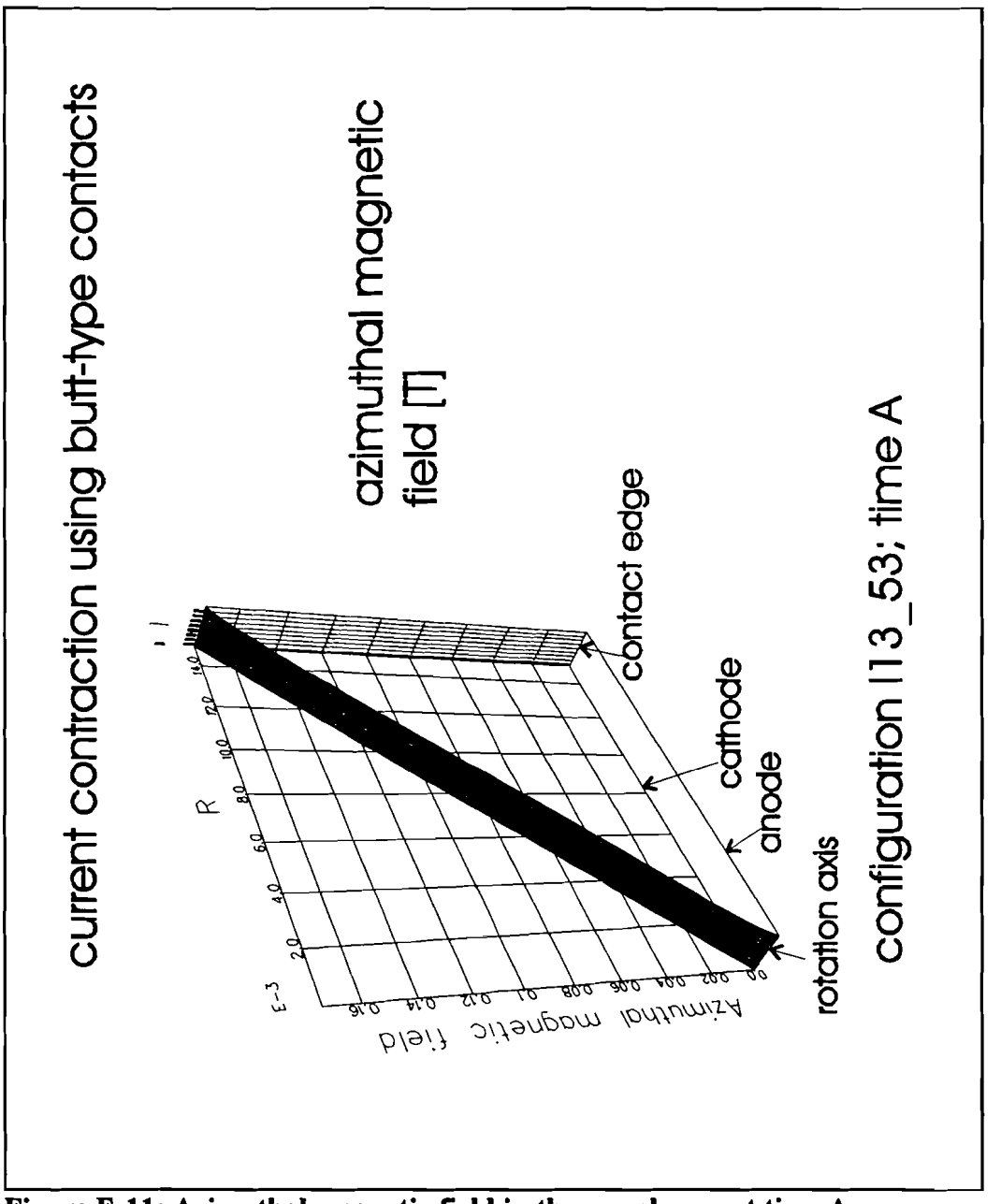

Figure E-11: Azimuthal magnetic field in the arc plasma at time A.

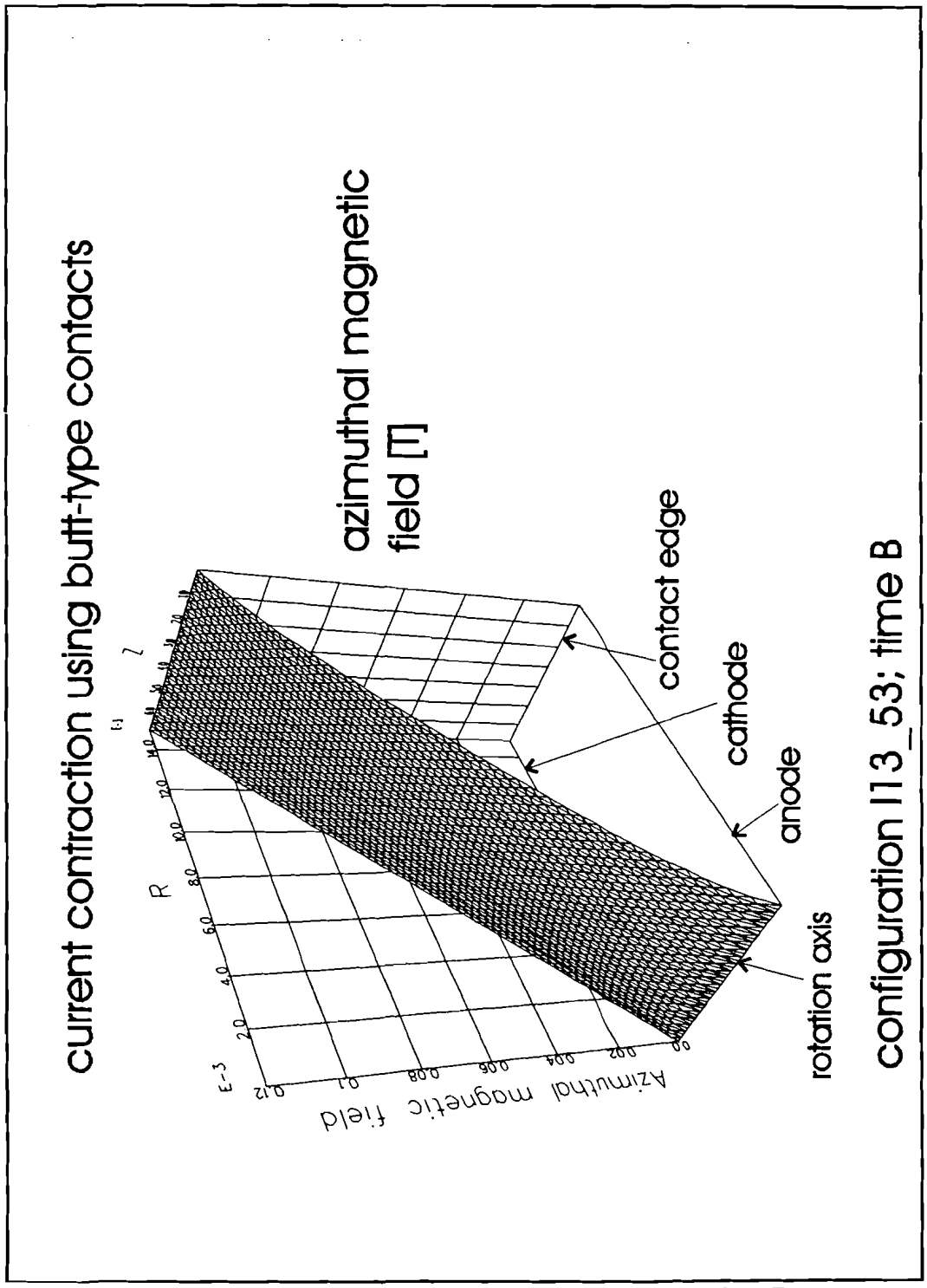

Figure E-12: Azimuthal magnetic field in the arc plasma at time B.

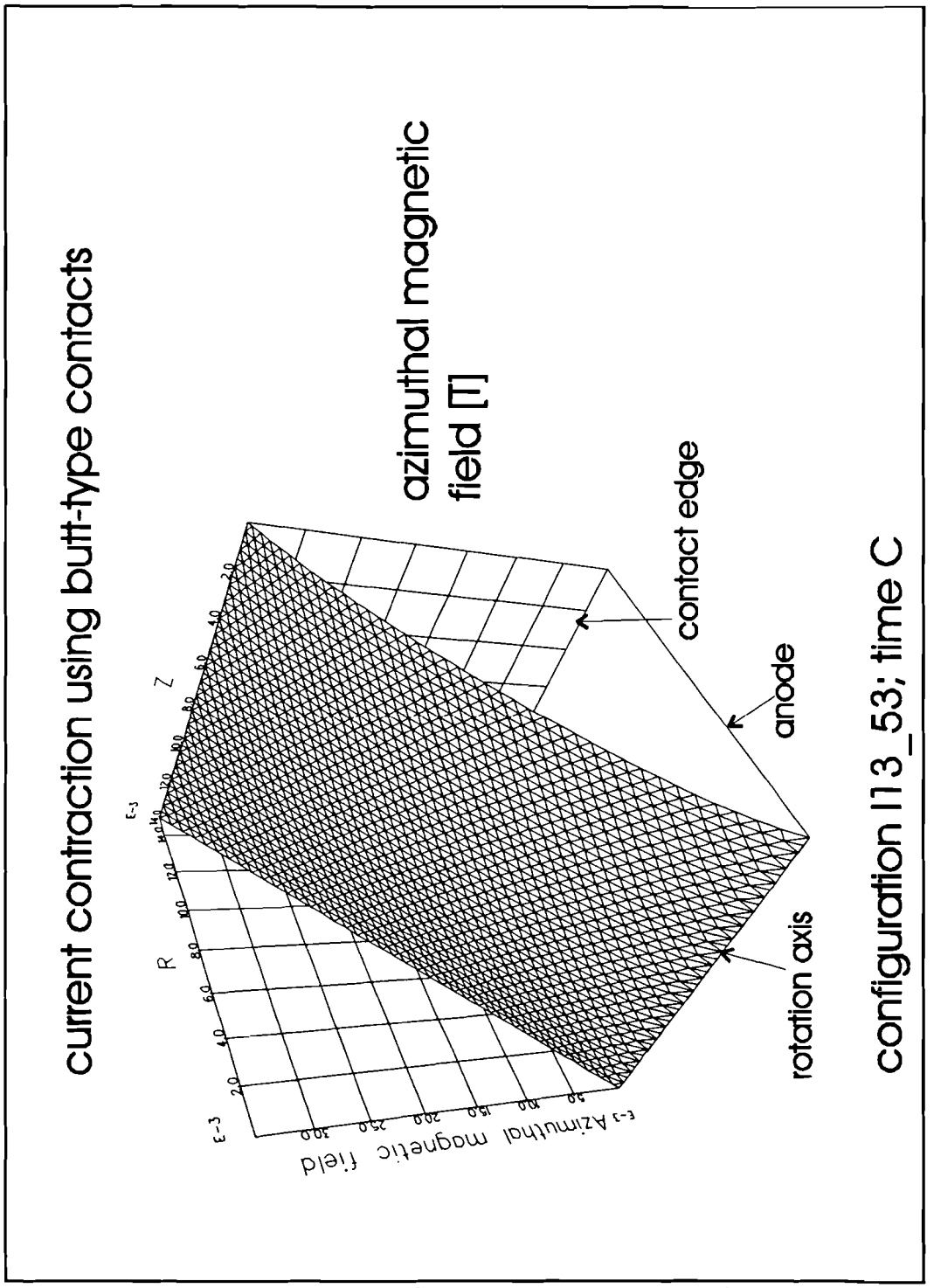

Figure E-13: Azimuthal magnetic field in the arc plasma at time C.

List of symbols

∇	= gradient operator	
Δ	= Laplace operator	
ε_0	= electric permitivity of vacuum	[F/m]
κ	= mass density	[kgm^{-3}]
λ	= heat conduction coefficient	[$Wm^{-1}K^{-1}$]
μ_0	= magnetic permeability of vacuum	[H/m]
ξ	= help variable	
ρ_p	= plasma resistance per meter gap length	[Ω/m]
σ	= plasma conductivity	[$\Omega^{-1}m^{-1}$]
Φ_A	= anode sheath potential drop	[V]
ω_{inj}	= $2\pi f_{inj}$	[rad/s]
ω_{main}	= $2\pi f_{main}$	[rad/s]
A	= arc cross section	[m^2]
B	= magnetic field vector	[T]
c_s	= specific heat	[$Jkg^{-1}K^{-1}$]
E	= electric field vector	[V/m]
e	= elementary charge	[C]
F	= ratio of ion current and circuit current	
f	= frequency of the sinusoidal current	[Hz]
f_{inj}	= frequency of injection current	[Hz]
f_{main}	= frequency of main current	[Hz]
I	= maximum amplitude of the current	[A]
I_{inj}	= maximum amplitude injection current	[A]
I_{main}	= maximum amplitude of main current	[A]
i	= current	[A]
J	= current density vector	[Am^{-2}]
J_{ac}	= average anode spot threshold current density	[Am^{-2}]
J_z	= current density in axial direction	[Am^{-2}]
J_{sat}	= saturation current density	[Am^{-2}]
K_{Bz}	= amplitude of axial magnetic field component deep inside the contacts	[T]
k	= Boltzman's constant	[J/K]
L_{mod}	= model reactance	[H]
m_e	= electron mass	[kg]
n_e	= electron density	[m^{-3}]
n_{es}	= electron density in the sheath region	[m^{-3}]
n_i	= ion density	[m^{-3}]
Q_{el}	= electron-ion momentum transfer collision cross section	[m^2]
R	= radius of contact	[m]
R_{mod}	= model resistance	[Ω]
T_{arc}	= arc temperature	[K]
T_e	= thermal electron energy	[J]
T_m	= melting temperature	[K]
T_v	= boiling temperature	[K]
t	= time	[s]
t_{arc}	= arcing time	[s]
t_{cz}	= time of first current zero	[s]
$t_{cz\ main}$	= time of current zero of main current	[s]
t_{inj}	= 1/frequency of injection current	[s]
U_0	= constant ionization voltage	[V]
U_{arc}	= arc voltage	[V]
Uvs	= measured arc voltage	[V]

v	= plasma velocity vector	[m/s]
v_c	= constant contact opening velocity	[m/s]
v_e	= electron velocity in axial direction	[m/s]
v_{et}	= thermal electron velocity in all directions	[m/s]
v_i	= ion velocity in axial direction	[m/s]
$v_{Te,z}$	= thermal electron velocity in axial direction	[m/s]
W_{arc}	= maximum cumulative arc energy	[J]
z	= average ion charge number	